Erzeugung dichter Elektronenpulse mit Laser-Plasma-Beschleunigern für QED Experimente in hohen Feldern

Stephan Kuschel

Generation of dense electron bunches by laser plasma accelerators for QED experiments in high fields

Stephan Kuschel

DISSERTATION

zur Erlangung des akademischen Grades

DOKTOR RERUM NATURALIUM (DR. RER. NAT.)

Vorgelegt dem Rat der

Physikalisch-Astronomischen Fakultät
Friedrich-Schiller-Universität Jena

1. Gutachter
   Prof. Dr. Matt Zepf
   Institut für Optik und Quantenelektronik
   Friedrich-Schiller-Universität Jena
   Max-Wien-Platz 1
   07743 Jena

2. Gutachter
   Prof. Dr. Jörg Schreiber
   Fakultät für Physik der Ludwig-Maximilians-Universität München
   Lehrstuhl für Experimentalphysik - Medizinische Physik
   Am Coulombwall 1
   85748 Garching b. München

3. Gutachter
   Prof. Dr. Dino Jaroszynski
   John Anderson Building
   107 Rottenrow East
   Glasgow
   G4 0NG
   UNITED KINGDOM

Tag der Disputation: 23.02.2018

vorgelegt von Stephan Kuschel,

geboren am 14.03.1986 in Celle.

Synopsis

Die Quantenelektodynamik (QED) gehört zu den am besten überprüften Theorien unserer Zeit. Dennoch konnten fundamentale Prozesse der Theorie, wie z. B. Paarproduktion aus dem Vakuum oder die Bewegung eines Elektrons in extremen Feldern, bisher nicht im Labor gemessen werden. Solche Prozesse der Starkfeld-QED können mit Experimenten untersucht werden, bei denen ein hochintensiver Laserpuls mit einem ultrarelativistischen Elektronen oder γ-Strahl wechselwirken. Besonders realistisch ist die Durchführung solcher Experimente unter Verwendung von hochintensiven Laserpulsen sowohl für die Beschleunigung von Elektronen als auch für die Bereitstellung hoher Felder.

Die Entwicklung von Laser-Plasma getriebenen Beschleunigern ist eine vergleichsweise neue Entwicklung auf diesem Gebiet. Durch die enormen Felder, die das Plasma zur Verfügung stellen kann, ist es möglich, ultrakurze und dichte Elektronenpulse über sehr kurze Strecken zu beschleunigen. Der beschleunigte Elektronenpuls ist prinzipbedingt mit einem Hochintensitätslaser gekoppelt, weswegen diese Beschleuniger ideale Vorraussetzungen für die Umsetzung von QED Experimenten bei hohen Feldstärken bieten. Mithilfe der Elektronenpulse können außerdem γ-Strahlen hoher Intensität erzeugt werden, wodurch auch QED-Experimente in greifbare Nähe rücken, die einen intensiven γ-Strahl benötigen. Allerdings muss die Qualität und Stabilität der Laser-Plasma beschleunigten Elektronenpulse noch weiter verbessert werden, bevor solche Experimente auch tatsächlich durchgeführt werden können.

Der erste Teil dieser Dissertation beschäftigt sich mit Laser-getriebenen Plasmabeschleunigern (engl: Laser wake field accelerator, LWFA) und deren Weiterentwicklung. Besonderes Augenmerk liegt dabei auf der Verbesserung der Stabilität und der Selbstinjektion der Plasmabeschleunigung. In dieser Arbeit wird gezeigt, dass die Gasdynamik auf einer $\sim 10\,\mu$m-Skala, die bisher nicht gemessen werden konnte, großen Einfluss auf den LWFA-Beschleunigungsprozess hat. Dichtemodulationen auf einer Skala von $10\,\mu$m wurden mithilfe eines ultrakurzen Laserpulses in Plasmen vermessen, die durch die Fokussierung des Hochintensitätslasers in einen Gasjet erzeugt wurden. Es wird gezeigt, dass diese Dichtemodulationen die Selbstinjektion in diesem Plasma auslösen. Die Resultate werden sowohl durch ein analytisches Modell sowie Particle-in-Cell (PIC) Simulationen bestätigt. Zur Unterdrückung der Selbstinjektion wurde eine Gaszelle mit homogenem Dichteprofil entwickelt. Mit dieser konnte gezeigt werden, dass Selbstinjektion unterdrückt werden kann und sich somit Strahlprofil und Richtungsstabilität dramatisch verbessern. Diese Erkenntnisse ebnen den Weg zu einem Plasmabeschleuniger bei dem Injektions- und Beschleunigsprozess unabhängig voneinander kontrolliert werden können. Darüber

hinaus wurde in dieser Arbeit ein neues Kriterium für die Homogenität der Plasmadichte eingeführt, das auch in einem allgemeinen Kontext für Plasmabeschleuniger gilt.

Im zweiten Teil der Dissertation wird untersucht, inwiefern kurze Elektronenpulse in Plasmen fokussiert werden können. LWFA Elektronenstrahlen weisen typischerweise eine sehr kleine Quellgröße, aber eine Divergenz von einigen mrad auf, was zu einem schnellen Abfall der Elektronendichte während der Freiraumpropagation führt. Für viele der angedachten QED Experimente ist es daher notwendig, den Strahl zu fokussieren. In dieser Arbeit wird erstmalig das Konzept der passiven Plasmalinse mit ultrakurzen LWFA-Elektronenpulsen untersucht. Sowohl Experimente als auch Simulationen demonstrieren den Effekt der passiven Plasmalinse. Es wurde zudem ein analytisches Modell entwickelt, welches die experimentellen Ergebnisse beschreibt. Es ist hervorzuheben, dass die gemessene Fokussierstärke die eines konventionellen Quadrupolmagneten deutlich übersteigt. Das Modell sagt des Weiteren eine Steigerung der Fokussierstärke für Elektronenpulse mit größerer Ladung voraus.

Die in dieser Arbeit vorgestellten Resultate zur Verbesserung und Fokussierung von laserbeschleunigten Elektronenpulsen könnten einen wichtigen Beitrag zur Realisierung der QED Experimente beitragen.

Abstract

Quantum electrodynamics (QED) is widely considered to be one of the most accurately tested theories. Nevertheless fundamental processes such as pair production from the vacuum or the motion of the electron in extreme fields have not been measured in the laboratory to date. Their measurement requires a high intensity laser together with a high intensity electron or γ-beam, which can be produced by a high density electron bunch.

A recent development within the last two decades are plasma based accelerators. The high fields that can be sustained by a plasma are used to deliver extremely short and dense electron bunches while shrinking size and costs of the device. Importantly, they are automatically co-located with and synchronized to a high intensity laser pulse, providing an ideal basis for investigating QED in high fields.The availability of generating dense electron bunches brings new QED experiments within reach. However, the quality and stability of laser wake field accelerated (LWFA) electron beams still has to be improved to make these experiments possible. Beyond the tests of QED, the stability and quality of the electron beam is also crucial for highly demanding applications such as LWFA-driven free-electron lasers.

The first part of this thesis is devoted to the LWFA process and its improvements with a particular emphasis on improving the stability of laser plasma accelerators. It is shown that the gas dynamics on a $10\,\mu$m scale plays an important role in LWFA, which has not been fully appreciated yet. Density modulations on a $10\,\mu$m scale were measured in a gas jet using a few-cycle probe pulse. It is shown that self-injection can be triggered by these modulations. Particle-in-cell (PIC) simulations and analytical modeling confirm the experimental results. A gas cell providing a homogeneous plasma density has been developed in order to reduce self-injection. Using this gas cell, it was possible to suppress self-injection. The experiments show that self-injection was suppressed in the gas cell. Using ionization injection and the gas cell, the beam shape as well as the pointing stability were strongly improved. This finding paves the way towards self-injection free acceleration in a plasma based accelerator. It also establishes a new requirement on the homogenouity of the plasma density – not only for LWFA, but also in a broader context, for example in particle driven plasma wake field acceleration (PWFA).

In the second part of this, the possibility of focusing the ultra-short electron bunch by passive plasma lensing is studied. LWFA-beams typically have a very small source size and a divergence of the order or a few mrad, resulting in a rapid drop in electron beam density during free-space propagation. Many of the envisioned experiments, however, require intense focused electron bunches. Therefore, the concept of passive plasma lensing

has been applied to ultra-short LWFA-bunches for the first time. The passive plasma lens effect was demonstrated experimentally by using a second gas target with predefined density. PIC simulations and analytical modeling describe the measured effect. Notably, the observed focusing strength of the passive plasma lens is larger compared to a conventional magnetic quadrupole lens. The analytical model predicts that the focusing strength can be further enhanced by increasing the bunch charge.

Contents

1 Introduction

The development of particle accelerators has continuously pushed the boundaries of experimental physics and allowed new theories to be tested. For example, collisions of particles have lead to the discovery of the Higgs-Boson in 2012 at the large hadron collider (LHC) at CERN. Accelerators are particularly powerful experimental tools because of their well controlled particle beams and stable operation, which is essential for the statistical analysis of the experimental data. Nowaday's particle accelerators can be combined with high intensity lasers, which allows the creation of more extreme conditions and high fields in the laboratory.

The most extreme limit of quantum electrodynamics (QED) is the so-called *Schwinger-limit*, which has been predicted by Fritz Sauter [Sauter 1931] and further investigated by Julian Schwinger [Schwinger 1951]: Similar to an atom, which becomes ionized in a strong external electric field, the quantum-vacuum is limited by a maximum electric field strength it can sustain, before electron-positron pairs are created. This electric field strength, $E_{\mathrm{S}} = \frac{m_e^2 c^3}{e\hbar} \approx 1.3 \cdot 10^{18}\,\mathrm{V/m}$, is refered to as the Schwinger limit. The Schwinger-limit of QED directly implies a non-linear vacuum response when the field strength becomes strong enough. This non-linear vacuum response leads to several effects as photon-photon scattering, vacuum-birefringence or electron-positron pair production. However, the direct observation and a measurement of their cross-sections of these effects is still subject to research. E144 is one famous experiment, that has been carried out at the Stanford Linear Accelerator Center (SLAC) in 1996, confirming the existence of the non-linear Breit-Wheeler pair production process ($\gamma + n \cdot \hbar\omega \rightarrow e^- + e^+$) [Burke et al. 1997]. The high energy γ-photons were created by Compton back-scattering from a focused laser beam with the 46.6 GeV SLAC electron beam. The high energy γ-beam was then overlapped with a high intensity laser pulse to create electron-positron pairs. However, the measurement relied on the modelling of different processes [Hu et al. 2010] and it is still ongoing research to measure the cross section of the pair production process. Another example is the first order fundamental process, the linear Breit-Wheeler pair production ($\gamma + \gamma' \rightarrow e^- + e^+$), which has not been measured in the laboratory to date. Due to its low cross section ($\sigma_{\gamma\gamma} \sim 10^{-29}\,\mathrm{m}^2$, see figure 1.1) experiments require the
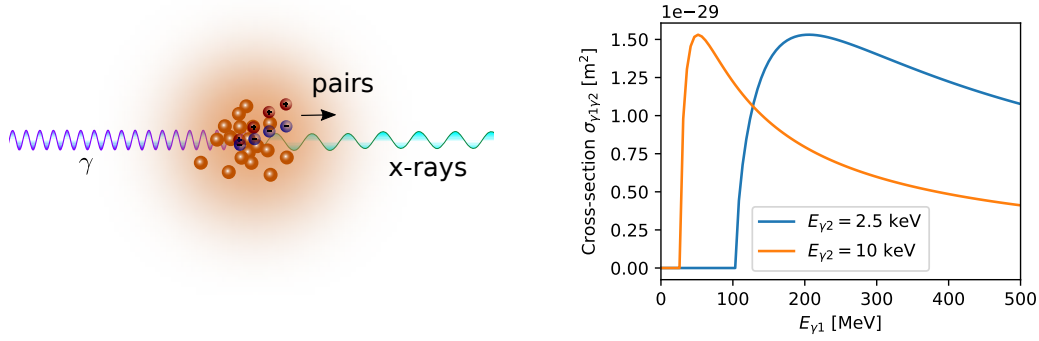
Figure 1.1: *The collision of an γ and a x-ray beam creates an electron-positron pair from the quantum vacuum. This is the so called Breit-Wheeler process. The left shows an illustration of the process, the right shows the energy dependent cross section for two different energies of the x-ray beam. The equation for $\sigma_{\gamma\gamma}$ was taken from Ruffini et al. 2010, eq. 23. The cross section $\sigma_{\gamma\gamma}$ drops to zero for below threshold energies. At this point the energy of the two γ photons drops below* 511 keV *in the rest frame of the interaction, which is insufficient to create an electron positron pair.*

collision of two intense γ-beams. In conclusion, experimental studies on a high field QED processes require a combination of high fields, γ-beams or electron-beams.

Laser wake field accelerators (LWFA) create electron bunches which are inherently synchronized to a high intensity laser pulse. This makes LWFA an ideal platform for the investigation of nonlinear QED processes. An example for an envisioned QED experiment is shown in figure 1.2. Electrons are accelerated using LWFA in a gas cell. In a next step, electrons are refocused and interact with a high-Z target, producing directed γ-ray beams that can interact with lower energy photon beam.

First experiments [Poder et al. 2017a] reveal that the current stability of LWFA in terms of pointing, beam quality and spectral shape can be an issue for high-field QED experiments: Random fluctuations of the laser plasma accelerator compromise the overlap of the (photon-)beams, which are supposed to collide, and may worsen the statistical significance of the experiment. Therefore, a focus of this thesis is the understanding and mitigation of beam fluctuations in laser plasma accelerators. It is important for laser-based high-field QED experiments that the high standards of conventional particle collider experiments are met.

Another important aspect of these experiments is the possibility to focus the electron or γ-beam. While electron bunches are often focused by conventional and large devices such as quadrupole magnets, plasma lenses have attracted notable interest in the last years due to their high field strength and very compact setup [Tilborg et al. 2015; Thaury
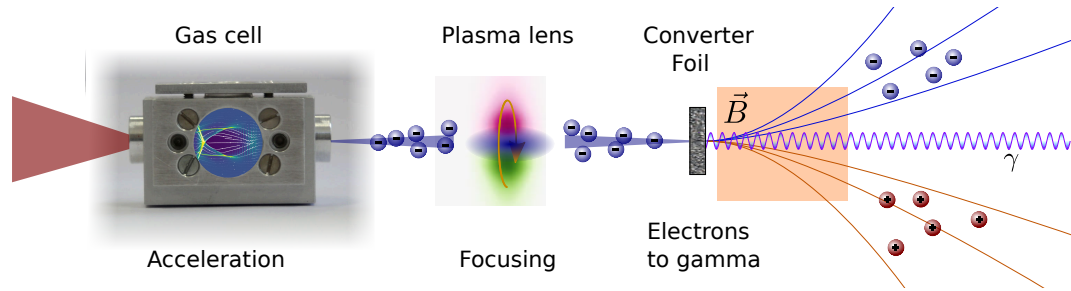
Figure 1.2: *An envisioned setup for various future experiment: Laser driven electron acceleration in the gas cell creates electron bunch with increased stability. These bunches are refocused by a compact plasma lens and then used in secondary experiments. In this case they are focused onto a converter foil to create a high intensity γ burst or a positron beam. This thesis focuses on the stable acceleration and the refocusing of the electrons using a passive plasma lens.*

et al. 2015]. In this thesis, the concept of passive plasma lensing is demonstrated and its use for possible applications is assessed.

In addition to the envisioned QED experiments, a laser plasma accelerator with improved stability and density has also other applications. Examples include the development of an all-optical free-electron laser, particle-driven wake field accelerator (PWFA) or the coupling of an LWFA electron bunch into a conventional accelerator.

1.1 Thesis outline

The fundamentals of laser plasma interactions and their modeling by computer simulations are described in Chapter 2. Starting with the motion of a single particle in a laser field, all calculations will be carried out using the Hamilton formalism. This treatment strongly simplifies the calculations compared to the typical description in the literature using electric and magnetic fields. Thereafter, the working principle of particle-in-cell (PIC) simulations is outlined. They are valuable tools for the simulation of laser plasma interactions and have also been used in this thesis for the interpretation of the experimental results. A post-processing package (*postpic*) has been developed in python. Postpic is used by an international community and the first open-source, GPL licensed project focusing on post-processing of PIC simulation data.

In Chapter 3, the theory of laser wake field acceleration (LWFA) is presented. First, a 1D model of the plasma wake is introduced. Scaling laws in higher dimensions and different injection schemes are discussed. In particular, the working principle of wave breaking and its relation to the slow down of the phase velocity of the plasma wake β_p is

studied. This is necessary to understand the results using the gas cell and the physical reason behind the increased stability of the laser plasma accelerator (Chapter 4).

A comparison of experiments using the gas cell and the gas jet is presented in Chapter 4. The most obvious difference between both targets is the improved pointing stability by one order of magnitude, when using the gas cell. It was found that wave breaking is triggered by density modulations within the flow of the gas jet as revealed by the plasma wave images (section 4.4). In particular, the unique imaging technique using few-cycle laser pulses is used to measure small scale density modulations quantitatively for the first time. These density modulations are identified as the leading contribution to wave breaking using the gas jet. For the new gas cell, in contrast, background free acceleration could be realized. Consequently, the density homogeneity has to be taken into account for stable and controlled plasma based accelerators. A publication is in preparation.

Chapter 5 will introduce the concept of plasma lensing. A general model will introduced, which is valid for long bunches. Different regimes are investigated using PIC simulations and post-processing by postpic.

Experiments investigating the passive plasma lensing have been performed with the impoved pointing and beam stability using the gas cell. The experimental resuls are presented in Chapter 6. In addition to the work published in Kuschel et al. 2016, the experimental data was reproduced quantitatively by a model based on the beam envelope equation (section 6.3).

A complete list of publications can be found in Appendix B.

2 Relativistic laser plasma interaction

This chapter will introduce some basic concepts of plasma physics by discussing the movement of a single electron within a laser field.

2.1 A free electron in a linearly polarized laser field

The movement of a single free electron inside an electromagnetic field is often described by solving the equation of motion in the electric $\boldsymbol{E}(\boldsymbol{r}, t)$ and magnetic $\boldsymbol{B}(\boldsymbol{r}, t)$ field given by the Lorentz force

$$m\boldsymbol{a} = \boldsymbol{F}_{\text{Lorentz}} \tag{2.1}$$

$$m\ddot{\boldsymbol{r}} = q(\boldsymbol{v} \times \boldsymbol{B}) + q\boldsymbol{E}. \tag{2.2}$$

Taking relativistic effects into account also requires $m \to m/\gamma$ for the single particle trajectory. Therefore this approach will soon result in a rather long calculation.

$\boldsymbol{E}$ and $\boldsymbol{B}$ fields are given by the vector potential $\boldsymbol{A}$ and the scalar potential φ

$$\boldsymbol{E} = -\partial_t \boldsymbol{A} - \nabla\varphi \tag{2.3}$$

$$\boldsymbol{B} = \nabla \times \boldsymbol{A}. \tag{2.4}$$

The relativistic Hamiltonian of a charged particle inside an externally given electromagnetic field is given by [Jackson 2006]

$$H = c \cdot \sqrt{(\boldsymbol{P} - q\boldsymbol{A})^2 + m^2c^2} + q\varphi \tag{2.5}$$

with $\boldsymbol{P} = \boldsymbol{p} + q\boldsymbol{A}$. Here $\boldsymbol{P}$ is called the canonical momentum.

The absence of external charges implies $\varphi \equiv 0$. The laser field is described by a plane wave pulse, i. e. a plane wave with an envelope depending on time. It is further assumed

that the propagation direction is z. Consequently the vector potential will only depend on z and t, which means $\boldsymbol{A} = \boldsymbol{A}(z,t)$. The equations of motion read:

$$\dot{x} = \frac{\partial H}{\partial P_x} = \frac{P_x - qA_x}{\sqrt{(\boldsymbol{P} - q\boldsymbol{A})^2 + m^2 c^2}} \quad , \quad -\dot{P}_x = \frac{\partial H}{\partial x} = 0 \tag{2.6}$$

$$\Rightarrow P_x = p_x + qA_x = c_x \tag{2.7}$$

$$\dot{y} = \frac{\partial H}{\partial P_y} = \frac{P_y - qA_y}{\sqrt{(\boldsymbol{P} - q\boldsymbol{A})^2 + m^2 c^2}} \quad , \quad -\dot{P}_y = \frac{\partial H}{\partial y} = 0 \tag{2.8}$$

$$\Rightarrow P_y = p_y + qA_y = c_y \tag{2.9}$$

$$\dot{z} = \frac{\partial H}{\partial P_z} = \frac{P_z - qA_z}{\sqrt{(\boldsymbol{P} - q\boldsymbol{A})^2 + m^2 c^2}} \quad , \quad -\dot{P}_z = \frac{\partial H}{\partial z} = -cq\frac{(\boldsymbol{P} - q\boldsymbol{A}) \cdot \partial_z \boldsymbol{A}}{\sqrt{(\boldsymbol{P} - q\boldsymbol{A})^2 + m^2 c^2}} \tag{2.10}$$

It turns out that the transverse canonical momenta $\boldsymbol{P}_\perp = \begin{pmatrix} P_x \\ P_y \end{pmatrix}$ are constants of motion (c_x, c_y) for relativistic treatment and arbitrary short pulses. Note that the only assumption used to derive this result was the form of the vector potential $\boldsymbol{A} = \boldsymbol{A}(z,t)$, not even its actual dependence on z and t. (c_x, c_y) are often called the first and second constant of motion.

For an electron, which is initially at rest (meaning a long time before the wave arrives $\boldsymbol{A}(z = 0, t \to -\infty) = \boldsymbol{0}$), these constants are 0:

$$c_x = c_y = 0 \tag{2.11}$$

It follows that

$$\boxed{p_x = qA_x = 0} \tag{2.12}$$

$$\boxed{p_y = qA_y} \tag{2.13}$$

Equation 2.13 is an important result: The momentum of a free electron, which was initially at rest, is equal to the y-component of the vector potential. Since the y-component of the vector potential oscillates periodically in time, the electron will move periodically along the polarization direction. This is the motion due to the electric field of the electromagnetic wave. Equation 2.13 also shows that the transverse momenta of the electron return to 0, once the EM wave has passed in this special case. However, introducing also transverse gradients, the electron may be scattered by the EM pulse (see section 2.1.2).

Together with the classical velocity-momentum relation, equation 2.13 reads $mv_y = qA_y$ and the maximum velocity v_y^{max} the particle acquires during the wave is given by

$$\frac{v_y^{\mathrm{max}}}{c} = \left| \frac{qA_0}{mc} \right| := a_0. \tag{2.14}$$

This is the definition of the *normalized vector potential* a_0, which is typically used to express the field strength in relativistic units. For $a_0 \gtrsim 1$, relativistic effects need to be taken into account when calculating the particle trajectory. Therefore an intensity, which leads to $a_0 \gtrsim 1$, is called "relativistic intensity",

$$a_0 = \frac{eE_0}{\omega m_e c} = \lambda \cdot \sqrt{\frac{I}{1.37 \cdot 10^{18} \, \frac{\mathrm{W}}{\mathrm{cm}^2}}} \tag{2.15}$$

with the wavelength λ in μm and the intensity I in units of $\mathrm{W/cm^2}$. With a common Titanium:Sapphire laser system, which operates at $\lambda = 800\,\mathrm{nm}$, an intensity of $I = 2.14 \cdot 10^{18}\,\frac{\mathrm{W}}{\mathrm{cm}^2}$ corresponds to $a_0 = 1$.

For $a_0 \ll 1$, the movement of the particle can be treated non-relativistically and the forces due to the magnetic field of the electromagnetic wave can be neglected. Thus the non-relativistic particle motion in the linearly polarized wave is entirely described by equation 2.13. This periodic motion is the origin of Thomson scattering as well as plasma dispersion (next section) or the ponderomotive potential (section 2.1.2).

2.1.1 Plasma frequency and dispersion relation

In the non-relativistic limit, the motion of the particle is given by equation 2.13 and $z = 0$ can be assumed for all times:

$$v_y = \frac{qA_0}{m} \sin(-\omega t) \tag{2.16}$$

$$y = \frac{qA_0}{m\omega} \cos(-\omega t) \tag{2.17}$$

The particle is displaced periodically, which induces a polarization. Assume that there is not only a single particle, but an electron density n_e following the exact same movement,

this induces a polarization density $\boldsymbol{P}$, q is the charge of the electron.

$$\boldsymbol{P} = y \cdot qn \tag{2.18}$$

$$= qn \frac{q\boldsymbol{A}_0}{m\omega} \cos(-\omega t) \tag{2.19}$$

$$= \frac{q^2 n \boldsymbol{A}_0}{m\omega} \cos(-\omega t) \tag{2.20}$$

$$= \frac{q^2 n}{m\omega^2} \underbrace{\boldsymbol{E}_0 \cos(-\omega t)}_{E} \tag{2.21}$$

Thus a plasma induces a polarization depending on the external electric field. If an electromagnetic wave is passing through a plasma this additional polarization acts back on the wave. The polarization becomes the inhomogeneous part of the wave equation, which then reads

$$\nabla^2 \boldsymbol{E} - \frac{1}{c^2} \partial_t^2 \boldsymbol{E} = \frac{1}{\varepsilon_0 c^2} \partial_t^2 \boldsymbol{P} \tag{2.22}$$

$$\nabla^2 \boldsymbol{E} - \frac{1}{c^2} \underbrace{\left(1 - \frac{1}{\varepsilon_0} \frac{q^2 n}{m\omega^2}\right)}_{\varepsilon} \partial_t^2 \boldsymbol{E} = 0, \tag{2.23}$$

where ε is the permittivity of a cold plasma. Electromagnetic waves can only propagate through the plasma if $\varepsilon > 0$. As ω decreases, ε becomes negative and low frequency electromagnetic waves are damped inside the plasma. As a result, a plasma has a characteristic frequency separating the two regimes – the so called "plasma frequency" ω_p:

$$\boxed{\omega_p^2 = \frac{1}{\varepsilon_0} \frac{q^2 n}{m}} \tag{2.24}$$

The permittivity of the plasma simplifies to

$$\varepsilon = 1 - \frac{\omega_p^2}{\omega^2}. \tag{2.25}$$

Equivalently, the "critical density" n_c is defined as

$$\boxed{n_c = \frac{\varepsilon_0 m}{q^2} \omega^2} \tag{2.26}$$

For a wavelength of $\lambda = 800\,\text{nm}$, the critical density is $n_c \approx 1.74 \cdot 10^{21}\,1/\text{cm}^3$.
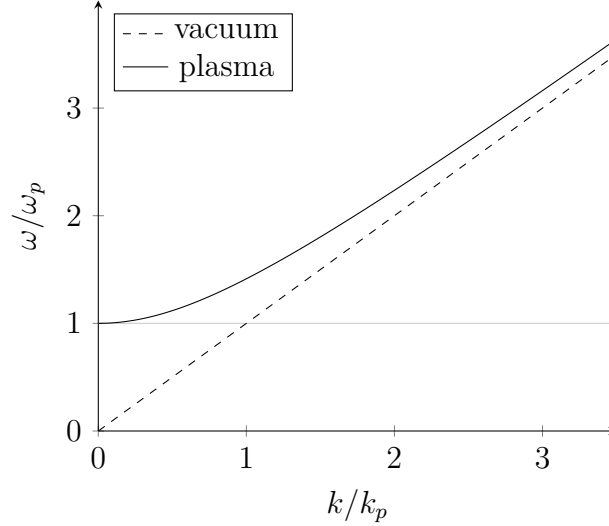
Figure 2.1: *Visualization of the plasma dispersion relation (equation 2.29): The solid line shows the dispersion relation $\omega(k)$ of an electromagnetic wave passing through a cold plasma. The lowest frequency allowed is the plasma frequency ω_p. The dashed line shows the vacuum dispersion relation for comparison.*

Optical properties of plasmas

While an EM wave can only propagate through a plasma if $\omega > \omega_p$, it still experiences the dispersion of the plasma. The dispersion relation can be obtained by inserting the vacuum solution for a plane wave $E_y = E_0 e^{i(\omega t - kz)} + \text{c.c.}$ into the wave equation (equation 2.23):

$$k^2 = \varepsilon \frac{\omega^2}{c^2} \tag{2.27}$$

$$k^2 = \frac{\omega^2}{c^2} - \frac{\omega_p^2}{c^2} \tag{2.28}$$

which is usually written in the form

$$\boxed{\omega^2 = k^2 c^2 + \omega_p^2} \tag{2.29}$$

This dispersion relation $\omega(k)$ is visualized in figure 2.1 as the solid line. The lowest frequency allowed in the plasma is ω_p. Towards high frequencies the dispersion relation converges towards the vacuum dispersion relation.

The refractive index η of the plasma follows by definition

$$\eta = \sqrt{\varepsilon} = \sqrt{1 - \frac{\omega_p^2}{\omega^2}}. \tag{2.30}$$

The refractive index of a plasma is therefore always smaller than unity ($\eta < 1$) and it is increasing with increasing ω, thus $\frac{\partial \eta}{\partial \omega} > 0$. For $\omega < \omega_p$ the dielectric constant becomes imaginary, which results in reflection and absorption of the EM wave.

The phase velocity of a light wave in a plasma ,$\frac{\omega}{k} = c/\eta$, is therefore always faster than the speed of light. However its group velocity is always slower than c

$$v_g = \frac{d\omega}{dk} = c \cdot \eta = c \cdot \underbrace{\sqrt{1 - \frac{\omega_p^2}{\omega^2}}}_{\beta_g} . \tag{2.31}$$

Typical plasma densities used in LWFA are in the range of some percent of the critical density or less, which means $\omega_p^2/\omega^2 \ll 1$. In that limit, the group velocity v_g can be approximated by

$$v_g \approx c \cdot \left(1 - \frac{1}{2}\frac{\omega_p^2}{\omega^2}\right). \tag{2.32}$$

Note that the gamma factor of the group velocity of the laser pulse (γ_g) in a plasma takes a very simple form even without any approximation:

$$\gamma_g = \frac{1}{\sqrt{1 - \beta_g^2}} \tag{2.33}$$

$$\gamma_g = \frac{\omega}{\omega_p} = \sqrt{\frac{n_c}{n_p}}. \tag{2.34}$$

This is a useful formula to calculate the γ-factor of an ultra-short laser pulse passing through a plasma.

2.1.2 Ponderomotive Potential

The periodic movement of a free electron inside an EM wave is described by equation 2.13. This movement along the polarization direction can be attributed to the electric field of the EM wave. In case of a focused laser pulse, this leads to a drift of the electron along intensity gradients: An electron moves outwards of the focus, but the electric force pushing it back is slightly smaller in its new position (due to the gradient). The residual momentum is experienced as a drift of the electron towards regions with lower intensity. This so called "ponderomotive force" can be described as the gradient of the

ponderomotive potential [Bauer et al. 1995; Lamb et al. 1983]

$$\phi_{\text{pond}} = \frac{e^2}{4m\omega^2} \boldsymbol{E}^2. \tag{2.35}$$

A laser pulse passing through a plasma will therefore tend to push the electrons away from regions of high intensity.

2.1.3 Relativistic Motion

The relativistic particle motion, parallel to the laser propagation direction (which can be attributed to the magnetic force of the electromagnetic wave) is discussed. Using equation 2.10 and assuming further a linearly polarized laser pulse in y-direction implying $A_x = A_z = 0$ yields:

$$-\dot{P}_z = \frac{\partial H}{\partial z} = -cq\frac{(P_y - qA_y) \cdot \partial_z A_y}{\sqrt{(\boldsymbol{P} - q\boldsymbol{A})^2 + m^2c^2}} + q\partial_z\varphi \tag{2.36}$$

which simplifies further using $P_x \equiv P_y \equiv 0$ (equation 2.11)

$$= cq\frac{qA_y\partial_z A_y}{\sqrt{(qA_y)^2 + p_z^2 + m^2c^2}} + q\partial_z\varphi \tag{2.37}$$

and $p_y = qA_y$ (equation 2.13)

$$= cq\frac{qA_y\partial_z A_y}{\sqrt{p_y^2 + p_z^2 + m^2c^2}} + q\partial_z\varphi \tag{2.38}$$

$$= \frac{cq}{mc}\frac{qA_y\partial_z A_y}{\sqrt{\left(\frac{p_y}{mc}\right)^2 + \left(\frac{p_z}{mc}\right)^2 + 1}} + q\partial_z\varphi \tag{2.39}$$

$$= \frac{q^2}{m}\frac{A_y\partial_z A_y}{\gamma} + q\partial_z\varphi \tag{2.40}$$

$$-\dot{P}_z = -\dot{p}_z - q\dot{A}_z = \frac{q^2}{2m}\frac{\partial_z A_y^2}{\gamma} + q\partial_z\varphi \tag{2.41}$$

with $A_z \equiv 0$ and $\varphi \equiv 0$ this reduces to

$$\boxed{\dot{p}_z = -\frac{q^2}{2m}\frac{\partial_z A_y^2}{\gamma}} \tag{2.42}$$
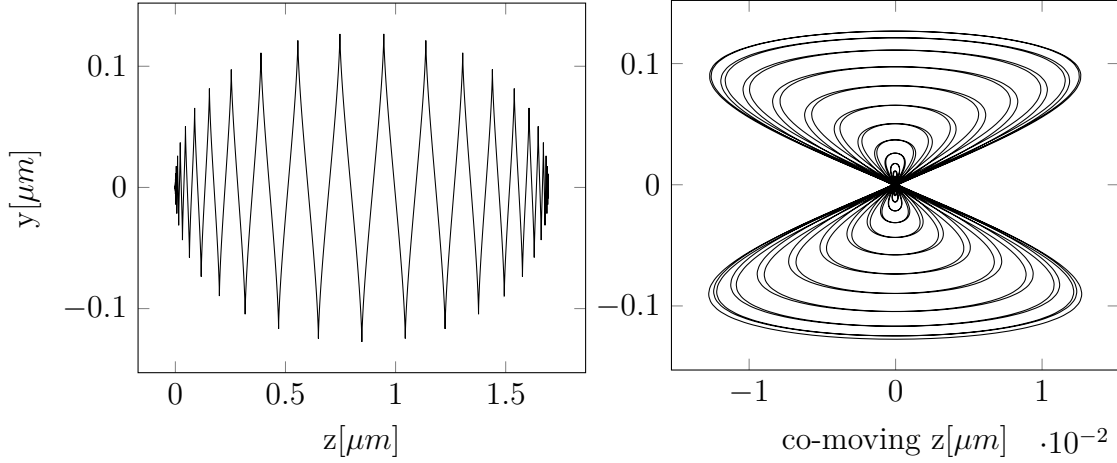
Figure 2.2: *The trajectory of a single electron in an electromagnetic plane wave pulse with a duration of 30 fs (FWHM) and $a_0 = 1$: The left panel shows the movement as seen in the lab frame. The particle is moving periodically up and down (y-direction) due to the periodic change of the electric field. Additionally a shift in z-direction (propagation of the laser pulse) can be observed. Once the pulse is over the particle is left displaced, but at rest again.*
The right panel shows the exact same movement in a co-moving frame with the electron: The trajectory shows the characteristic "figure-8-motion".

Equations 2.12, 2.13 and 2.42 form a set of equations which can be used to solve the relativistic single particle dynamics for any given vector potential of the form $\boldsymbol{A} = A_y(z,t) \cdot \boldsymbol{e}_y$.

Figure-8-motion

For example the plane wave pulse with a pulse duration σ_t is introduced

$$\boldsymbol{A}(z,t) = A_0 \exp\left(\frac{-(z/c - t)^2}{2\sigma_t^2}\right) \sin(kz - \omega t)\boldsymbol{e}_y. \tag{2.43}$$

Figure 2.2 shows an electron trajectory calculated for a pulse with a peak $a_0 = 1$, $\lambda = 800\,\mathrm{nm}$ and the FWHM duration of 30 fs. The left panel shows the particle motion in y-direction due to the electric field, and it also shows the particle displacement in propagation direction of the wave due to the magnetic field.

The right panel of figure 2.2 shows the same movement within a co-moving frame of the particle. This is often referred to as the "figure-8-motion" of the electron in a relativistic laser field.

2.2 Particle-in-cell simulations

Particle-in-cell simulations (PIC) are an important tool to model interactions of high intensity laser pulses with a plasma. Due to their ability to describe non-equilibrium systems and crossing particle trajectories, they are able to simulate various experiments and are widely used in the field of relativistic laser plasma physics.

A PIC simulation consists of two major components: The first part is the $\boldsymbol{E}$ and $\boldsymbol{B}$ fields which are represented by their values on a predefined grid – the simulation box. They can be evaluated in time by solving Maxwell's equations numerically:

$$\frac{\partial \boldsymbol{B}}{\partial t} = -\nabla \times \boldsymbol{E} \qquad\qquad \mu_0 \varepsilon_0 \frac{\partial \boldsymbol{E}}{\partial t} = \nabla \times \boldsymbol{B} - \mu_0 \boldsymbol{J} \qquad (2.44)$$

The second part is the ensemble of particles. Many charged particles – typically in the range of 10^7 to 10^9 – are added to the simulation. They are representing the plasma and since the position and the momentum of every single particle is known, all required quantities (like plasma density, charge density, current, temperature, ...) can be calculated from the ensemble. Their trajectories are calculated independently by solving each individual equation of motion:

$$\frac{d\boldsymbol{x}}{dt} = \boldsymbol{v} \qquad\qquad \frac{d\boldsymbol{p}}{dt} = \boldsymbol{F}_{\mathrm{Lorentz}} = q(\boldsymbol{v} \times \boldsymbol{B}) + q\boldsymbol{E} \qquad (2.45)$$

The movement of the charged particles creates a current $\boldsymbol{J}$, which is calculated on the grid and then in turn reinserted into Maxwell's equations (equation 2.44) and the cycle starts from the beginning. This PIC cycle is visualized in figure 2.3 and continues until the end of the simulation.

The particle positions and momenta are not bound to the simulation grid. They are floating point values, such that a particle position is resolved much better than the grid resolution. Therefore interpolation between the cells is used when calculating $\boldsymbol{F}_{\mathrm{Lorentz}}$ and care must be taken when calculating the currents on the grid from the particle positions and momenta. This numerical interpolation compromises the signal-to-noise ratio of the simulation.

PIC simulations in this thesis were performed using the open-source code EPOCH [Arber et al. 2015] and the JUROPA cluster at the Jülich supercomputing center (JSC).
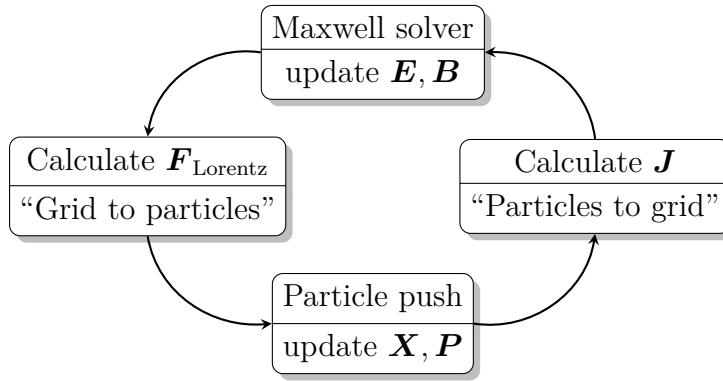
Figure 2.3: *The PIC cycle: After advancing E and B fields, the Lorentz force $F_{Lorentz}$ is calculated for every particle within the simulation. With these forces, all particle momenta P and in turn all particle positions X are updated. The moving charges create a current J on the simulation grid, which is inserted into Maxwell's equations during the next iteration. This cycle continues to evaluate the system of EM fields and particles.*

2.3 Post-processing of PIC simulations

The result of a PIC simulation typically consists of the electric and magnetic field as well as the particle positions and momenta. This data needs to be post-processed and scaled down before it can be visualized. Typical tasks include the calculation of the plasma density, temperature or a phase space map from individual particle positions. A python module called postpic has been developed to simplify post-processing. Postpic is open source, licensed under GNU public license v3+ and freely available via its main repository at `https://github.com/skuschel/postpic`.

The particular strength of postpic is the way it can handle particle data: A particle object can represent an ensemble of different species, each consisting of a quantity of many individual macro particles. Calculations of new particle quantities (like the direction of movement or the γ-factor) are then calculated on a single command, while postpic ensures that different particle species are handled correctly. Newer features contain k-space reconstruction from the electromagnetic fields or tracing particles through the simulation via their unique particle IDs (as used in the video of figure 3.4). Also axis transformations are implemented. Postpic currently supports the data format of EPOCH [Arber et al. 2015] and the open particle mesh data (openPMD[1]) format, which is currently used by the codes PIConGPU [Bussmann et al. 2013] and WARP [Grote et al. 2005]. Postpic is agnostic to the data format and it can therefore easily be extended.

---

[1]`https://github.com/openPMD/openPMD-standard`

3 Plasma based electron acceleration

The understanding of the injection and acceleration process in a non-linear plasma wave is important for the improvement of laser plasma accelerators. A 1D nonlinear plasma model is derived. Different injection processes – where some of the electrons enter the accelerating phase of the plasma wave – are discussed. Most importantly, the origin of wave breaking is shown and linked to the phase velocity of the plasma wake β_p (equation 3.43). This will be used later to explain the different behavior of the gas jet and the gas cell (Chapter 4).

3.1 One-dimensional plasma waves

In this section, a 1D nonlinear model for the plasma wake response will be introduced. The result of this derivation will be equation 3.34, which will be further discussed later. A much shorter derivation can be found in [Sprangle et al. 1990; Brancolini 2016]. The 1D fluid equations were derived with the help of Dr. Vasily Kharin.

3.1.1 Derivation of 1D plasma fluid equations

For simplicity, a normalised CGS unit system will be used throughout this section. The vector potential A is normalized to $a = \frac{eA}{mc}$ and CGS units imply $c = 1$, $m = 1$ and $u = \gamma\beta$, where $\gamma = \sqrt{1 + \boldsymbol{u}^2}$.

This 1D model uses the same assumptions as introduced in section 2.1.3: A plane wave is propagating in z direction with an additional temporal envelope. The linear polarization direction is y. Therefore $\boldsymbol{A} = A(z, t) \cdot \boldsymbol{e}_y$. In order to obtain the equations of motion for the kinetic momentum p_z, the total derivative of the canonical momentum $P_z = u_z + a_z$

needs to be expanded

$$\dot{P}_z = \frac{dP_z}{dt} = \partial_t u_z + \underbrace{\partial_t a_z}_{=0} + \underbrace{(\boldsymbol{v} \cdot \nabla)u_z}_{v_z \partial_z u_z} + (\boldsymbol{v} \cdot \nabla)\underbrace{a_z}_{=0} \tag{3.1}$$

$$= \partial_t u_z + \frac{u_z}{\gamma}\partial_z u_z. \tag{3.2}$$

Substituting the result from equation 2.41 yields (note that $q = -1$)

$$-\frac{\partial_z a_y^2}{2\gamma} + \partial_z \varphi = \dot{P}_z = \partial_t u_z + \frac{u_z}{\gamma}\partial_z u_z. \tag{3.3}$$

Given that $a_y = -u_y$ (equation 2.13), the general expression for γ can be rewritten as

$$\gamma = \sqrt{1 + a_y^2 + u_z^2} \tag{3.4}$$

$$a_y^2 = \gamma^2 - 1 - u_z^2 \tag{3.5}$$

$$\partial_z a_y^2 = 2\gamma\partial_z\gamma - 2u_z\partial_z u_z. \tag{3.6}$$

Combining equation 3.3 and equation 3.6 leads to

$$\frac{-2\gamma\partial_z\gamma + 2u_z\partial_z u_z}{2\gamma} + \partial_z\varphi = \partial_t u_z + \frac{u_z}{\gamma}\partial_z u_z \tag{3.7}$$

$$\partial_t u_z = \partial_z\varphi - \partial_z\gamma. \tag{3.8}$$

Additionally Poisson's equation is used and reads

$$\Delta\varphi = -4\pi\rho, \tag{3.9}$$

which can be rewritten as

$$\partial_z^2\varphi = 4\pi(n - n_0) \tag{3.10}$$

$$\partial_z^2\varphi = k_p^2\left(\frac{n}{n_0} - 1\right). \tag{3.11}$$

Finally, the inhomogeneous wave equation is used

$$\partial_t^2 a_y - \partial_z^2 a_y = 4\pi j_y. \tag{3.12}$$

With $j_y = -nv_y = -n\frac{u_y}{\gamma} = n\frac{a_y}{\gamma}$, it follows that

$$\partial_t^2 a_y - \partial_z^2 a_y = 4\pi n\frac{a_y}{\gamma}. \tag{3.13}$$

The plasma wave vector k_p is given by $k_p^2 = 4\pi n_0$. Thus the wave equation can finally be written as

$$\partial_t^2 a_y - \partial_z^2 a_y = k_p \frac{a_y}{\gamma} \frac{n}{n_0}. \tag{3.14}$$

Transformation into the moving window

This set of equations (3.8, 3.11 and 3.14) is now transformed to a frame that is co-moving with the laser pulse. The new coordinates ζ and τ are defined as

$$\zeta = z - \beta_p t \qquad\qquad \tau = t \tag{3.15}$$
$$\partial_z = \frac{\partial \zeta}{\partial z}\partial_\zeta + \frac{\partial \tau}{\partial z}\partial_\tau \qquad\qquad \partial_t = \frac{\partial \zeta}{\partial t}\partial_\tau + \frac{\partial \tau}{\partial t}\partial_\tau \tag{3.16}$$
$$= \partial_\zeta \qquad\qquad = -\beta_p \partial_\zeta + \partial_\tau \tag{3.17}$$

Since the plasma wake is moving with almost the speed of light, we can use the approximation $\beta_p \approx 1$. The derivatives with respect to z and t are then given in the moving frame as:

$$\partial_z = \partial_\zeta \qquad\qquad \partial_t = \partial_\tau - \partial_\zeta \tag{3.18}$$

The next step is to transform all three equations into the new coordinates. Since those are co-moving with the plasma wave, it is expected that the system is quasi-static in the new coordinates ζ, τ.

Equation 3.8 transforms to

$$(\partial_\tau - \partial_\zeta)u_z = \partial_\zeta \varphi - \partial_\zeta \gamma \tag{3.19}$$
$$\partial_\tau u_z = \partial_\zeta (u_z + \varphi - \gamma). \tag{3.20}$$

As we have transformed into the co-moving frame of reference, we can assume a quasi-static solution in τ. That assumption makes all derivatives with respect to τ equal to zero. It follows that $u_z + \varphi - \gamma$ is independent of τ and ζ and is constant. For electrons initially at rest in the lab frame ($u_z = 0, \varphi = 0, \gamma = 1$) this constant is equal to -1 and it follows:

$$\gamma - u_z = \varphi + 1 \tag{3.21}$$

Additionally we will also need the continuity equation:

$$\partial_t n + \partial_z(n v_z) = \partial_t n + \partial_z(n \frac{u_z}{\gamma}) = 0, \tag{3.22}$$

which can be transformed using equation 3.18

$$(\partial_\tau - \partial_\zeta) n + \partial_\zeta \left(n \frac{u_z}{\gamma} \right) = 0 \tag{3.23}$$

$$\partial_\tau n = \partial_\zeta \left(n \frac{\gamma - u_z}{\gamma} \right). \tag{3.24}$$

Using the quasi-static approximation, it follows that $n \frac{\gamma - u_z}{\gamma}$ is constant. For electrons which are initially at rest in the lab frame, this constant is given by the initial plasma density:

$$\frac{n}{n_0} = \frac{\gamma}{\gamma - u_z} \tag{3.25}$$

The transformation of equation 3.11 into the co-moving frame leads to

$$\partial_\zeta^2 \varphi = k_p^2 \left(\frac{n}{n_0} - 1 \right). \tag{3.26}$$

Combining this with equation 3.25

$$\partial_\zeta^2 \varphi = k_p^2 \left(\frac{\gamma}{\gamma - u_z} - 1 \right) = k_p^2 \left(\frac{u_z}{\gamma - u_z} \right) \tag{3.27}$$

and substituting equation 3.21 yields

$$\partial_\zeta^2 \varphi = k_p^2 \left(\frac{u_z}{\varphi + 1} \right). \tag{3.28}$$

This is almost the final differential equation for the wake potential φ. The last step is to rewrite u_z as a function of known quantities $u_z = u_z(\varphi, a_y)$. equation 3.5 will be rearranged

$$\gamma^2 - u_z^2 = 1 + a_y^2 \tag{3.29}$$

and expanded to

$$\gamma + u_z = \frac{1 + a_y^2}{\gamma - u_z}. \tag{3.30}$$

The substitution of equation 3.21 yields

$$\gamma + u_z = \frac{1 + a_y^2}{\varphi + 1} \tag{3.31}$$

and u_z can finally be rewritten as

$$u_z = \frac{1}{2} \underbrace{(\gamma + u_z)}_{\text{Eqn. 3.31}} - \frac{1}{2} \underbrace{(\gamma - u_z)}_{\text{Eqn. 3.21}} \tag{3.32}$$

$$= \frac{1}{2} \left(\frac{1 + a_y^2}{\varphi + 1} - (\varphi + 1) \right). \tag{3.33}$$

Thus the final ordinary differential equation for the wake potential φ can be written as

$$\boxed{\partial_\zeta^2 \varphi = \frac{k_p^2}{2} \left(\frac{1 + a_y^2}{(\varphi + 1)^2} - 1 \right)} \tag{3.34}$$

This equation describes the plasma wake response in 1D. The solution to this ordinary differential equation is the potential φ caused by the plasma for any given laser field $a_y(\zeta)$.

The second equation of this model can be derived by transforming equation 3.14 to the co-moving window:

$$(\partial_\tau - \partial_\zeta)(\partial_\tau a_y - \partial_\zeta a_y) - \partial_\zeta^2 a_y = -k_p^2 \frac{a_y}{\gamma} \frac{n}{n_0} \tag{3.35}$$

$$\boxed{(2\partial_\zeta - \partial_\tau) \partial_\tau a_y = k_p^2 \frac{a_y}{\gamma} \frac{n}{n_0}} \tag{3.36}$$

Both boxed equations together build the 1D nonlinear model. While equation 3.34 describes the evolution of the plasma $\varphi(\zeta, \tau)$ in the presence of a varying $a_y(\zeta, \tau)$, equation 3.36 describes the evolution of the laser field a_y in the presence of a varying potential φ. Due to simplifications which were used in the 1D model, all other plasma quantities, like density $n(\zeta, \tau)$, energy of the particles $\gamma(\zeta, \tau)$ or even the electric field $E_\zeta(\zeta, \tau)$ can be derived from the potential $\varphi(\zeta, \tau)$.

The plasma wake excitation takes place over many plasma wave periods and it is known from simulations and experiments [Sävert et al. 2015] that the plasma wave structure changes slowly over the propagation distance. This means, that a_y and φ will change only slowly in the co-moving window and thus their dependence on τ will be neglected in the following discussion.

3.1.2 Solution of 1D model

For the sake of simplicity, a constant laser pulse profile $a_y(\zeta)$ will be assumed for the discussion of the acceleration process within the plasma wake. In reality, laser pulses can change their shape and intensity due to self phase modulation, dispersion of the plasma or the loss of intensity due to ionization Schroeder et al. 2011.

Low amplitude limit

The nonlinear response (equation 3.34) simplifies to the differential equation of a driven harmonic oscillator for a small amplitude wake $\varphi \ll 1$:

$$\partial_\zeta^2 \varphi + k_p^2 \varphi = \frac{k_p^2}{2} a_y^2 \tag{3.37}$$

The function $\varphi(\zeta)$ oscillates with the linear plasma oscillation period of $\zeta = \frac{2\pi}{k_p}$ and is driven by the square of the vector potential a_y^2 which is proportional to the intensity of the laser.

Nonlinear solution

Current laser wake field accelerators make use of laser pulses with $a_0 > 1$. The strong laser field will excite plasma waves for which the small amplitude approximation $\varphi \ll 1$ becomes invalid. Therefore numerical solutions of the differential equation equation 3.34 are presented to visualize the nonlinearly driven plasma wave. As an example, the plasma density is set to $k_p = 1$ and $a_y(\zeta)$ is a Gaussian laser pulse[1] $a_y(\zeta) = a_0 \exp\left(\frac{-\zeta^2}{2\sigma_\zeta^2}\right) \sin(k_L\zeta)$. A quasi neutral plasma ($\varphi = 0$) is assumed as initial condition. Remember that within the deviation another initial condition has been already used: the electron fluid described is at rest in the lab frame before the laser pulse arrives ($u_z = 0, \gamma = 1$). This is a reasonable assumption for laser wake field experiments. Even if supersonic nozzles are used (see section 4.1), the flow velocity of the gas ($\sim$ km/s) is much smaller, than the relativistic velocities considered here.

The solutions for $\sigma_\zeta = 1$ and $k_L = 1/12$ are shown in figure 3.1. The top panel shows a low The potential along the plasma wake (blue) shows a harmonic oscillation as expected from the low amplitude limit (equation 3.37). With increasing a_0 the solution of the oscillation becomes nonlinear.

---

[1] of course the ODE can be solved numerically for arbitrary functions $a_y(\zeta)$.
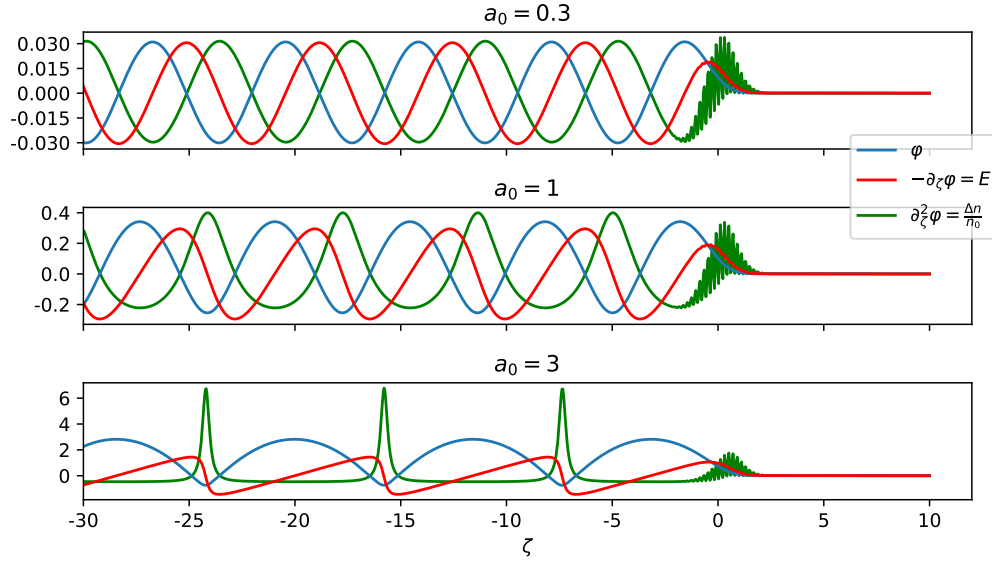
Figure 3.1: *Numerical solution of equation 3.34 for $k_p=1$ and different laser intensities: The laser pulse is traveling from left to right. The solution $\varphi(\zeta)$ is shown in blue, the resulting electric field in red and the relative density variation $\Delta n/n_0$ in green. It can be clearly seen, that the plasma wake is a harmonic oscillation for small amplitudes ($a_0 = 0.3$), but deforms to a nonlinear oscillation as a_0 is increased.*

Although this is only a very simple 1D model, some typical characteristics of the non-linear wake field can be identified:

- With increasing a_0, the plasma density (green) spikes periodically. Between the spikes, the plasma density is strongly reduced. However, in 2D or 3D it is possible that the electron density reduces to almost zero in the central plasma wake profile. This means that only the positive ions are left behind, while the negative electrons are completely expelled. This is the so called blowout regime. A model, specific to this regime will be introduced in section 3.2.5.

- The periodic spikes of the plasma density lead to an electric field showing a characteristic saw-tooth like profile. The electron acceleration takes place in regions where the electric field is negative, accelerating negative charges in forward direction.

- The period length of the nonlinear plasma wave is longer than the period length of the low amplitude plasma wake. This nonlinear lengthening is described by Sprangle et al. 1990 and has also been experimentally observed [Sävert et al. 2015].

- At the front, the imprint of the laser induced figure-8-motion is clearly visible in the density profile (Chapter 2).

3.2 LWFA: Laser wake field acceleration

This section will provide a visualization of phase space, which can already explain the principles of LWFA within the 1D fluid model. Different methods of injection will be introduced.

3.2.1 The separatrix

The solutions $\varphi(\zeta)$ of the potential in the plasma wake were discussed in the last section. This potential is formed by the plasma itself in reaction to the strong laser pulse. Now, the potential $\varphi(\zeta)$ will be seen as a background potential, in which a single particle is moving. This will lead to a description of the acceleration process and the so called separatrix [Esarey et al. 1996].

The Hamiltonian of a free particle in normalized units (for electrons: $q = -1$) is given by:

$$H = \sqrt{1 + (\boldsymbol{P} - q\boldsymbol{A})^2} + q\varphi(z,t) \tag{3.38}$$

Instead of transforming $\varphi(\zeta)$ back to $\varphi(z,t)$, H will be transformed to the co-moving co-ordinates: $H(x,y,z,P_x,P_y,P_z,t) \rightarrow K(x,y,\zeta,P_x,P_y,P_\zeta,t)$. According to Kuypers 2005, the new coordinates can be obtained by

$$\zeta = \frac{\partial F_2}{\partial P_\zeta} = z - \beta_p t \qquad\qquad P_\zeta = \frac{\partial F_2}{\partial z} = P_z \tag{3.39}$$

with the generating function of the transformation $F_2(z, P_\zeta, t) = (z - \beta_p t)P_\zeta$.

The new Hamiltonian[2] K reads:

$$K = H + \frac{\partial F_2}{\partial t} \tag{3.40}$$

$$= H - \beta_p P_z \tag{3.41}$$

$$\boxed{K = \sqrt{1 + (\boldsymbol{P} - q\boldsymbol{A})^2} + q\varphi(\zeta) - \beta_p P_z} \tag{3.42}$$

For the 1D problem discussed here, K simplifies to $K(\zeta, P_y, P_z, t)$. However, as seen in equation 2.13 P_y is a conserved quantity and its value is determined by the initial conditions. As before, the quasi-static approximation can be used in the co-moving

---

[2]Strictly, the Hamiltonian must depend on the canonical variables and time. Therefore P_z would need to be replaced by P_ζ. Since both variables denote identical values, P_z will still be used for convenience.
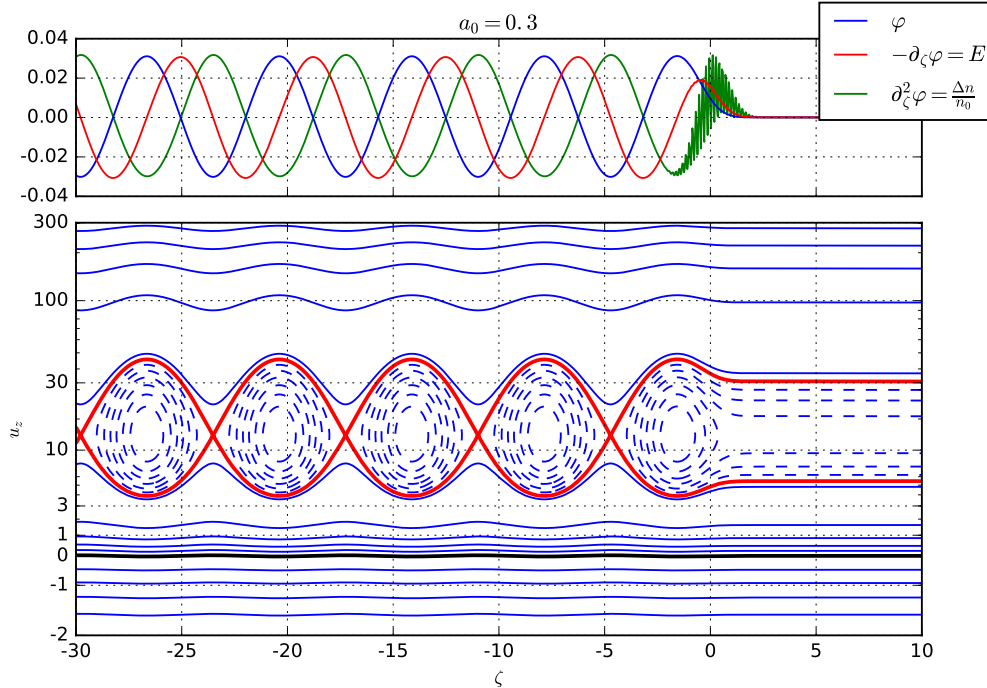
Figure 3.2: *The numerical solution of the potential $\varphi(\zeta)$ (top) and phase space trajectories of particles moving in that potential (bottom). Two trajectories are emphasized: Particles initially at rest (black) and the separatrix (red), which is defined as the transition between open and closed trajectories. Electrons following an open trajectory will oscillate due to the wave passing by, while electrons following closed trajectories are trapped inside one wave period.*

coordinates and K becomes time independent ($K \neq K(t)$). A time independent Hamiltonian must be a conserved quantity[3] and the value of K is conserved along electrons trajectories. Consequently all particle trajectories are identical to contour lines of the function $K(\zeta, P_z)$. They are plotted in figure 3.2 for $a_0 = 0.3$ and $k_p = 1$: The upper panel shows the numerical solution $\varphi(\zeta)$ and its derivatives. The lower panel shows contour lines of the function $K(\zeta, P_z = u_z)$. Electrons, which have initially (at $\zeta \to \infty$) no transverse momentum will therefore follow one of the trajectories in phase space denoted by the contour lines in this plot. The actual trajectory is determined by the initial position of the particles in phase space (ζ, u_z). Figure 3.3 shows the same scenario for $a_0 = 1$ and $a_0 = 3$.

The phase space trajectories of two special cases are marked with different colors:

Particles initially at rest The black line indicates the phase space trajectory of particles which are initially at rest. All particles of the plasma background – which actually create this potential – are following that line. This contour line is defined by $K = 0$.

---

[3] For $H = H(q, p, t)$ it follows: $\dfrac{dH}{dt} = \dfrac{\partial H}{\partial q}\dot{q} + \dfrac{\partial H}{\partial p}\dot{p} + \dfrac{\partial H}{\partial t} = -\dot{p}\dot{q} + \dot{q}\dot{p} + \dfrac{\partial H}{\partial t} = \dfrac{\partial H}{\partial t}$

Separatrix The separatrix is defined as the transition between the open and the closed trajectories in phase space (red line). The open trajectories are followed by electrons which oscillate in the plasma wave. This can be seen, for example, for the blue lines solid lines: electrons which are initially at rest are moving slightly due to the plasma wave leading to the density modulations depicted as the green line in the upper panel. The closed contour lines (dashed, blue) represent electron trajectories which are trapped inside a plasma wave.

3.2.2 Injection into a plasma wave

Electrons on trapped trajectories (i. e. inside the separatrix) can be accelerated in the plasma wave. Unfortunately, the plasma electrons follow the black line in figure 3.2, which is clearly separated from the trapped trajectories. In order to make LWFA possible, some of the electrons need to make the transition from an open (solid blue line) to a closed (dashed blue line) trajectory, thus they need to cross the separatrix. This transition is called *injection* or *trapping*.

By comparing figures 3.2 and 3.3 it can be observed that the separatrix and the plasma electrons move closer together as the wave amplitude increases. Consequently, the plasma electrons need to overcome a smaller potential difference for injection at a larger a_0 or a reduced phase velocity of the plasma wave [Schroeder et al. 2006]. This suggests that a large plasma wave amplitude increases the chance of electron injection into the plasma wave. However, there is no injection within this 1D model. Due to the 1D fluid description, the electrons have a single, well defined momentum P_z for every position ζ. Consequently electron trajectories cannot split in phase space (i. e. a fraction of the electrons becomes trapped, while the majority keeps forming the plasma wave) and no electrons can be accelerated within this model.

In reality, there are various ways for particles to become trapped and accelerated in the plasma wave structure. Different mechanism of injection will be discussed in the next section.
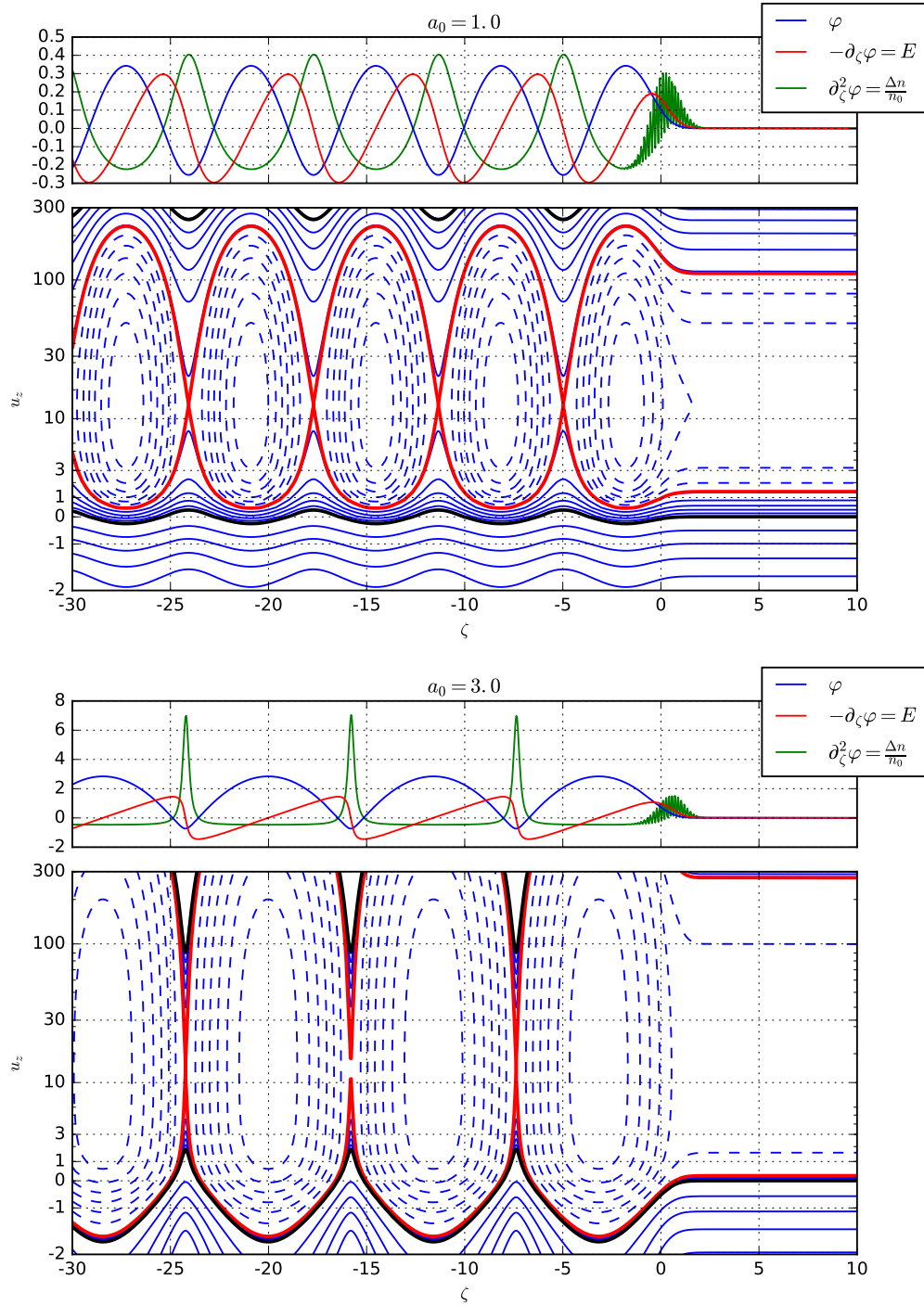
Figure 3.3: *Same as figure 3.2, but $a_0 = 1$ and $a_0 = 3$ are shown. It can be seen, that the black line (initial rest electrons) and the separatrix (red) are moving closer to each other as a_0 increases and the potential difference between electrons initially at rest and the separatrix decreases.*

3.2.3 Mechanisms of injection – beyond the 1D fluid model

The 1D fluid model cannot describe the injection process of electrons into the plasma wake. PIC simulations (section 2.2) do not rely on a fluid description and therefore include the injection process in the simulation. They are often used to numerically model these interactions for high intensities.

The injection process is in many ways important for the accelerated electrons: First, the time of injection determines how long the electrons are accelerated within the plasma wake and therefore it determines their final energy. In addition the injection mechanism determines what volume in phase space the injected electrons occupy, which manifests itself in the electron's emittance as well as their divergence after the acceleration. Consequently, controlling the injection means controlling electron energy, emittance and divergence [Esarey et al. 2009].

Wave breaking

As seen in figure 3.3, the phase space trajectory of the electrons initially at rest (background plasma) shows that increasing a_0 also increases the maximum forward momentum u_z they gain within the plasma wake. If a_0 increases even further, the maximum forward velocity of the electrons will at some point exceed the phase velocity of the plasma wave β_p. This is called wave breaking and as a result of it, electrons will become trapped in the plasma wake, as schematically shown for the 2D PIC simulation in figure 3.4, lowest panel. As in the 1D model, a larger a_0 also increases the amplitude of the plasma wave until wave-breaking occurs. Please note that these presented simulations show the principle of injection. The a_0 needed to induce wave-breaking in the 2D simulation cannot be compared to an experiment to an experiment.

Two requirements have to be met in order for wave breaking to occur (see figure 3.5 for a schematic illustration of the relations): First, the electrons need to gain enough initial momentum in order to overcome the phase velocity of the wake. This initial momentum is delivered by the amplitude of the plasma wake (section 3.2). Since the wake is driven by a laser pulse (in this example), it depends on the a_0 of the laser pulse as well as the temporal and spatial pulse shape.

Secondly, a slower phase velocity of the plasma wake β_p is favorable for wave-breaking [Bulanov et al. 1998; Suk et al. 2001]. The smaller β_p, the less wake amplitude is required to provide the momentum needed to accelerate the electrons to at least β_p and allow them to enter the accelerating phase of the plasma wave. The phase velocity of the wake β_p
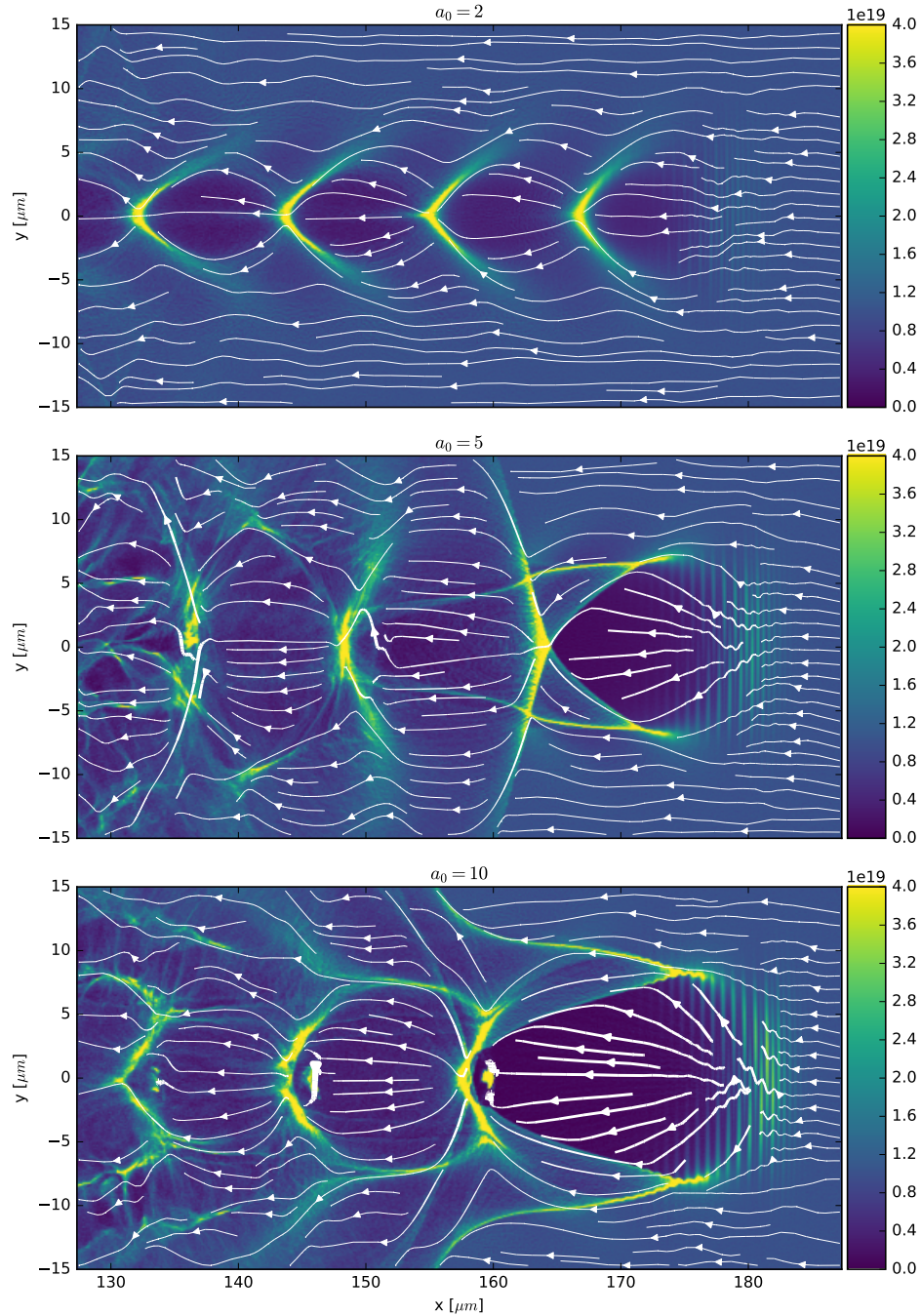
Figure 3.4: *2D PIC simulations of the plasma wake behind the laser pulse for different laser intensities corresponding to different a_0: The color scale indicates the plasma density in $\frac{1}{\text{cm}^3}$. The streamlines show the movement of the electrons in the co-moving system.*

At $a_0 = 2$ (top), the plasma wake shows the anharmonic oscillation with periodic density spikes. With increasing a_0, the period length increases until wave breaking occurs $a_0 = 10$ (bottom). The wave breaking itself is not visible, but as a result of wave breaking trapped electrons are visible in the first and the second bucket. Snapshots of the wave-breaking process are shown in figure A.1.

A video version is available at `https://youtu.be/--xjEIQe-zE`
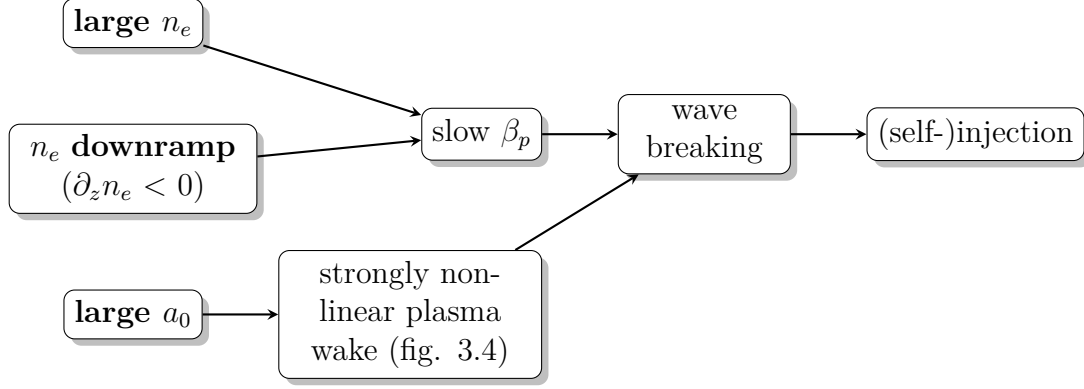
Figure 3.5: *Schematic diagram to illustrate how different conditions (bold) affect the plasma wake and finally lead to electron injection triggered by wave breaking. It is important to note, that wave-breaking needs a plasma wake strong enough in combination with a reduced phase velocity of the plasma wake β_p to occur.*

can be reduced from the speed of light due to various reasons. Important contributions to β_p are listed here:

$$\beta_p = 1 - \underbrace{\frac{1}{2}\frac{\omega_p^2}{\omega^2}}_{\text{dispersion}} - \underbrace{\frac{\omega_p^2}{\omega^2}}_{\text{etching}} - \underbrace{\frac{\zeta}{\lambda_p}\frac{\partial \lambda_p}{\partial z}}_{\text{density downramp}} \qquad (3.43)$$

The plasma dispersion term has been derived already in section 2.1.1. Etching (section 3.2.4) and density down-ramp (equation 3.46) will be discussed in the following.

In the literature, the first two terms are often summed up to $\frac{3}{2}\frac{\omega_p^2}{\omega^2}$ [Lu et al. 2007]. They depend only on the plasma density. When they are the leading contribution to β_p, the injection process is often called *self-injection*, neglecting the downramp term. In case of artificially induced plasma density down-ramps, the downramp term dominates and the process is typically called *down-ramp injection*, while neglecting the other two terms. However, it is important to note, that all of these contributions lead to the exact same injection mechanism, namely wave breaking.

The quantitative measurement of the downramp term with a resolution of $10\,\mu$m has been realized in this thesis for the first time (Chapter 4). As it was not measured before, its influence in the context of small scale random density variations has not been fully appreciated.

phase velocity of the plasma wave in a density gradient

The decrease of the phase velocity of the plasma wake in a density downramp can be explained as follows: In case of a low amplitude wake, the plasma wavelength is solely determined by the plasma density $\lambda_p \sim \frac{1}{\sqrt{n_p}}$. A longitudinal plasma density gradient (decreasing n_p with increasing x) therefore leads to a continuously increasing plasma wavelength over the propagation. Accordingly, the expansion of each wave period, slow down the phase front of each following wave period. Consequently, the phase fronts of the plasma wake propagate with a decreased velocity v_p. The slow-down reduces β_p, which can trigger wave breaking if the gradient is large enough [Bulanov et al. 1998]. Likewise electrons would need to overcome a smaller momentum gap in order to reach v_p and become trapped inside the plasma wake.

The reduction of β_p can be understood by considering a step-like density transition. Before the transition, the plasma wavelength is given by λ_{p1} and afterwards it is given by λ_{p2}. Before the density transition, the Nth plasma oscillation is located at $N\lambda_{p1}$ relative to the driving laser pulse. During the passage of the plasma wave through the transition, the Nth plasma oscillation changes its location by $\Delta\zeta = N(\lambda_{p1} - \lambda_{p2})$. Therefore the change of phase velocity is proportional to the distance ζ behind the driving laser pulse and the change of the wavelength. In a continuous density gradient, the phase velocity of the plasma wake is reduced to [Esarey et al. 2009]:

$$\beta_p = \frac{1}{1 + \frac{\zeta}{k_p}\frac{\mathrm{d}k_p}{\mathrm{d}z}} \tag{3.44}$$

which can by approximated if $\Delta\lambda_p \ll \lambda_p$

$$\beta_p \approx 1 + \frac{\zeta}{2n}\frac{\partial n}{\partial z} \tag{3.45}$$

and simplified substituting $n = \omega_p^2 \frac{m\varepsilon_0}{e^2}$ and $\omega_p = \frac{2\pi c}{\lambda_p}$

$$\beta_p = 1 - \frac{\zeta}{\lambda_p}\frac{\partial\lambda_p}{\partial z}. \tag{3.46}$$

In other words, a fast enough increase of the plasma wavelength induces wave breaking and therefore injection. Downramp injection [Geddes et al. 2008] has been used for triggering injection continuously [Gonsalves et al. 2011] or abrupt by a density transition through a shock front [Buck et al. 2013; Schmid et al. 2010].

When considering electron injection into the first wave period, β_p has to be evaluated at the end of the first plasma wave. Neglecting the nonlinear increase of the plasma

wavelength (valid for low wave amplitudes), this is at the position $\zeta = \lambda_p$. Using $\lambda_p = \frac{2\pi c\sqrt{m_e\varepsilon_0}}{q_e} n_p^{-1/2}$, the downramp term can be written as

$$\beta_p = 1 - \frac{\partial\lambda_p}{\partial z} = 1 + \frac{\pi c\sqrt{m\varepsilon_0}}{q_e} n_p^{-3/2} \frac{\partial n_p}{\partial z} = 1 + \frac{\lambda_p}{2n_p}\frac{\partial n_p}{\partial z}. \tag{3.47}$$

Please note the $n_p^{-3/2}$ scaling, which becomes important when the density of the acceleration is reduced. This will be discussed in section 4.7.

Self-injection

Self-injection is not a well defined mechanism in the literature. The term is typically used to emphasize, that electrons were injected and accelerated while there was no distinct position for injection to happen. Self-injection can be typically attributed to injection by wave-breaking. As illustrated in figure 3.5, different conditions of the plasma (density downramp or large density) decrease the phase velocity of the plasma wake β_p. Additionally a large a_0 of the driving laser pulse leads to a stronger plasma wake. Both effects together are required for wave-breaking.

Ionization Injection

Ionization injection (e. g. [Chen et al. 2012]) is based on the fact that different charge states of an atom are ionized at different electric field strengths. The ionization process is complicated in detail, however there are established models to calculate approximate ionization rates, such as the Ammosov-Delone-Krainov (ADK) model [Ammosov et al. 1987; Ammosov et al. 1986]. Table 3.1 lists the ionization potentials of hydrogen, helium and nitrogen as well as the intensities which cause an ionization rate of 0.5/fs at $\lambda = 800$ nm. Hydrogen or helium already ionize before $a_0 \sim 0.03$, which is reached already in the rising edge of the main pulse. The same holds true for all nitrogen levels up to the fifth level. However, the ionization potentials of level 6 and 7 are considerably larger and consequently a higher intensity is required for ionization ($a_0 = 1.8$ or $a_0 = 2.3$). Once the laser has reached this intensity it will also drive a considerable plasma wake. The electrons being released by the ionization process will therefore start at a point in phase space which is not on the fluid trajectory and possibly inside the separatrix as illustrated in figure 3.6. It is important to note, that ionization injection does not require the plasma wave to break. Instead the released electrons ideally start their trajectories already inside the separatrix.
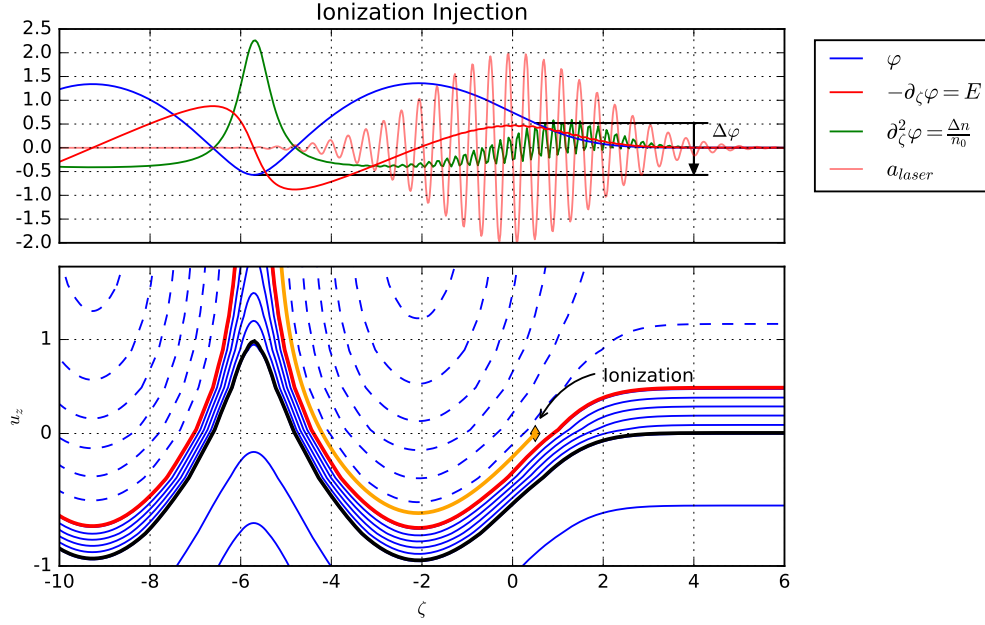
Figure 3.6: *The principle of ionization injection: The laser pulse is propagating from left to right and ionization injection can happen in its rising edge. The front of the laser pulse already creates a plasma wave such that the separatrix (red line lower panel) crosses $u_z = 0$ during the rising edge of the pulse. An electron, which is released due to ionization, after the seperatrix has crossed $u_u = 0$, is consequently released inside the separatrix and will be accelerated. As an example, the point of ionization is marked by an amber diamond and the following particles trajectory by the amber line.*
In another perspective, the electron is starting its trajectory with zero velocity ($u_z = 0$ after ionization) but at a different wake potential. The total potential difference due to the wake field $\Delta \varphi$ is sufficient for it to reach the phase velocity of the wake v_p at the end of the first plasma wake period.

The electrons which are released close to the maximum of the laser pulse undergo a larger potential difference $\Delta \varphi$ (figure 3.6) than the electrons which are ionized well before the main pulse. Due to the large potential difference, they gain more momentum within the wake, allowing them to keep up with the plasma wake to become accelerated.

Ionization injection has been experimentally demonstrated [Pak et al. 2010; Ralph et al. 2010]. Section 4.4 will show that the use of ionization injection will also affect beam quality and pointing stability.

Atom	Level	IP (eV)	$I\ (\frac{\mathrm{W}}{\mathrm{cm}^3})$	a_0
H	1	13.6	$2.2 \cdot 10^{14}$	0.01
He	1	24.6	$1.7 \cdot 10^{15}$	0.03
	2	54.4	$1.0 \cdot 10^{16}$	0.07
N	1	14.5	$2.8 \cdot 10^{14}$	0.01
	2	29.6	$1.2 \cdot 10^{15}$	0.02
	3	47.5	$3.3 \cdot 10^{15}$	0.04
	4	77.5	$1.2 \cdot 10^{16}$	0.08
	5	97.9	$2.0 \cdot 10^{16}$	0.1
	6	552	$1.8 \cdot 10^{18}$	1.8
	7	667	$2.3 \cdot 10^{18}$	2.3

Table 3.1: *The ionization potentials (IP) of hydrogen, helium and nitrogen. The last two columns present the intensity and the corresponding a_0 which cause an ionization rate of 0.5/fs as predicted by the ADK model with $\lambda = 800$ nm. The nitrogen levels 6 and 7 are used for ionization injection because of the much higher intensity required for ionization.*

Further methods of injection

Wave breaking and ionization injection are widely used in current LWFA experiments because of their simplicity. However various further methods have been invented to move electrons into the separatrix phase space. Selected injection methods should be outlined briefly.

- The ponderomotive injection is an example of two colliding laser pulses. The injection pulse is propagating perpendicular to the driving laser pulse [Umstadter et al. 1996]. Some electrons gain energy due to the ponderomotive force of the injection pulse which leads to injection into the plasma wake of the driving pulse.

- In contrast, the colliding pulse injection [Esarey et al. 1997] is the co-linear collision of two pulses with slightly detuned frequencies. This excites a beat wave with a phase velocity of $\frac{\Delta\omega}{2k_0} \ll c$. This slow moving wave is used as a pre-acceleration stage for the electrons before being accelerated in the plasma wake.

- External injection means that another accelerator (typically conventional) is used to accelerate an electron bunch to energies such that it can keep up with the plasma wave. This is experimentally extremely challenging because the conventional accelerator and the laser pulse need to be synchronized on a femtosecond time scale. A project combining conventional with plasma based accelerators is for example the SINBAD accelerator at DESY in Hamburg, Germany [Grebenyuk et al. 2014].

3.2.4 Relativistic laser pulse evolution in underdense plasmas

The laser pulse is affected by the plasma. The dispersion relation of light propagating through a plasma was already derived in section 2.1.1 for the non-relativistic case. The laser pulse is further altered by relativistic effects within the plasma, as discussed in the following.

Relativistic self-guiding and self phase modulation

The non-relativistic motion of the electron in the electro-magnetic wave leads to dispersion of the wave as described in section 2.1.1. Dispersion is only depending on the plasma frequency ω_p and the laser frequency ω. If the intensity of the EM-wave increases to relativistic intensity, the relativistic mass increase of the moving electrons effectively reduces the plasma frequency $\omega_p = \omega_{p0}/\sqrt{\gamma}$ [Sun et al. 1987; Umstadter 2003]. Since the plasma frequency is changed in regions of high intensity, also the refractive index is changes. A Taylor expansion for $a_0 \ll 1$ is [Esarey et al. 2009]:

$$\eta = 1 - \frac{\omega_{p0}^2}{2\omega^2}\left(1 - \frac{a^2}{2}\right) \tag{3.48}$$

The refractive index is increased in regions of high intensity, which is on axis in case of a Gaussian beam profile. Therefore the phase velocity $v_\phi = c/\eta$ is slower on the beam axis compared to the outer regions of the laser beam. Consequently the phase fronts of the laser become curved towards the axis, which results in self-focusing of the laser beam [Esarey et al. 1996]. It is worth noting, that equation 3.48 can be written in the form $\eta = \eta_0 + \eta_2 \cdot I$, which is well known from non-linear optics in crystals [Boyd 2008].

The self-focusing can lead to self-guiding, if the focusing effect is strong enough to balance the diffraction of the laser pulse. This happens if the laser power P exceeds a critical power $P_c \approx 17.4\frac{\omega^2}{\omega_p^2}$ [GW] [Esarey et al. 2009]. The guiding effect has been first shown experimentally by Wagner et al. 1997 over a distance of $\sim$10 Rayleigh ranges. A LWFA experiment using self-guiding and ionization-injection is, for example, published by Clayton et al. 2010.

Etching

The laser pulse driving the plasma wake constantly delivers energy to the wake. Since the front of the laser pulse drives the plasma wake the pulse looses energy faster on its front than on its tail. The laser pulse gets slowly eroded away from its front. This effect is called *etching*. Note that the etching velocity $v_{\text{etch}} = c\frac{\omega_p^2}{\omega^2}$ can be calculated from

the 1D model (section 3.1) [Decker et al. 1996]. The etching actually reduces the phase velocity of the plasma wake β_p, which then becomes

$$\beta_p = \beta_g - \beta_{\text{etch}} \tag{3.49}$$

$$= 1 - \frac{3}{2}\frac{\omega_p^2}{\omega^2} \tag{3.50}$$

with β_p from equation 2.32. In conclusion plasma dispersion and etching reduce the group velocity of the laser and therefore the phase velocity of the plasma wake. The electron acceleration terminates if the laser pulse has lost all its energy into the plasma wake, which is reached after the so called *pump-depletion length* L_{pd}

$$L_{pd} = c\frac{\omega_p^2}{\omega^2}\tau \tag{3.51}$$

where τ is the duration of the laser pulse (FWHM) [Lu et al. 2007].

3.2.5 Scalings and limitations of LWFA

For 3D studies of LWFA, the so called *bubble* or *blow-out* regime [Kostyukov et al. 2004; Rosenzweig et al. 1991] is introduced. It assumes that the laser is strong enough to expel all plasma electrons from the laser axis, leaving only the ions behind. The plasma wake is therefore assumed to be an electron-free region of spherical shape with radius R. This model applies quite well for $a_0 > 4$ and also for $a_0 \gtrsim 2$ for matched laser spot conditions (Lu et al. 2006, equation 3.53).

In order to achieve a long acceleration length (several or several tens of Rayleigh ranges) the laser pulse needs to be guided by the plasma (last section). Conditions for efficient laser guiding (no beam oscillations) can be estimated assuming that the ponderomotive force is balanced by the radial electric field of the plasma wake. The plasma wake is assumed to be a spherical region (radius R) behind the driving laser pulse. Equating $F_{\text{pond}} = \frac{a_0}{k_p R}$ with $F_{\text{electric}} = k_p R$ yields [Lu et al. 2007]:

$$k_p R = \sqrt{a_0} \tag{3.52}$$

Lu et al. 2007 present, that $k_p R = 2\sqrt{a_0}$ (note the additional factor two) matches PIC simulation results much better. Additionally it is assumed, that the laser spot size w_0 should roughly match the blow out radius R. In total, this yields the matching conditions

for optimal laser guiding:

$$\boxed{k_p R \sim k_p w_0 \sim 2\sqrt{a_0}}$$

(3.53)

One of the leading limitations of LWFA is called *dephasing*. The phase velocity of the plasma wake β_p is reduced by etching and dispersion in a constant density plasma (equation 3.43). Consequently accelerated electrons can move faster than the plasma wake and will finally outrun the accelerating phase of the plasma wake. The distance after that *dephasing* happens is called dephasing length L_d [Lu et al. 2007] and is given by

$$L_d = \frac{c}{c - v_p} R \approx \frac{2}{3} \frac{\omega^2}{\omega_p^2} R$$

(3.54)

The acceleration terminates after reaching the dephasing length. Within the separatrix model, the dephasing length would be the distance the electrons travel in the lab frame before obtaining their maximum momentum u_z (figure 3.3).

Pump depletion and dephasing limit the acceleration process. Short laser pulses will deplete before the electrons dephase. Too long pulses will reach farther into the plasma wake and the electrons will also be accelerated within the laser field. In this scenario the electrons will acquire large transverse momenta, which leads to a large divergence and is typically unwanted for the electron beam. Therefore the laser pulse should be as short as possible, but the acceleration process should still be limited by the dephasing length L_d rather than the pump depletion length L_{pd}

$$L_{pd} > L_d$$

(3.55)

$$c\tau > \frac{2}{3} R$$

(3.56)

The maximum electric field within the blow out region or "bubble", that can be used for acceleration can be calculated as $E_{\max}/E_0 = \sqrt{a_0}$, with $E_0 = cm_e\omega_p/e$ [Lu et al. 2007]. The maximum energy gain of the electrons can be estimated by assuming a constant accelerating electric field ($\sim \sqrt{a_0}/2$) over the dephasing length L_d. This leads to to a scaling law for the electron energy gain in a laser plasma accelerator [Lu et al. 2007]:

$$\Delta E \approx \frac{2}{3} mc^2 \frac{\omega_0^2}{\omega_p^2} a_0$$

(3.57)

$$\Delta E [\,\mathrm{GeV}] \approx 1.7 \left(\frac{P[\,\mathrm{TW}]}{100} \right)^{1/3} \cdot \left(\frac{10^{18}}{n_p[\,\mathrm{cm}^{-3}]} \right)^{2/3} \cdot \left(\frac{0.8}{\lambda_0[\,\mu\mathrm{m}]} \right)^{4/3}$$

(3.58)

with the peak power of the laser system P, plasma density n_p and central wavelength λ_0. This scaling has been experimentally confirmed on various laser systems as long as the matching conditions (equation 3.53) were fulfilled and the pulse is not limited by pump depletion. In order to obtain maximum electron energies, the plasma density n_p has do be reduced, which increases the plasma wavelength. Therefore the blow out radius R increases and the laser spot size w_0 needs to be increased as well. This is why LWFA experiments use a long focal length typically larger than f/10. However, an increased w_0 also requires more laser power to maintain the a_0 at the focus. This is the reason for the unfavorable $P^{1/3}$ scaling of the maximum electron energy.

4 A background-free acceleration regime accessed by the gas cell

Laser wake field accelerators (LWFA) stand out for their extremely large accelerating fields, the plasma can sustain. Therefore it is an active topic of research and the maximum electron energy is constantly increasing. The pointing stability, beam quality and control over the spectral shape, however, still need to improve to be able to use those beams for secondary experiments such as QED experiments or a free electron laser. The ability to control the injection and acceleration mechanism independently is the key to match the accelerator to the demands of the experiment or any specific usage of the accelerated electron beam.

Self-injection or wave breaking relies on a strong plasma wake and also on the reduction of the phase velocity of the wake β_p (section 3.2.3). This depends on the plasma density and on plasma density gradients, as presented in the last chapter. Now, localized density modulations are measured inside a gas jet and could be quantified using transverse probing images of the plasma wake. As other methods for density measurements, such as Abel inversion of the accumulated phase, usually average over a large volume, they are oblivious to density modulations on such a small scale. The quantification of the small scale density gradients will show for the first time, that these density modulations are the leading contribution to β_p in the gas jet, but below resolution in the newly developed gas cell (equation 3.43). It is possible to drive a considerable plasma wake for the acceleration in the gas cell, while suppressing self-injection. Using ionization injection, the pointing stability and beam shape improve strongly (section 4.6).

4.1 Gas targets for LWFA

Over the last two decades various gas targets have been built for the use in laser wake field acceleration (LWFA). The simplest and most basic target is the gas jet. Its simplicity makes it easy to use and therefore many experiments all over the globe have been conducted using a gas jet. The density of the gas – and therefore the plasma density after

ionization – can be varied by varying the backing pressure, the shape of the gas profile can be controlled with the shape of the nozzle. Generally supersonic nozzles allow the creation of steep gradients at the front and the back while having an almost constant density plateau over a mm long region [Semushin et al. 2001; Azambuja et al. 1999]. Nozzle designs were optimized to flatten the density plateau [Lemos et al. 2009].

On the JETI 40 laser system, the gas jet has been used for years for LWFA and much effort has been made to characterize the gas profiles by combining transverse probing and tomographic reconstruction [Landgraf et al. 2011]. In this thesis, a gas cell has been developed. Gas cells have already been used on other facilities [Pollock et al. 2011; Audet et al. 2016; Osterhoff et al. 2008] and even 3D printed models have been proposed [Vargas et al. 2014]. However, either the size, durability or probing requirements made it impossible to adopt those gas cells to a comparably small laser system: The typical acceleration length on the Astra Gemini Laser (Rutherford Appleton Laboratory, UK) is 20 mm to 25 mm, which requires a density plateau of similar length. Using the JETI 40 laser system it is possible to reach acceleration lengths of only 2 mm before dephasing or depletion limit the acceleration process (section 3.2.5). Also the plasma density inside the cell should be well controlled. The gas cell was designed with the following criteria:

Durability Replacing parts of the target during an experiment is time consuming because it requires the vacuum to be broken, which is followed by a realignment procedure. Therefore the number of laser shots onto the gas cell should be maximized by building the cells entry and exit holes of steel. Steel will erode more slowly due to exposure to laser light or plasma contact compared to aluminum or even plastic.

Variable length The length of the gas cell should be variable between 0 mm and 5 to 10 mm without having the cell to be changed. This allows to change the length without or with only minor realignment.

Homogeneous density profile Most importantly the density profile within the cell should be as homogeneous as possible. Therefore the incoming gas stream needs to be subdivided to allow the gas to distribute uniformly as rapidly as possible. The data presented in the next chapter will show, that the homogeneous density is the requirement allowing for stable and dark current free acceleration.

Transverse probing Side windows need to be installed to allow transverse probing. In addition these windows should be large enough to support the numerical aperture of the microscope objective used to image the plasma wave.

An image of the gas jet and the gas cell targets with identical plasma length of 2 mm are shown in figure 4.1. Two plugs (figure 4.1c) are inserted on the front and the back
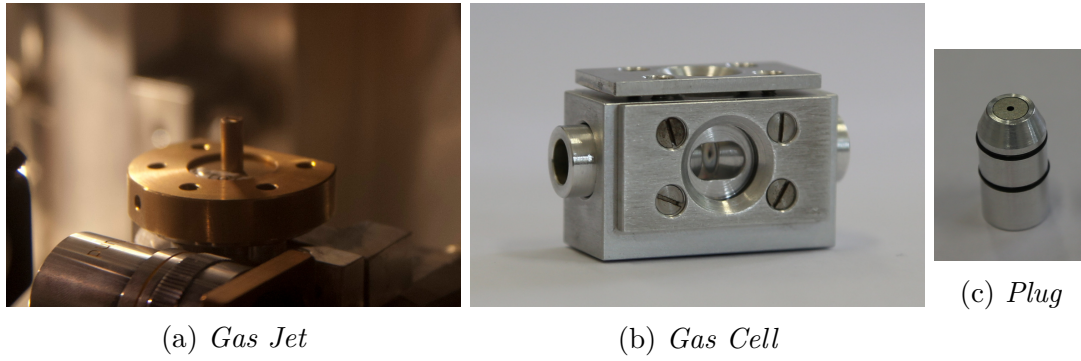
(a) *Gas Jet*

(b) *Gas Cell*

(c) *Plug*

Figure 4.1: *Images of the different gas targets used in the experiments: The supersonic gas jet (left) and the newly developed gas cell (middle). The actual plasma length is set to 2 mm in both cases. The right picture shows one of the two plugs used as the enter or exit holes of the gas cell.*

of the cell and fixed in their position by a set screw. This allows continuous adjustment of the length between the enter and the exit hole of the cell.

4.2 The JETI 40 lasersystem

The experimental results presented throughout the thesis are obtained at the Jena Titanium Sapphire laser system (JETI 40). It is a 40 TW class laser system delivering pulses of $\tau = 27$ fs with an energy of $E = 650$ mJ on target. An overview of the system's key parameters is listed in table 4.1.

The oscillator creates pulses with a repetition rate of 80 Mhz. After the first amplifier single pluses are picked to reduce the repetition rate to 10 Hz. Those pulses are being stretched to 800 ps and further amplified using in total one regenerative amplifier and three multipass amplifiers. The beam diameter is subsequently increased to finally 55 mm before the compressor, which compresses the pulse to 27 fs as measured by a Fastlite WIZZLER. Additionally a Fastlite DAZZLER and a MAZZLER are build into the system to control spectral phase and spectral shape of the pulse. Finally about 650 mJ of energy reach the target chamber.

Energy before compression	$\approx 1.1\,\mathrm{J}$
Energy on target	$E = 650\,\mathrm{mJ}$
pulse duration	$\tau = 28\,\mathrm{fs}$
repetition rate	$10\,\mathrm{Hz}$
peak power (nominal / on target)	$40\,\mathrm{TW}\ /\ 24\,\mathrm{TW}$
central wavelength	$\lambda_0 = 800\,\mathrm{nm}$
spectral width	$\Delta\lambda \approx 70\,\mathrm{nm}$
beam diameter	$55\,\mathrm{mm}$

Table 4.1: *Parameters of the JETI 40 laser system.*

4.3 Experimental setup

The setup of the experiment is depicted in figure 4.2. The laser pulse is reflected by three mirrors inside the octagonal target chamber and finally focused by an f/12 ($f = 65\,\mathrm{cm}$[1]) off-axis parabolic mirror (OAP) onto the target. The target can be either the gas jet or the gas cell in order to compare their performance.

The rising edge of the main laser pulse ionizes the gas atoms and the main pulse can drive a plasma wake within this plasma. Electrons can be injected (section 3.2.3) and accelerated within this plasma wave. The accelerated electrons propagate to a scintillation screen (Kodak Biomax MS) and the scintillation signal is detected by a CCD. This diagnostic will therefore record the beam profile in order to obtain divergence and pointing stability of the accelerated electrons (section 4.4). The charge of the electron beam was deduced using the calibration values reported in Buck et al. 2010 for the Biomax MS screen. The absolute error of the charge measurement is estimated as a factor 2, due to uncertainties in the measurement of the absolute photon flux and the age of the screen.

Additionally a dedicated 6 fs pulse is used to probe the plasma transversely. The accumulated phase difference can be used to determine the plasma density using an Abel inversion [Malka et al. 2000] or imaging the interaction region allows to acquire pictures of the plasma wake driven by the laser [Schwab et al. 2013; Sävert et al. 2015]. The plasma wake images allow to measure the periodicity of the plasma wake and therefore provide a local density measurement, which can be used to identify density modulations within the gas jet (see section 4.4).

The laser focus was imaged by a microscope objective (not shown in drawing) onto a CCD. After optimization of the focal spot, the final spot area was mea-

---
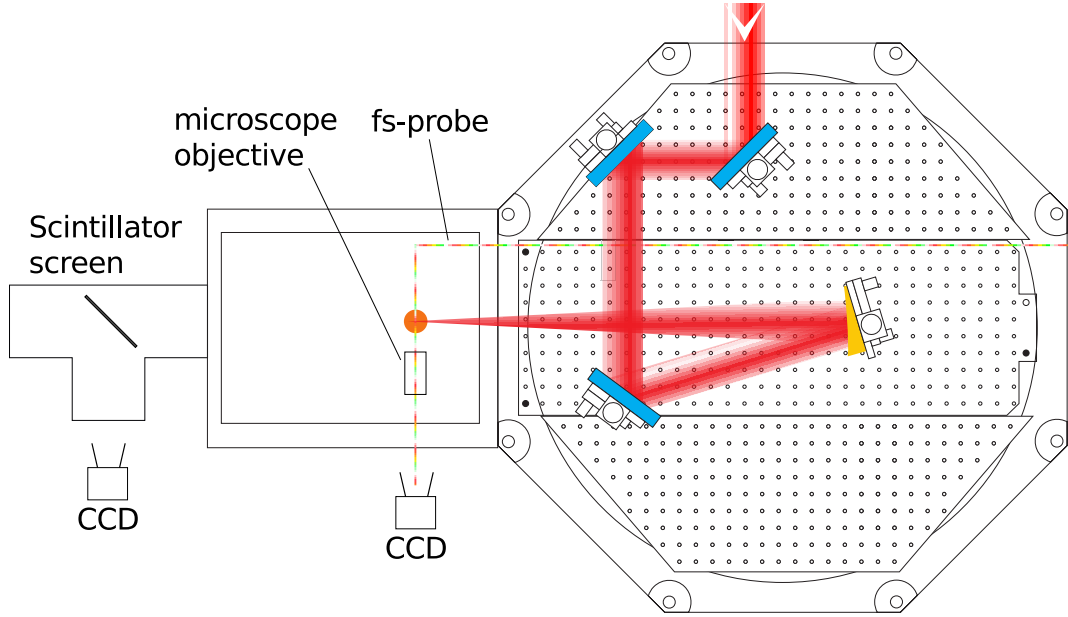
[1]Manufacturer: SORL, OAP25-055-04Q

Figure 4.2: *The experimental setup used to compare gas jet and gas cell: After the JETI 40 pulse enters the 8-sided chamber, it passes over three mirrors until it is finally focused by an f/12 off-axis parabolic mirror onto the gas provided by either the gas cell or the gas jet. The electrons are accelerated in forward direction and their profile becomes visible when passing the scintillating screen. The screen is imaged onto a CCD for detection of the beam profile.*
Additionally an optically coupled 6 fs probe beam passes the target and is imaged by the microscope objective onto another CCD. This allows to image the plasma wave.

sured to $120\,\mu\mathrm{m}^2$, leading to a vacuum peak normalized amplitude of $a_0 = \sqrt{\lambda^2/[\mu\mathrm{m}^2] \cdot I/(1.37 \cdot 10^{18}\,[\mathrm{W/cm}^2])} \approx 2.2$.

The matching conditions (equation 3.53) require $k_p w_0 \approx 2\sqrt{a_0}$ for optimal laser guiding in the plasma. For a plasma density $n_p = 1 \cdot 10^{19}\,/\mathrm{cm}^3$, as used in the experiment, and the presented laser and focusing parameters, these conditions are almost fulfilled: $k_p w_0 = 3.6 \approx 2\sqrt{a_0} = 3$. The difference may be explained by self-compression of the laser pulse inside the plasma, resulting in an increased a_0. A corresponding non-linear increase of the plasma wavelength has been experimentally observed using the same laser system [Sävert et al. 2015].

The gas target (jet or cell) is mounted on a xyz-translation stage to align the target relative to the laser focal spot position. The length of the gas jet and gas cell was adjusted to 2 mm. In case of the gas jet the laser focal spot was aligned 0.75 mm above the nozzle. For the gas cell it was aligned to the middle of the 0.8 mm diameter entrance aperture. The longitudinal position of the focus as well as the second order dispersion were optimized in each case for the stability of the electron beam.

4.4 Density modulations inside the gas jet

A good comparison between the gas cell and the gas jet requires identical (or at least closely matched) conditions in both targets. While it is possible to ensure identical density in the constant density section, the targets will differ in the detailed profile as their working principles differ. Before the discussion of the electron acceleration, two major differences between the gas targets will be discussed.

First, the density ramps at the beginning and at the end of the targets are different. The supersonic gas jet has a steep density gradient, typically in the range of $\sim 100\,\mu$m [Landgraf et al. 2011]. For the gas cell, the gas is flowing outwards though the openings and therefore the gas density on axis drops much slower. The scale of this decrease is approximately on the scale of the of the entrance and exit holes [Sazhin 2008], which are 0.8 mm in diameter. The longer ramps of the gas cell affect the LWFA process in two ways.
1. The upramp at the beginning of the gas cell changes the coupling of the laser pulse into the plasma. The smooth transition between vacuum and plasma may increase the coupling into the guiding mode of the plasma [Poder et al. 2017b]. However, the additional plasma in the ramp would also cause an energy loss due to etching and ionization.
2. The downramp at the exit of the gas cell affects the electron beam directly. The density ramp can damp the electron's betatron oscillations and thus lead to a reduced divergence of the electron beam [Shaw et al. 2012].

Secondly, the images of the plasma wake revealed density modulations on a scale of $50\,\mu$m or smaller: Typical plasma wave images, captured by transverse probing are compared for both gas targets (figure 4.3). In both cases, the the plasma wake is clearly visible as well as the curved wave fronts. The first wake period is slightly enlarged due to the non-linear driven plasma wake by the laser. All images show a similar first wake period, indicating similar laser intensity in the plasma of the gas jet and the gas cell. The probing of the gas cell shows a clear plasma wake with constant plasma wavelength. This suggests a very homogeneous density on the laser axis. The probing image of the gas cell, however, shows clear variation of the plasma wavelength. This indicates density modulations inside the gas jet. Please note, that interferometry is averaging the density over a too large spatial region to resolve such localized density modulations.

The influence of the density modulations on the wave breaking behavior can be quantitatively determined using equation 3.43. For the first wake period (bucket) we can approximate $\zeta \approx \lambda_p$ and the derivative $\frac{\partial \lambda_p}{\partial z}$ can be calculated from the plasma wake images, even without knowledge of the magnification factor. For the images shown in
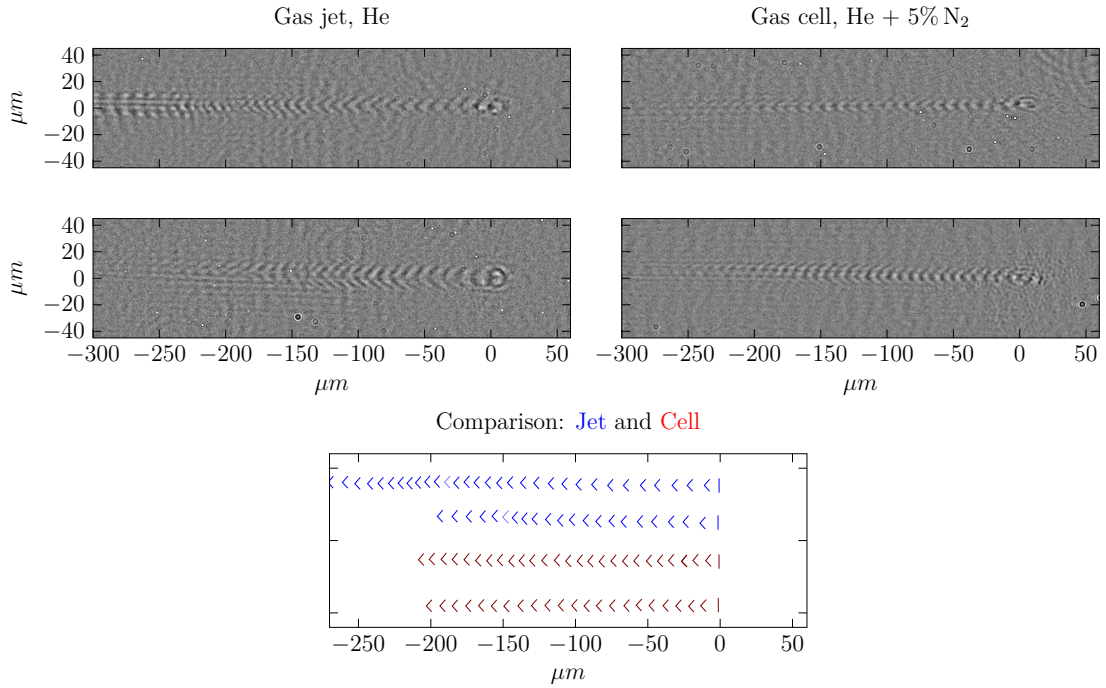
Figure 4.3: *Images of the plasma wave, captured by transverse probing. The first wake field period is clearly visible and enlarged compared to the other wake periods. This is a result of the non-linear driven plasma wake by the laser $(x = 0)$. The laser conditions are therefore similar in the gas cell and the gas jet. For better comparison the phase fronts of the individual wakefields are presented in the lower graph for the jet (upper two, blue) and the cell (lower two, red). The wavelength of the plasma wakefield shows a clear variation over the propagation distance within the gas jet whereas the phase fronts of the plasma wake within the gas cell are equally spaced. The gradient $\frac{\partial \lambda_p}{\partial z}$ from the images evaluates for the gas jet to $\sim 3\%$.*

figure 4.3, the terms evaluate to:

$$\beta_p = 1 - \underbrace{\frac{1}{2}\frac{\omega_p^2}{\omega^2}}_{0.3\%} - \underbrace{\frac{\omega_p^2}{\omega^2}}_{0.6\%} - \underbrace{\frac{\zeta}{\lambda_p}\frac{\partial\lambda_p}{\partial z}}_{\text{1st bucket: } \sim 3\%} \tag{4.1}$$

While etching and dispersion reduce β_p by only 0.9% combined, the down-ramps as present in the gas jet lead to an additional reduction of $\sim 3\%$. Clearly, the small down-ramps are the major contribution to the slow down of the phase velocity of the plasma wake β_p. As they are not present inside the gas cell, a different injection behavior of both gas targets is expected. The small density modulations can act as multiple down-ramps, which the laser pulse passes, while propagating through the gas jet. Due to the additional reduction of β_p in each of the down-ramps, the plasma wake has a highly increased probability to break. That would lead to consecutive injection of electrons in each down-ramp.

4.5 Background-free ionization injection

In this section the electron beams of gas jet and gas cell will be compared. For different target configurations a typical series of six consecutive laser shots is shown in figure 4.4: The beam profiles of the gas jet used with pure He show strong structuring (third row of graphs). There is typically a region of high electron flux on the screen, surrounded by a region with "wings" or "branches" of electrons displaying various shapes. Row number four shows the beam profiles of the gas cell using pure He. In this case no accelerated electrons were observed, even for a larger plasma density of $n_e = 2.4 \cdot 10^{19}$ /cm^3 (note the change of the color scale). This measurement shows, that the self-injection occurring in the gas jet is indeed suppressed in the gas cell.

In order to inject electrons into the plasma wake in the gas cell, a mixture of 95% He and 5% N_2 was used to trigger ionization injection. The corresponding beam profiles are shown in rows one and two (figure 4.4) displaying almost no substructure. Since no self-injection was observed within the gas cell at all accessible densities, all acceler-ated charge must be ionization injected by the ionization of $N^{5+} \rightarrow N^{6+}$ or $N^{6+} \rightarrow N^{7+}$ (section 3.2.3).

For a better comparison, the accelerated charge depending on the plasma density is plotted in figure 4.5. The visible trend is that more charge is accelerated when the plasma density is increased, independent of the gas target used. This can be explained with a slower phase velocity of the plasma wake (β_p) caused by a slower laser pulse propagation

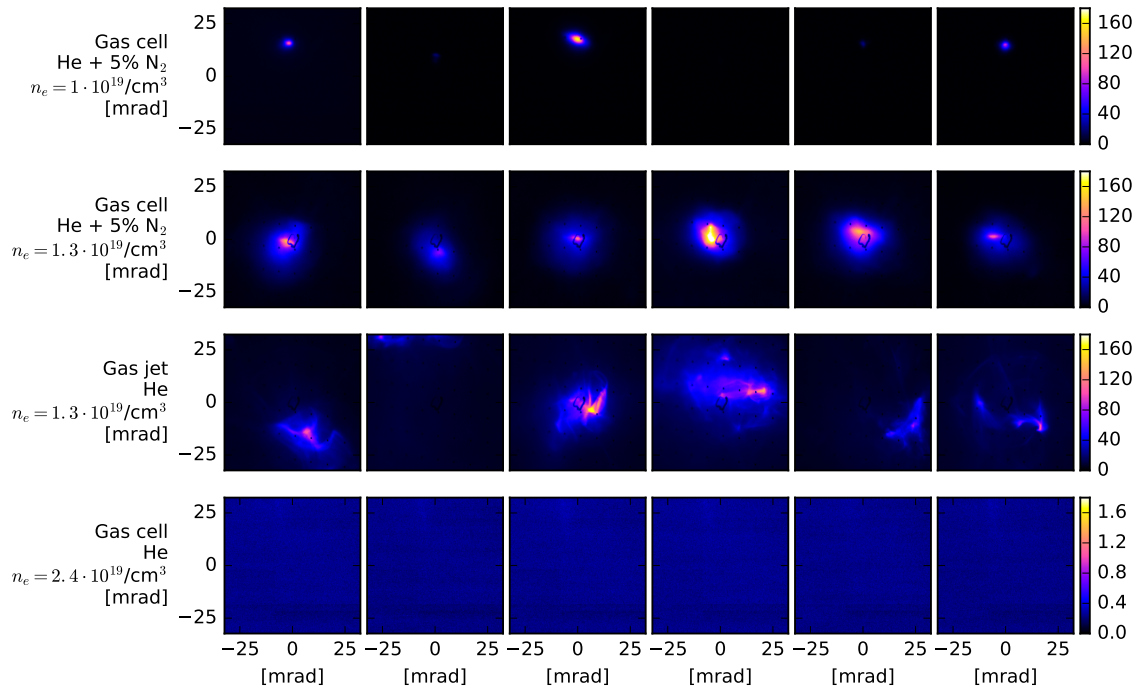Figure 4.4: *Consecutive electron beam profiles for different target configurations as seen on the scintillation screen. The beam profiles of the gas jet (third row) show strong substructure and varying beam shape, whereas the beam profiles of the gas cell (first and second row) are more stable in pointing and beam shape. Using the gas cell with pure He (fourth row) does not accelerate any charge (note the different color scale).*
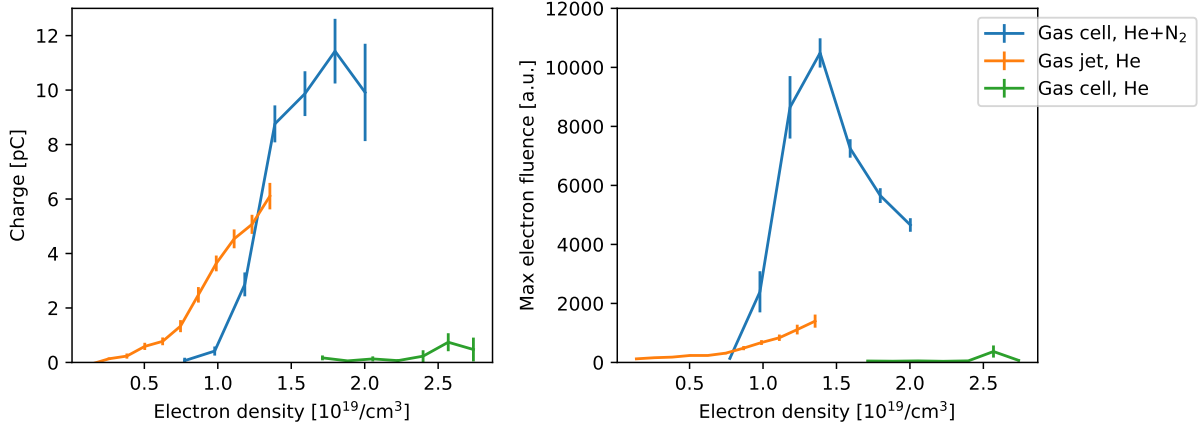
Figure 4.5: *Total accelerated charge and maximum electron fluence on the scintillating screen, depending on the electron density n_e of the target. The total charge increases with increasing electron density (left). The maximum electron fluence shows a clear maximum for the gas jet (right, blue). No charge is accelerated with the gas cell and pure He (red). The uncertainty of the absolute charge scale is estimated as a factor 2. The error bars indicate the variations between the measurements. The maximum of the electron fluence decreases towards the highest densities because more charge is distributed into much larger angles.*

due to increased dispersion and etching. Wave-breaking becomes more likely as β_p is reduced (increasing n_p) which causes more charge to be trapped in case of the gas jet.

Even for larger densities up to $n_e = 2.75 \cdot 10^{19} /\text{cm}^3$, no wave breaking could be observed for the gas cell. The onset of injection in the gas jet was measured to be at $n_e \approx 0.8 \cdot 10^{19} /\text{cm}^3$ (figure 4.5), corresponding to $P/P_c = 1.8$, with P_c the critical power for self-focusig (section 3.2.4). This onset is slightly lower compared to the expectations from other experiments (Froula et al. 2009: $P/P_c = 3$, Mangles et al. 2012: $P/P_c = 2$). Due to the density modulations, β_p in the gas jet has an additional contribution of 3%. Assuming there are no density modulations inside the gas cell, the dispersion and etching terms would have to compensate for these 3% before the plasma wake breaks. This would happen at $n_e > 3.3 \cdot 10^{19} /\text{cm}^3$ and consequently no accelerated electrons would be expected below that density. In the experiment, however, the much larger density would also affect the laser pulse evolution in the plasma. Particularly self-focusing and self-compression may lead to an increased a_0, which suggests to find this threshold at a lower density already. The plasma density in the gas cell experiment was limited to $n_e < 2.75 \cdot 10^{19} /\text{cm}^3$ (corresponding to $P/P_c < 5.5$) due to technical constraints in the experiment and no self-injection could be observed up to this density.

Using ionization injection, a reduction of β_p increases the overlap between the separatrix and the volume in which N^{5+} and N^{6+} are ionized. Consequently more charge is accelerated at larger plasma densities, as observed (figure 4.5). The increase of the overlap may be caused by various reasons: As the electron density increases, the phase velocity of the wake β_p is reduced, which in turn enlarges the separatrix. Also the increased density may lead to stronger self focusing of the laser pulse, which may lead to an increased ionization volume of N^{5+} and N^{6+}. Additionally, the overlap volume may be also affected by the exact pulse shape. However, the increase of charge with increasing plasma density is in line with the predictions of the theory model. Furthermore, an increased overlap of separatrix and ionization volume, would not only lead to more accelerated charge, it also implies, that the electrons populate a larger volume inside the separatrix. As this is a volume of phase space, this model predicts an increased divergence for larger electron densities. In line with this prediction, the measurement (figure 4.6) shows a linear increase of the solid angle Ω with the electron density up to $1.8 \cdot 10^{19}\,/\text{cm}^3$. For plasma densities below $0.8 \cdot 10^{19}\,/\text{cm}^3$ the overlap vanishes and no charge can be ionization injected into the plasma wake. At plasma densities slightly above $0.8 \cdot 10^{19}\,/\text{cm}^3$, the beam's divergence is minimal or the beam randomly disappears, as seen in figure 4.3, first row. In addition the density down-ramp at the exit of the gas cell may decrease the divergence of the electron beam [Shaw et al. 2012].

The divergence of the electron beam, accelerated using the gas jet, does not show any dependence on the electron density within the error bars (figure 4.6). A possible source of the divergence may be tilted density down ramps. They would lead to off-axis injection (simulations in the next subsection 4.5.1) or refraction of the laser pulse (see discussion in the next section 4.6).

It is a reasonable assumption to have density gradients within the gas jet: Due to its supersonic character, those gas jets typically rely on shocks from the nozzle boundary to achieve supersonic flow. In addition the a little ridge on the surface of the nozzle would create an additional shock front in the flowing gas. Detailed characterization of a gas jet using tomographic reconstruction of the plasma density have shown typical variations in the order of $\sim 20\%$ with a spatial resolution of $60\,\mu\text{m}$ [Landgraf et al. 2011]. The width of an artificially induced shock front[2] was measured to be approximately $5\,\mu\text{m}$ at a density transition from $6 \cdot 10^{19}\,/\text{cm}^3$ to $4 \cdot 10^{19}\,/\text{cm}^3$ [Schmid et al. 2010]. Therefore local density variations due to imperfections of the nozzle are far beyond the resolution tomographic reconstruction can provide.

---

[2]The width of the shock front is about 5 to 10 times the molecular mean free path of the gas [Schmid et al. 2010; Mott-Smith 1951].
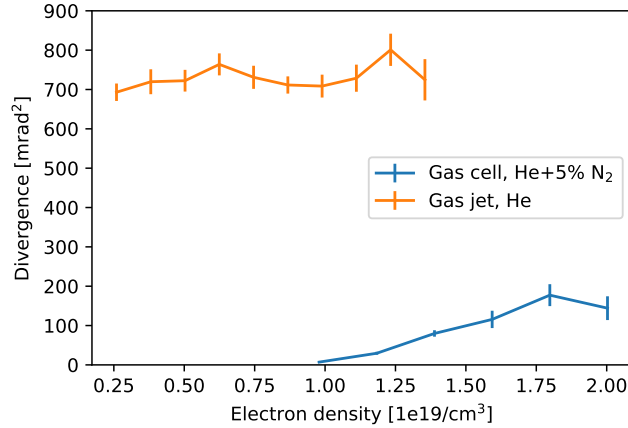
Figure 4.6: *Solid angle Ω of the electron beam depending on the electron density n_e. The divergence was measured by fitting a 2D-Gaussian onto the beam profile. While the divergence of the electron beam accelerated using the gas jet and pure He (self-injection, green) seems almost independent on the plasma density, it increases using the gas cell with He and 5% N_2 (ionization injection, blue).*

Shocks would be visible in transverse probing only if the shock front is parallel to the transverse probing beam, which is unlikely, but occasionally happens. An example of such an occurrence is shown in figure 4.7 (right): The shock front is clearly visible around $x = -50\,\mu$m while a change of the plasma wavelength can also be observed. The change of the plasma wavelength corresponds to the change of the plasma density before and after the shock front. The left picture of figure 4.7 shows another example of a varying plasma wavelength while a shock front is not visible, probably because it is tilted with respect to the probing direction. The extreme case shown in figure 4.7 corresponds to $\frac{\partial \lambda_p}{\partial z}$ of up to 10%.

Figure 4.7 (right) also shows a bright spot at the position where the shock front and the plasma wave intercept. This emission has been described as "wave-breaking radiation" and has been attributed to the extreme acceleration the electrons undergo when the plasma wave breaks [Thomas et al. 2007]. This supports the finding, that electrons are injected when the plasma wave transits a density gradient.

4.5.1 3D PIC simulations of density down-ramps

3D PIC simulations have been performed to evaluate the injection on a density down-ramp. EPOCH3D v4.8.3 has been used sampling a plasma density of $n_p = 1 \cdot 10^{19}$ /cm^3 in a $60 \times 35 \times 35\,\mu$m large box by 1 particle per cell and a resolution of 18 cells/μm
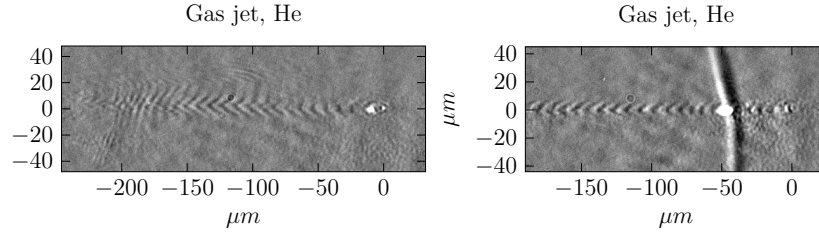
Figure 4.7: *Probing pictures with varying plasma wavelength. Using the gas jet rarely but regularly it happens that pictures with varying plasma are visible. The left pictures shows maximal plasma wavelength $\lambda_p^{max} = 10\,\mu$m (corresponding to $n_e = 1.11 \cdot 10^{19}\,$/cm^3) and a minimal plasma wavelength $\lambda_p^{min} = 5.3\,\mu$m (corresponding to $n_e = 4.0 \cdot 10^{19}\,$/cm^3).*
On the right picture the plasma wavelength changes less dramatically from $\lambda_p^{max} = 9.44\,\mu$m (corresponding to $n_e = 1.25 \cdot 10^{19}\,$/cm^3) to $\lambda_p^{min} = 8\,\mu$m (corresponding to $n_e = 1.74 \cdot 10^{19}\,$/cm^3), while the shock front is visible at the same time.

in propagation direction and $7.5\,$cells/μm in each transverse direction. The density was linearly ramped over $100\,\mu$m centered around $0\,\mu$m. The laser pulse with $\lambda = 800\,$nm, $\tau = 20\,$fs was focused to $6\,\mu$m (FHWM) spot at the center of the density up-ramp ($0\,\mu$m) with a vacuum $a_0 = 3.0$ which ist just below the self-injection threshold for a constant plasma density of $n_p = 1 \cdot 10^{19}\,$/cm^3. Due to the short propagation length, self focusing of the laser pulse can be neglected. After propagation of $50\,\mu$m at the maximum plasma density of $n_p = 1 \cdot 10^{19}\,$/cm^3, the laser plasma wake encounters a down-ramp of $40\,\mu$m length with a variable density gradient.

The trapped charge of the plasma wake depending on the plasma density gradient is shown in figure 4.8. Without a density gradient no charge is injected into the plasma wake. As the density gradient increases, β_p reduces and more charge is injected into the plasma wake and finally accelerated, as the model suggests. Therefore the model, simulations and experimental data are in line and show, that even small scale density variations can trigger the injection of significant amounts of charge.

PIC simulations of a tilted down-ramp have been carried out. A central slice of the simulation just after the end of the down-ramp is shown (figure 4.9). As the tilt angle α increases the electrons are injected off-axis into the plasma wake. Consequently they gain additional transverse momentum, which can also affect the beam's divergence and pointing. As the downramps has been measured in the gas jet, this effect may explain the larger divergence and the differences in pointing stability (next section).

Please note, that another important contribution to β_p within simulations (section 2.2) is numerical dispersion: The discretization of Maxwell's equations leads to a high frequency cut off, where the group velocity of the EM-wave approaches zero. This leads to so
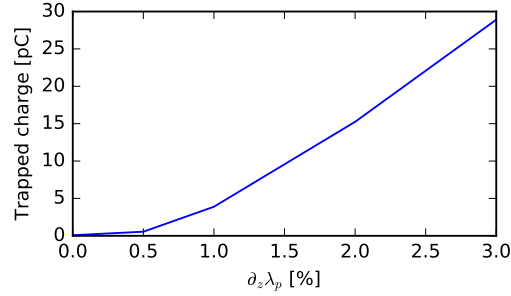
Figure 4.8: *The injected charge in the 3D PIC simulation depending on the density gradient introduced over a downramp of 40 μm length. The density before the downramp was always set to $n_p = 1 \cdot 10^{19}$ /cm³. Without the density gradient no charge has been trapped in the plasma wake. Introducing an additional downramp leads to more reduction of β_p and therefore triggers the injection process. The intensity of the laser pulse was chosen to be on the onset of injection ($a_0 = 3$).*
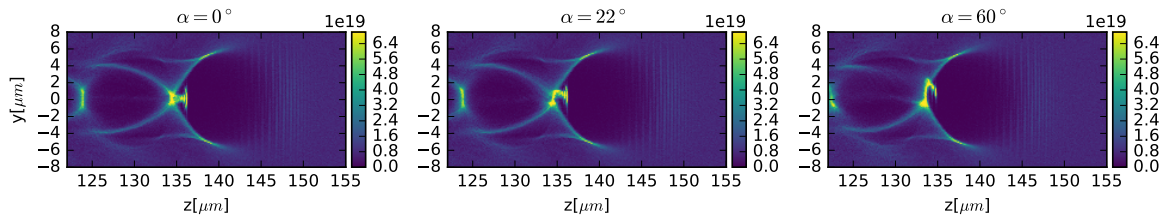
Figure 4.9: *The influence of a tilted downramp on the accelerated elecrtrons: A central slice of the 3D PIC simulation is shown at a position just after the down ramp. The color scale encodes the plasma density in units of $1/cm^3$. The initial direction of the electrons entering the acceleration phase of the plasma wake is changed depending on the tilt angle α of the density gradient. The density gradient is tilted in the y-z plane. The laser pulse had a peak $a_0 = 3$ and the plasma density was set to $n_p = 1 \cdot 10^{19}$ /cm³.*

called numerical dispersion and affects high frequencies most. For low frequencies the grid dispersion relation usually approaches the vacuum dispersion relation. Assuming a standard 3D Yee solver with 15 cells per wavelength in propagation direction of the laser and 6 cells per wavelength along the other two dimensions, the numerical dispersion leads to a reduction of the group velocity of the laser pulse of 0.7%, which is comparable the dispersion by the plasma[3]. To reduce numerical dispersion, pseudo spectral solvers can be used [Lehe et al. 2016; Blaclard et al. 2016] or the computational stencil, used to calculate derivates on the simulation grid, can be extended [Pukhov 1999; Cowan et al. 2013; Lehe et al. 2013]. A systematic approach to the extension of the computational stencil is presented in our recent publication [Blinne et al. 2017].

4.6 Enhanced electron beam pointing stability

The most obvious difference between jet and cell is the increased pointing stability of the gas cell. Figure 4.10 shows the center of mass positions of the electron beam for consecutive laser shots onto the target as seen on the scintillation screen. It is clearly visible, that the electrons beam centers cover a much more confined area using the gas cell. In order to evaluate the pointing stability, the covariance matrix $\Sigma = \begin{pmatrix} \text{var}(x) & \text{cov}(x,y) \\ \text{cov}(x,y) & \text{var}(y) \end{pmatrix}$ of the electron beam directions was calculated. The eigenvalues of Σ are the variances along the short and the long axis of the distribution. The black ellipse in figure 4.10 visualizes the standard deviation (square root of variance $= 1\sigma$ confidence region) ellipse of the 2D-Normal distribution[4] enclosing the solid angle $\Omega = \pi \cdot \Delta\theta_1 \Delta\theta_2$. Consequently, the area of the standard deviation ellipse is a good measure for the solid angle covered by the electron beam and therefore for the pointing stability of the electron beam. For the gas jet and the gas cell, the plasma density was independently found to be at optimized conditions at $n_e = 1.3 \cdot 10^{19}$ /cm^3. The solid angle decreased from $\Omega^{\text{jet}} = 490 \, \text{mrad}^2$ to $\Omega^{\text{cell}} = 48 \, \text{mrad}^2$, which demonstrates an order of magnitude in beam pointing enhancement. For both targets the pointing stability showed only little dependence on the plasma density.

There are various possible sources for the (residual) pointing fluctuations of the electron beam, which should be discussed now.

---

[3]Counter intuitively, a reduction of transverse resolution increases the phase velocity of the laser pulse in propagation direction.

[4]Note, that the 1σ, 2σ, 3σ confidence levels correspond to the well known probabilities 68%, 95%, 99.7% under the assumption of a 1D-Normal distribution. In the 2D case discussed here also analytic expressions are available and the corresponding probabilities are $1 - e^{-\frac{1}{2}} \approx 39\%$, $1 - e^{-2} \approx 86\%$, $1 - e^{-\frac{9}{2}} \approx 98.9\%$
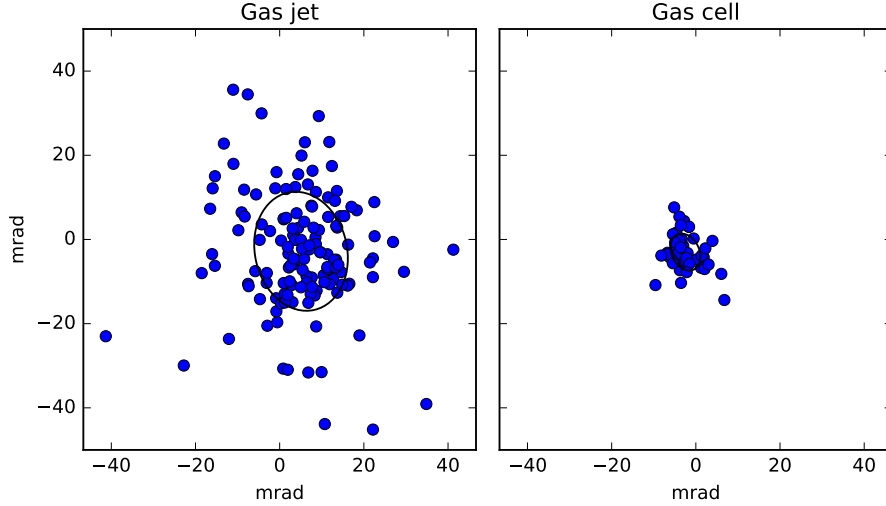
Figure 4.10: *Electron beam pointing stability of gas jet and gas cell: each blue dot represents the center of mass of single electron beam. 140 consecutive shots are shown for the gas jet, 50 consecutive shots are shown for the gas cell. The standard deviation (black ellipse) decreases from $\Omega^{jet} = 490\,\mathrm{mrad}^2$ to $\Omega^{cell} = 48\,\mathrm{mrad}^2$. The electron density was $n_e = 1.3 \cdot 10^{19}\,/\mathrm{cm}^3$, which are optimized conditions in both cases. The pulse of the JETI40 laser was focused by an f/12 parabolic mirror to a vacuum intensity of $a_0 = 2.2$.*

laser farfield The movement of the farfield of the laser can be easily estimated: A position shift in the focal plane of the parabola by one diffraction limited spot diameter corresponds to the angular tilt of

$$\Delta\theta = \frac{4\pi}{\lambda} \cdot \frac{1}{d} \tag{4.2}$$

which evaluates for our conditions to $\Delta\theta = 0.02\,\mathrm{mrad}$ or $\Omega = 0.001\,\mathrm{mrad}^2$. Typically the focus is moving by ~ 2 to 3 spot diameters and therefore this contribution can be neglected safely.

laser nearfield The nearfield profile f the laser shows intensity variations, as clearly visible on the monitoring screens of the laser system. Nearfield profiles of consecutive shots before the compressor have been recorded. The intensity variation leads to a shift of the center of mass of the beam profile of $\Delta\theta \approx 0.5\,\mathrm{mrad}$ or $\Omega = 0.75\,\mathrm{mrad}^2$ which is a negligible contribution compared to the measured stability. However, ultimately this may become significant if other sources can be reduced.

laser focal spot changes The intensity and phase variation of the laser system also lead to slight variations of the shape of the focus. The influence of these variations is hard to estimate but it is quite clear that hot spots within the first airy ring will self-focus in the plasma and drive a second plasma wake with much lower amplitude

than the main plasma wake, but in close proximity to it. The additional wake field can of course influence the main wake and alter its exact shape as well as properties of the accelerated electrons. Therefore it is hard to find a genuine estimate how strongly the electron beam pointing may be influenced.

refraction on density gradients The influence of a density gradient parallel to the propagation direction of the laser on wave-breaking has already been discussed in section 3.2.3. Transverse gradients can also change the propagation direction of the laser due to refraction. The magnitude of this effect shall be estimated in the following. For $\omega \gg \omega_p$ the index of refraction η is given by equation 2.32:

$$\eta = 1 - \frac{1}{2}\frac{\omega_p^2}{\omega^2} = 1 - \frac{n_p}{2n_c} \tag{4.3}$$

Using Snell's law of refraction $\eta_1 \sin \alpha_1 = \eta_2 \sin \alpha_2$ the angular deviation due to refraction is given by

$$\Delta\alpha = \arcsin\left(\eta_2/\eta_1 \cdot \sin\alpha\right) - \alpha \tag{4.4}$$

with the angle of incidence α and the ratio of refractive indices, which can be simplified to

$$\frac{\eta_2}{\eta_1} = \frac{2n_c - n_2}{2n_c - n_1} \tag{4.5}$$

and approximated if $n_1 \ll n_c$ and $n_2 \ll n_c$

$$\frac{\eta_2}{\eta_1} \approx 1 + \frac{n_1}{2n_c} - \frac{n_2}{2n_c} = 1 - \frac{\Delta n}{2n_c} \tag{4.6}$$

A Taylor expansion of $\Delta\alpha$ at $\alpha = 0$ finally yields

$$\boxed{\Delta\alpha = \frac{\Delta n}{2n_c}\alpha + \mathcal{O}(\alpha^3)} \tag{4.7}$$

The extreme value of $\Delta\alpha$ is reached for grazing incidence and it can be obtained with a Taylor expansion of $\Delta\alpha$ with respect to Δn at $\alpha = \pi/2$, which yields the surprisingly simple result $\Delta\alpha_{\mathrm{max}} = \sqrt{\frac{\Delta n}{n_c}} + \mathcal{O}(\Delta n^{3/2})$.

Assuming a large plasma density transition of $\Delta n = 1 \cdot 10^{19}/\,\mathrm{cm}^3$ and for a wavelength $\lambda = 800\,\mathrm{nm}$ the factor $\Delta n/n_c \approx 5.7 \cdot 10^{-3}$. This leads to a deviation of the laser propagation direction by $\Delta\alpha \approx 2.2\,\mathrm{mrad}$ ($\Omega = 15\,\mathrm{mrad}^2$) if the density transition is oriented at $\alpha = 45°$. However, the influence is much larger for shallower angles: As $\alpha \to \pi/2$ the laser is deviated by up to $\Delta\alpha_{\mathrm{max}} \approx 77\,\mathrm{mrad}$.

The shift of the laser propagation direction induces a mismatch between the laser- and the electron propagation direction. The deviation of the laser pulse therefore translates to a deviation of the accelerated electrons.

standing density wave inside the gas cell A pointing deviation which is specific to the gas cell may be caused by low order transverse eigenmodes inside the gas cell. The gas cell has a diameter of $d = 9\,\mathrm{mm}$. The lowest order standing wave, contribution to a density gradient on axis is

$$n(y) = n_0 + \Delta n \cdot \sin\left(2\pi \frac{y}{d}\right) \tag{4.8}$$

Assuming $\Delta n = 0.1 \cdot 10^{19}/\mathrm{cm}^3$ the gradient on axis evaluates to $\partial_y n = 0.07 \cdot 10^{19}\,\frac{1}{\mathrm{cm}^3} \cdot \frac{1}{\mathrm{mm}}$ and consequently the index of refraction to $\partial_y \eta = \frac{\partial_y n}{2 n_c} = 2.1 \cdot 10^{-4}/\mathrm{mm}$. This leads to a deviation of the laser with a radius of curvature of $R = \frac{\eta}{\partial_y \eta} \approx 5\,\mathrm{m}$. The collected angular laser deviation over the length of the gas cell ($2\,\mathrm{mm}$) can therefore be estimated as $\Delta\alpha \approx 2/5000 = 0.4\,\mathrm{mrad}$.

Judging from this simple calculation it seems reasonable to assume a minor influence on the pointing of the gas cell assuming modes are building up inside the cell. A thorough analysis is required since there is currently no indication if longitudinal gas density modes are present within the cell at all. Higher order modes would lead to a stronger deviation but also undergo stronger damping due to their higher eigen-frequency.

The calculation suggests, that refraction of the laser pulse is likely to be the leading contribution to the pointing in-stability of the electrons when accelerated using the gas jet. Density modulations of up to $3 \cdot 10^{19}/\mathrm{cm}^3$ have been measured and there are multiple density transitions inside the plasma. Thus their individual contributions sum up to the final pointing stability. They influence the electron beam in two ways: First the laser propagation direction is changed and secondly a tilted down-ramp will also affect the injection process and may lead to a tilted injection (figure 4.9). Due to the mismatch of laser- and electron propagation direction, electrons injected after a directional shift will consequently populate shifted positions in phase space, which indicates that this process contributes to the divergence of the final electron beam in case of the gas jet and possibly explain the structured beam profiles (see section 4.4): When multiple down-ramps trigger injection repeatedly with random orientations, the final beam is expected to consist of multiple beamlets. However, wave-breaking is a highly non-linear process, which may cause the structured profiles or the divergence of the beam.

For the gas cell, the reduction of the localized density modulations is most likely to be the reason for the enhanced pointing stability compared to the gas jet. However, the

residual pointing fluctuations are larger than the sum of the contributions discussed here. It is possible, that the focal spot changes of the laser have a significant influence on the pointing of the electron beam. Another possibility is the presence of undetected density modulations: The sensitivity of the plasma wake imaging not better than $\partial_z \lambda_p = 0.25\%$ and a smaller gradient would not be detected by this method. Residual modulations can still be present in the gas cell. In particular, modulations over a long spatial scale would be undetected. Such modulations would not affect wave breaking, as this is depending on the gradient of the plasma density. The refraction of the laser pulse, however, is depending on the accumulated phase difference, which can still be a significant contribution.

4.7 Discussion

The increase of stability of the LWFA electron beam is of vital importance for future experiments. The newly developed gas cell provided a much smoother plasma density on a $10\,\mu m$ scale compared to the standard gas jet. In addition the data shows that these density modulations in the gas jet are the major contribution to the phase velocity of the plasma wake β_p. (equation 4.1). This is an important observation in two ways:

1. Even small density variations, as present in the gas jet, can trigger the injection process. This is the first time, that density variations on a $10\,\mu m$ scale have been resolved in an LWFA target and were linked to the process of wave-breaking and therefore injection.

2. The suppression of self-injection can be used for a background-free LWFA: Such an accelerator should have a density profile homogeneous enough to ensure, that the dispersion and etching terms are the leading contribution to the phase velocity of the plasma wake, i.e. $\frac{\partial \lambda_p}{\partial z} < \frac{3}{2} \frac{n_p}{n_c}$.

The requirement on the homogeneity of the plasma density becomes even more important, when LWFA is scaled up: In order to overcome dephasing (section 3.2.5) higher electron energies require lower plasma densities. The dispersion and etching terms (equation 4.1) are proportional to the plasma density. The downramp term can be written in terms of the plasma density (equation 3.47): $\left|\frac{\partial \lambda_p}{\partial z}\right| = \frac{\pi c \sqrt{m \varepsilon_0}}{q_e} n_p^{-3/2} \frac{\partial n_p}{\partial z}$. Therefore the just introduced homegeneity requirement reads $\left|\frac{\pi c \sqrt{m \varepsilon_0}}{q_e} n_p^{-3/2} \frac{\partial n_p}{\partial z}\right| < \frac{3}{2} \frac{n_p}{n_c}$ or more conveniently $\left|\frac{\lambda_p}{2 n_p} \frac{\partial n_p}{\partial z}\right| < \frac{3}{2} \frac{n_p}{n_c}$. It is clear that it becomes increasingly difficult to control the downramp term for smaller densities due to its very unfavorable $n_p^{-3/2}$ scaling.

The self-injection free plasma wake is an important step towards shaping the spectrum of the electrons. If injection happens in one distinct location of the acceleration process only, the final electron spectrum can have a narrow bandwidth and well definded final energy. The possibility of having a background-free acceleration process is a prerequisite to this important step. Further experiments involving the JETI 100 laser system are planned to investigate alternate injection mechanisms in order to gain control over the spectrum of the final electron beam.

As a result of this smoother density profile and controlled injection, the newly developed gas cell has also improved the general shape and reproducibility of the electron beam profile (figure 4.4). The structured beam profiles of the gas jet are likely caused by the same density variations that lead to self-injection. Two mechanism can be identified, which may cause the structured electron beam in the jet: Refraction of the laser at a density variation leads to an additional angular component of the electrons (section 4.6).

Secondly, a tilted down-ramp may also lead to additional transverse momentum of the electron beam at the point of injection. As injection is likely to be triggered repeatedly on multiple downramps in the gas jet, the final electron beam is expected to consist of multiple beamlets, which may be the cause of the measured structured beam profiles. Further studies, preferably by simulations would be needed identify which of the mechanisms is the leading effect. However, the gas cell shows a much smoother electron beam profile.

The use of the gas cell also improves the pointing stability of the accelerated electrons by an order of magnitude in solid angle Ω. The divergence of the electron beam has also improved from $\sim$750 mrad^2 (jet) down to 16 mrad^2 (cell) in optimized conditions. The enhanced divergence is likely to be caused by the absence of density modulations, which can cause injection. Another factor is the longer density down-ramp at the exit of the gas cell, which may decrease the divergence [Shaw et al. 2012].

The results are in line with a stability analysis of LWFA on a similar laser system [Hansson et al. 2014]. The reported divergence of 14 mrad (600 mrad^2) is very similar to the gas jet measured here (750 mrad^2) and only improves slightly using a capillary (400 mrad^2). This suggests, that the divergence may be caused by the highly non-linear wave-breaking process itself or a possible density variation at the position of the gas inlet. Their pointing stability of a gas jet (60 mrad^2) is similar to the pointing stability the newly developed gas cell (50 mrad^2) and is further enhanced down to 5 mrad^2 when using a capillary. This enhancement may be caused by an even more homogeneous gas density inside the capillary, particularly as density variations on a long spatial scale would not be detected by the transverse probing inside the gas cell.

The homogeneous density profile of the gas cell is also important to study the wave-breaking process. When increasing the intensity of the laser pulse further, also the amplitude of the wake increases, making it more likely to break even in homogeneous plasmas. Even without density modulations the slow down of the phase velocity of the wake β_p due to etching and dispersion will be sufficient to trigger wave-breaking and therefore injection. This is a strongly non-linear process, which may inherently cause structured electron beam profiles or the large beam divergence. The current data cannot exclude this possibility in the case of self-injection. Future experiments at the JETI 100 laser system of the Helmholtz-Institute Jena are in preparation to clarify this question.

5 Focusing electron pulses by a plasma lens

Reshaping and transportation of an electron beam is required to deliver a high electron fluence on the target. For conventional collision experiments this is described by the luminosity $L = \frac{N_1 N_2}{4\pi\sigma_1\sigma_2}$, where N_1, N_2 are the numbers of particles of the colliding beams and σ_1, σ_2 are the beam sizes at the interaction point. Conventional accelerators typically use quadrupole magnets to focus the beam. The first magnet focuses one of the transverse directions while it defocuses the other. The second magnet is rotated with respect to the first such that both transverse directions are focused at a single point. Due to defocus-refocus scheme, those magnet pairs (or sometimes triplets) have a very strong dependence on the electron energy or – in other words – create strong chromatic aberrations in the electron beam. However, radio frequency (RF) accelerators have a typical energy bandwidth of $\Delta E/E \lesssim 0.1\%$ and chromatic aberrations may be neglected.

Plasma lenses have potential advantages over conventional beam focusing: First, laser plasma based accelerators create electron bunches with a much larger energy bandwidth up to a continuous spectrum. Therefore they require lenses with much lower chromatic aberration. Plasma lenses typically focus both transverse beam directions at once and have therefore less chromatic aberrations. Secondly, plasma based accelerators are very compact in size compared to conventional ones. It would therefore be appealing to be able to build devices for beam shaping and transport on a similar spatial scale, possibly for final beam focusing [Chen 1987]. Third, the focusing strength reached by plasma lenses can exceed the strength of quadrupole magnets by orders of magnitude, which allows for much stronger focusing. In the conclusion of this chapter the focusing strengths of different focusing methods will be discussed (section 6.4).

5.1 Concept of plasma lensing

Since the advent of RF accelerators there was increasing interest in methods to focus their electron beams. In a relativistic beam, a basic observation is that the electric self-

forces of the beam act repulsively while the magnetic self-forces act to pinch the bunch together. As shown in section 5.1.2 these forces cancel in the ultra relativistic limit ($\beta \to 1$). Consequently the focusing magnetic forces may overcome the repulsive electric forces if a sufficient fraction of the beam's charge is neutralized. This idea was first outlined and demonstrated by Gabor 1947: In his experiment an ion beam propagated through an electron plasma held in a magnetic trap.

The majority of publications in the 1990s did not distinguish between active and passive plasma lensing and the term "plasma lens" was mostly attributed to the dynamics of a particle beam passing through a plasma in the 1990s, which corresponds to passive plasma lensing. However, a generally recognized definition is still missing throughout the literature, which is why this section is proposing a definition for those terms.

Govil et al. 1999 defines a *passive* plasma lens as a plasma lens, where the particle beam is passing though a plasma *without external currents* applied. Within this thesis I would like to redefine the *passive* plasma lens as a plasma lens where *all focusing fields are created by the particle bunch itself or by the plasma in response to it*. This might seem a minor change in definition, but it sets a clear boundary to any kind of additional source of focusing forces, which could be some external current (as excluded by Govil), but also another particle bunch or an additional focused laser beam.

Instead of compensating the repulsive electric force by neutralizing the beam's charge, it can also be compensated by an additional magnetic field. This approach utilizes a longitudinal current (z-pinch) in a medium transparent to the particle beam. This longitudinal current creates an azimuthal magnetic field, which causes a charged particle beam to focus or defocus. This active beam focusing has been demonstrated with an ion beam at Berkeley [Panofsky et al. 1950] and was reproduced at the GSI (Darmstadt, Germany) 43 years later [Boggasch et al. 1993] with much stronger focusing than the original "Gabor" lens. This is an example for *active* plasma lensing. In *active* plasma lensing the *focusing fields are generated by any kind of external driver*. The most prominent example is the already mentioned longitudinal current creating an azimuthal magnetic field as in Panofsky et al. 1950 or Boggasch et al. 1993. The exact same principle has recently been demonstrated with a laser wake field accelerated electron bunch by Tilborg et al. 2015 confining the external current inside a capillary.

Another approach to an active plasma lens scenario has been shown recently: Thaury et al. 2015 accelerated an electron bunch using LWFA and changed its divergence in a second plasma stage: The preceding laser pulse excites a wake field in the second stage and the electrons are focused due to the transverse electric field within that plasma wake. The dominant focusing electric field was therefore created by the charge separation caused by the laser pulse, as reported by the authors.

5.1.1 Over- and underdense passive plasma lensing

Passive plasma lensing has been investigated around the 1990s and several experiments have been carried out using particle beams accelerated with conventional accelerators (i.e. [Su et al. 1990; Rosenzweig et al. 1990; Nakanishi et al. 1991; Hairapetian et al. 1994; Ng et al. 2001]). Since those particle (electron) beams are long compared to their transverse size, the theoretical derivations often assume an infinitely long electron beam or, to be more precise, $\sigma_\parallel/c \gg \omega_p$. Plasma lensing in general is also divided into the *overdense* and the *underdense* regime.

A plasma is called *overdense* with respect to a laser if the density of the plasma n_p is larger than the characteristic (plasma) density associated with the frequency of the laser pulse, which is the critical density n_c, therefore $n_c \ll n_p$. Analogously a particle bunch with a density n_b is called *overdense* to another plasma if $n_b \gg n_p$. In this regime the plasma can compensate charges and currents of the particle bunch up the times and length scales, which are characteristic to the plasma and therefore are given by the plasma frequency. The passive plasma lensing demonstrated in this thesis is in the overdense regime, which will be discussed in detail in section 5.2.

The *underdense* regime is the other extreme, where $n_b \gg n_p$. In this regime the fields of the bunch are strong enough to drive a non-linear plasma wake which changes the plasma response significantly. This regime will be briefly discussed in section 5.3.

Before going into the details of these two regimes some underlying principles will be discussed that are equal common to cases. Particularly the fields and forces of two co-moving charges will be evaluated before proceeding to the actual mechanisms in the over- and underdense regimes.

5.1.2 Fields and forces of relativistically co-moving charges

The forces between two co-moving charges are an instructive example in order to understand the principle of passive plasma lensing. Consider a stationary electric charge with the charge q at the origin of the system K. It will not create any magnetic field because there are no currents. The electric field of the charge is given by:

$$\boldsymbol{E} = \frac{q\boldsymbol{r}}{r^3} \tag{5.1}$$

A second test charge (producing no fields) of the same kind, positioned at the point $\boldsymbol{P} = (0, b, 0)$ would therefore experience the force $\boldsymbol{F}$:

$$\boldsymbol{F} = \frac{q^2}{b^2} \boldsymbol{e}_y \tag{5.2}$$

$\boldsymbol{F}$ is directed such that it will push the particles apart from each other. Assume that the system K is actually moving with respect to the laboratory system K'. In addition to an electric field the moving charge would also create a current which creates a magnetic field. These solutions can be obtained by Lorentz-boosting the electro-magnetic fields from K into K'. If the direction of the boost is the x-direction the field transformation equations are [Jackson 2006]:

$$\begin{aligned} E'_x &= E_x & B'_x &= B_x \\ E'_y &= \gamma(E_y - \beta B_z) & B'_y &= \gamma(B_y + \beta E_z) \\ E'_z &= \gamma(E_z + \beta B_y) & B'_z &= \gamma(B_z - \beta E_y) \end{aligned} \tag{5.3}$$

In the point P the fields transform to:

$$\begin{aligned} E'_x &= 0 & B'_x &= 0 \\ E'_y &= \gamma E_y & B'_y &= 0 \\ E'_z &= 0 & B'_z &= -\gamma\beta E_y \end{aligned} \tag{5.4}$$

The force $\boldsymbol{F}'$ acting on an identical charge in the co-moving point P as seen by the system K' is therefore

$$\boldsymbol{F}' = q\left(\boldsymbol{E}' + \boldsymbol{\beta} \times \boldsymbol{B}'\right) \tag{5.5}$$

$$= \frac{q^2}{b^2}\gamma\left(\underbrace{1}_{\text{el}} - \underbrace{\beta^2}_{\text{mag}}\right)\boldsymbol{e}_y \tag{5.6}$$

$$= \frac{q^2}{b^2\gamma}\boldsymbol{e}_y \tag{5.7}$$

The force $\boldsymbol{F}'$ is always repulsive between the two identical charges, because $\beta < 1$. In the case of non-moving particles ($\gamma = 1 \Rightarrow \beta = \sqrt{1 - \frac{1}{\gamma^2}} = 0$) this result is identical to equation 5.2. It is important to note that the faster the particles are moving the weaker the repulsive force between them becomes and in the ultra relativistic limit $\gamma \to \infty$ the repulsive force between the particles vanishes. Equation 5.6 shows clearly how this mechanism works, because the forces acting on the particle are still decomposed in an electric (el) and magnetic (mag) part. Although the repulsive electric contribution

increases with γ, the attracting magnetic contribution scales with $\gamma\beta^2$ to compensate the repulsion.

Assuming further, that a fraction f_e of the charge is neutralized. The current remains unaffected and therefore the magnetic field is not changed either. The electric force gains an additional factor $(1 - f_e)$:

$$\boldsymbol{F'} = \frac{q^2}{b^2} \left((1 - f_e)\gamma - \gamma\beta^2 \right) \boldsymbol{e}_y \tag{5.8}$$

$$= \frac{q^2}{b^2}\gamma \left(- f_e + \underbrace{1 - \beta^2}_{1/\gamma^2} \right) \boldsymbol{e}_y \tag{5.9}$$

$$= \frac{q^2}{b^2}\gamma \left(\frac{1}{\gamma^2} - f_e \right) \boldsymbol{e}_y \tag{5.10}$$

The force $\boldsymbol{F'}$ between the particles becomes attractive when $f_e > \frac{1}{\gamma^2}$, which is the so called *Budker condition of self-focusing* [Reiser 2008]. This condition is not only valid for two co-moving charges, but also for an entire electron beam. The particles of an electron beam experience an attractive force towards the axis of the beam, if f_e is larger than $1/\gamma^2$. In case of an relativistic ($\gamma \gg 1$) electron beam, $1/\gamma^2$ approaches zero and even a very small f_e is sufficient to result in an attractive force between the particles, which is a focusing force. In passive plasma lensing the charge neutralization f_e is provided by the plasma.

5.2 Overdense regime $\left(n_p \gg n_b \right)$

If the electron bunch density n_b is much smaller then the neutral plasma density n_p the bunch is passing through, this is called the *overdense* regime. Most experiments of passive plasma lensing – including the one presented in the Chapter 6 – are in this regime. For selected parameters, results of 3D PIC simulations are shown in this section to visualize the focusing effect. Also an analytical model will be introduced, which is valid for the special case of a long bunch.

long electron bunches

A long bunch in this context means that it is long compared the plasma wavelength of the background plasma. This can be easily understood by realizing that the plasma responds to an external force on the timescale of the plasma frequency (section 3.1). More precisely, the term *long* bunch will be used throughout this thesis for a bunch with
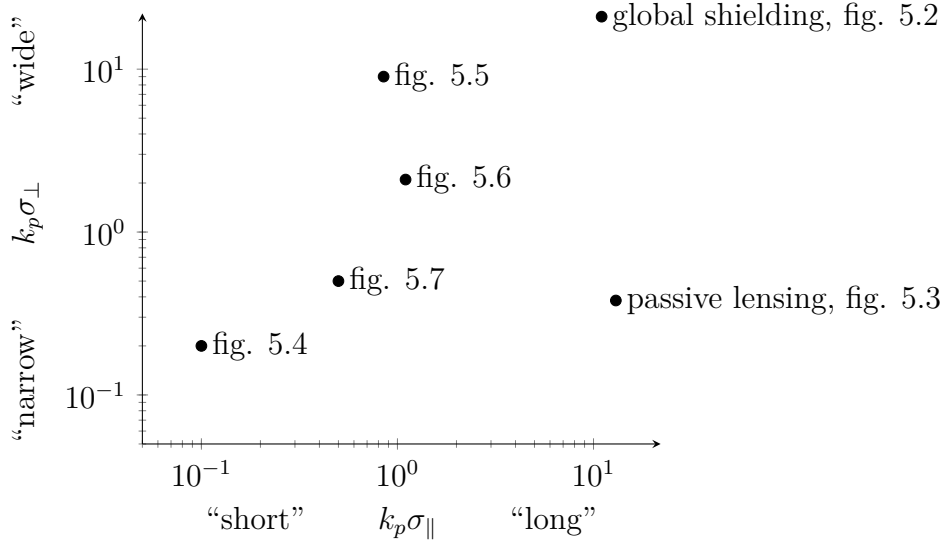
Figure 5.1: *Overview of the regimes corresponding to the selected simulations.*

$k_p\sigma_\parallel \gg 1$, where $\sigma_\parallel$ is the longitudinal extent of the bunch. Accordingly a *short* bunch is charaterized by $k_p\sigma_\parallel \ll 1$.

In analogy, two more regimes need to be distinguished depending on the width ($\sigma_\perp$) of the bunch. A bunch with $k_p\sigma_\perp \gg 1$ will be referred to as a *wide* bunch, while a bunch with $k_p\sigma_\perp \ll 1$ will be called a *narrow* bunch.

Depending on the values of $k_p\sigma_\parallel$ and $k_p\sigma_\perp$ different regimes are entered in which focusing may or may not occur. This is discussed in the following and 3D PIC simulations have been carried out for selected parameters. An overview of the selected parameters is given in figure 5.1. The resolution of the simulation was set to 1 or 2 cells per μm using 1 or 2 macro particles per cell for sampling of the background plasma. The size of the simulation box varies depending on the bunch size and was set to $64 \times 200 \times 200$ μm in most cases.

At first, two cases will be discussed: The case of ideal passive plasma lensing (long and narrow bunch) and the case of global shielding (long and wide bunch). Both can be described by a model developed by Whittum et al. 1990 and Chen et al. 1987, which will be introduced.

When the transverse and longitudinal size of the bunch is large (long and wide), the plasma shields all the self-fields of the bunch. The plasma will match the density profile of the bunch, totally neutralizing its charge [Whittum et al. 1990]. In addition the plasma compensates the current of the bunch mitigating the magnetic field. As all self-forces (electric and magnetic) of the bunch are suppressed, this scenario results in a
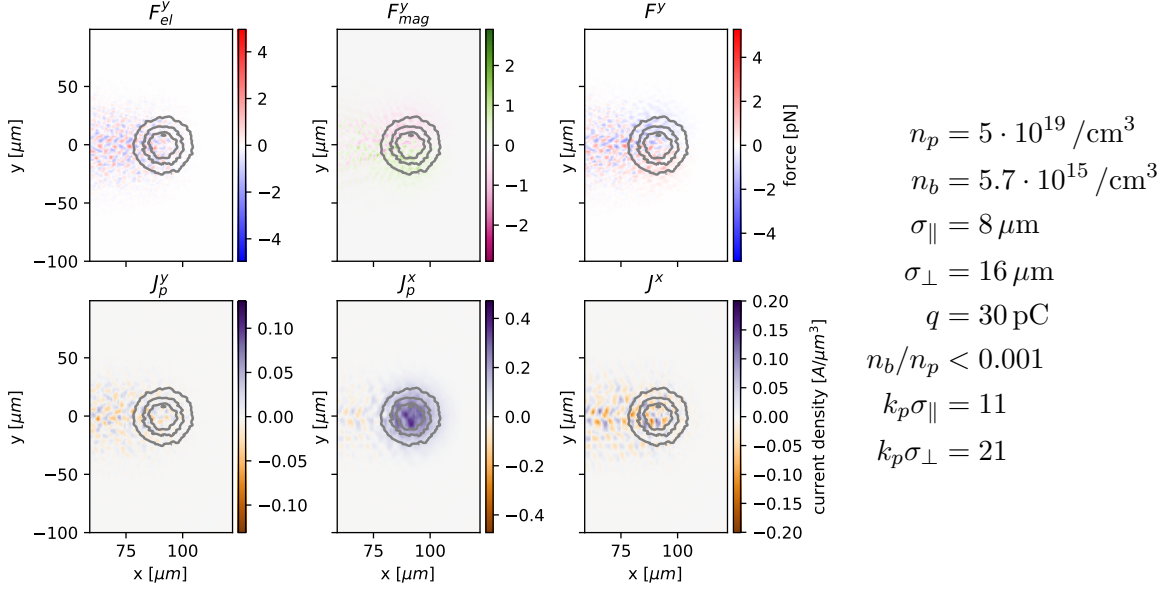
Figure 5.2: *The transverse and longitudinal extent of the particle bunch is much larger than the plasma wavelength and the electric and magnetic forces are therefore greatly shielded by the plasma. The upper row shows the forces originating from transverse electric and magnetic fields. For the calculation of the magnetic lorentz force $\beta = c$ is assumed. Their sum is shown as the total force F^y. The lower row displays the transverse (J_p^y) and longitudinal (J_p^x) plasma current. The net current $J^x = J_p^x + J_{bunch}^x$ is shown on the lower right. The electron bunch is indicated by the gray contour lines at $1/\sqrt{2}$, $1/2$ and $1/4$ of the maximum bunch density and moves from left to right.*
Note, that the current of the background plasma J_p^x in this scenario matches the bunch's current distribution, effectively neutralizing it ($J^x \approx 0$).

theoretically force-free propagation of the electron beam and is the concept of "Plasma suppression of beamstrahlung" [Whittum et al. 1990].

The in-principle force-free scenario is depicted in figure 5.2: The upper row shows the force originating from the transverse electric field (F_{el}^y) and the transverse magnetic field (F_{mag}^y) as well as their sum (F^y). For the calculation of the force $v = c$ was assumed which is justified for any relativistic electron beam ($\gamma \gg 1$). The lower row shows the transverse current of the plasma (J_p^y), the longitudinal current of the plasma (J_p^x), and the total longitudinal current (J^x), which is the sum of J_p^x and the longitudinal current caused by the electron bunch itself. The electron bunch is indicated by the gray contour lines at $1/\sqrt{2}$, $1/2$ and $1/4$ of the maximum bunch density. It can be seen that the forces in the plasma cancel on a global scale. The residual forces are on the scale of the plasma wavelength and should not be discussed here.

Ideal plasma lensing requires the bunch to be long and narrow (figure 5.3). The basic concept of the ideal passive plasma lensing case is as the calculation of the force of

The plots show, in the top row: F_{el}^y, F_{mag}^y, F^y (force [pN]); in the bottom row: J_p^y, J_p^x, J^x (current density [A/μm^3]), with axes y [μm] and x [μm].

$$n_p = 1 \cdot 10^{18} \,/\mathrm{cm}^3$$
$$n_b = 5 \cdot 10^{16} \,/\mathrm{cm}^3$$
$$\sigma_\parallel = 68 \,\mu\mathrm{m}$$
$$\sigma_\perp = 2 \,\mu\mathrm{m}$$
$$q = 50 \,\mathrm{pC}$$
$$n_b/n_p = 0.05$$
$$k_p\sigma_\parallel = 13$$
$$k_p\sigma_\perp = 0.38$$
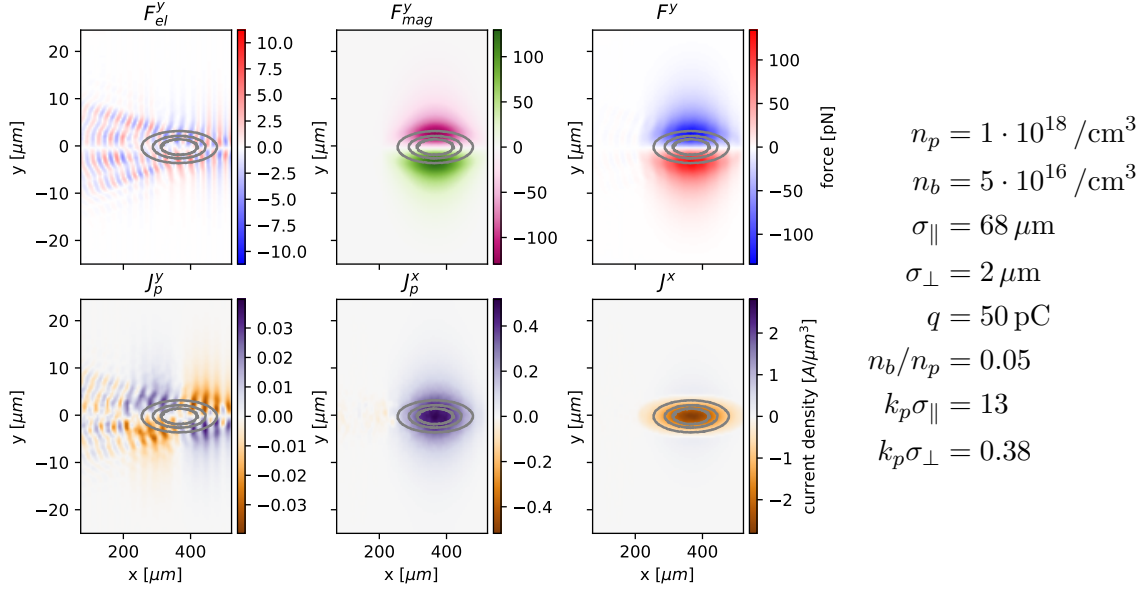
Figure 5.3: *The typical passive plasma lensing scenario: The particle bunch is much longer than the plasma wavelength ($k_p\sigma_\parallel \gg 1$) which is why the charges of the plasma can easily rearrange to neutralize the bunch's charge and therefore its electric field (see F_{el}^y).*
The transverse size is much smaller than the plasma wavelength and therefore a significant fraction of the return currents is flowing outside of the bunch (see J_p^x) making current compensation and therefore magnetic field shielding ineffective. The residual magnetic field F_{mag}^y dominates the total transverse force on the bunch F^y and pinching it together. The fast modulation, visible in F_{el}^y and J_p^y is on the scale of the plasma wavelength and should not be discussed here.

two co-moving charges (section 5.1.2) suggests. The intent is a scenario, in which the charges of the bunch are neutralized, while the current of the bunch is not [Chen 1987]. As the bunch is long, the charges in the plasma are rearranging to compensate for the charge of the bunch, which in turn compensates its repulsive electric field. This charge compensation by the plasma can be actually seen in figure 5.3: J_p^y shows a transverse inwards directed current at the head of the bunch, indicating the movement of plasma electrons away from the bunch, while an outwards directed current at the tail of the bunch. In turn F_{el}^y is strongly attenuated. As the bunch is narrow ($k_p \sigma_\perp < 1$) a large portion of the return current is radially located outside of the bunch (seen in J_p^x). Therefore a net current J^x remains, which is the current creating the magnetic fields. In total, the repulsive electric field is well-shielded, while the focusing magnetic field remains, leading to the net focusing effect of passive plasma lensing.

Scaling of the focusing strength (transverse direction)

For the special case of passive plasma lensing with a long bunch, an analytical scaling is available in the literature [Chen et al. 1998; Chen et al. 1987; Rosenzweig et al. 1989]. The lens is characterized by its *focussing strength K*. Focussing strength and focal length f have the relation

$$\int K \, \mathrm{d}s = \frac{1}{f} \tag{5.11}$$

for a thin lens, that is $\int \mathrm{d}s \ll f$.

The focusing strength K of a passive plasma lens and for a long and narrow bunch is given by Chen et al. 1998[1]:

$$K = \frac{2\pi r_e}{\gamma} n \tag{5.12}$$

where $n = \min(n_p, n_b)$ is determined by the lower of the two densities n_p or n_b. In the overdense regime discussed here, $n = n_b$ by definition. This formula approximates the focusing strength under the assumption of ideal conditions (similar to figure 5.3): The electric field is fully compensated while the magnetic field is not affected by the plasma, that is, all return currents are outside the particle bunch. Return currents in the region of the bunch counteract the focusing magnetic field and reduce the focusing strength to K_{rc} which is approximately given by Whittum et al. 1990; Chen et al. 1998.

---

[1]See eqn. 2.1 and 2.2 noting a typographic error in eqn. 2.2: $n_p \to n_b$

$$K_{rc} = \frac{K}{1 + (k_p \sigma_\perp)^2} \tag{5.13}$$

$$= \frac{1}{2\gamma} \cdot \frac{k_b^2}{1 + k_p^2 \sigma_\perp^2} \tag{5.14}$$

using the relation $k_b^2 = 4\pi r_e n_b$.

In order to compare the focusing strength K from this model with the simulation data (figure 5.3), a simple geometric consideration links it with the force calculated in the simulation. A particle traveling through the transverse field at a transverse distance y is collecting transverse momentum $p_\perp = \int F_\perp \, dt$ and the angle of its motion is determined by the ratio of transverse to longitudinal momenta $\alpha = p_\perp / p_\parallel$, which is also the ratio of transverse distance y to focal length f: $\alpha = d/f$. Combining this yields

$$\alpha = \frac{p_\perp}{p_\parallel} = \frac{1}{cp_\parallel} \int F \, ds \tag{5.15}$$

$$= \frac{y}{f} = y \int K \, ds \tag{5.16}$$

$$\Rightarrow K = \frac{F}{cyp_\parallel} = \frac{F}{y\gamma mc^2} \tag{5.17}$$

As a numerical example should serve: transverse distance $y = 1\,\mu\text{m}$, $\gamma = 200$, $F = 1\,\text{pN}$ leads to $K = 0.061 \cdot 10^6\,1/\text{m}^2$. The values from figure 5.3 are showing a focusing force of $F \approx 120\,\text{pN}$ in a distance of $y = 2\,\mu\text{m}$ yielding $K \approx 3.6 \cdot 10^6\,1/\text{m}^2$. In comparison equation 5.14 evaluates for the same parameters to $K_{rc} = 4 \cdot 10^6\,1/\text{m}^2$, which is in good agreement. Particularly the fact, that the simulated bunch has longitudinal Gaussian shape, while the model assumes an infinitely long beam is most likely to account for the deviation.

Scaling of the focusing strength (longitudinal direction)

LWFA accelerators typically have short and dense electron bunches compared to RF accelerators. Lundh et al. 2011 published a measurement of the bunch duration of 1.4 to $1.8\,\text{fs} \approx 0.5\,\mu\text{m}$ (RMS); Buck et al. 2011 measured $5.8 \pm 2\,\text{fs} \approx 1.7 \pm 0.6\,\mu\text{m}$ (FWHM). Those bunches have therefore a very different aspect ratio compared to an RF accelerated electron beam. After propagation of only a few mm their shape may safely be assumed to be "pancake"-like rather than "cigar"-like.

The description of the passive plasma lensing for an LWFA electron bunch therefore requires also the scaling of the effect depending on the longitudinal size of the bunch.
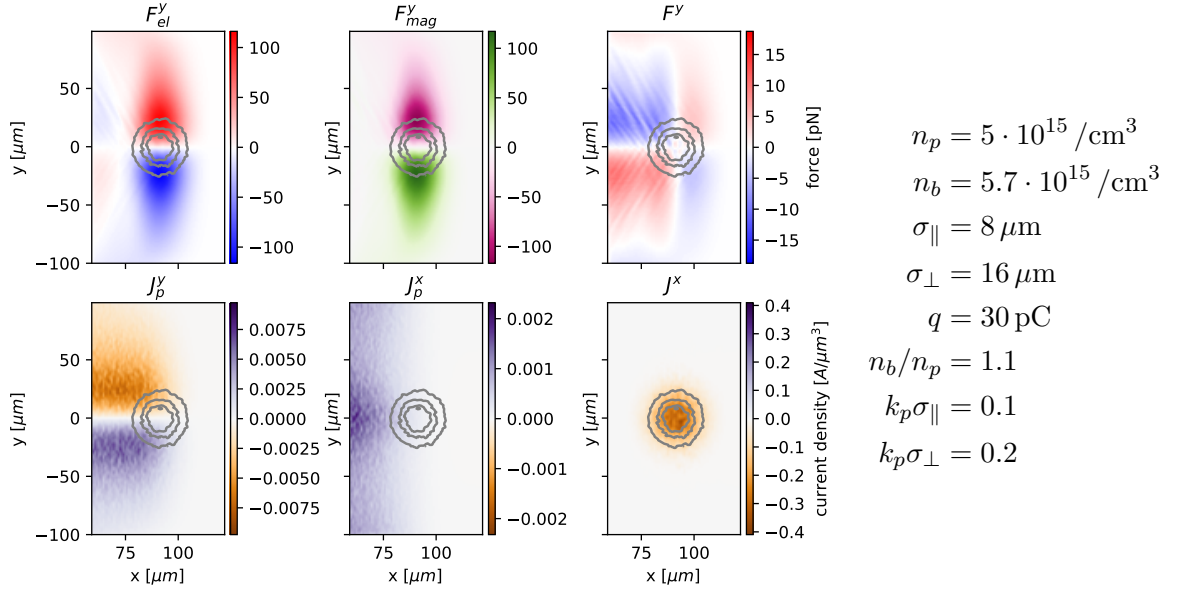
Figure 5.4: *The short and narrow bunch: The plasma response takes place on length scales much longer than the extent of the bunch, which is visible in J_p^y and J_p^x. Therefore the plasma ineffectively shields the electric fields and the final plasma focusing almost vanishes. Strictly $n_b/n_p = 1.1$ is not within the over-dense regime since the plasma density is modulated by only $\sim 1 \cdot 10^{15}\,/\mathrm{cm}^3$ due to the slow plasma response.*

Unfortunately such a scaling is not available in the literature to the knowledge of the author. As the entire evolution of the fields becomes more complicated when at least on of the parameters $k_p\sigma_\parallel$ or $k_p\sigma_\perp$ approach unity, 3D PIC simulation of those regimes will be presented to give a qualitative understanding of the plasma response and assess for which parameter ranges plasma lensing may be possible.

5.2.1 Qualitative description of the plasma response

This section will show selected simulations to qualitatively describe longitudinal effects of the plasma wake and their influence on the propagating electron beam.

We will start from the case of ideal plasma lensing (figure 5.3). This long and narrow bunch becomes short and narrow, when its length is reduced, as seen in figure 5.4. Since the plasma response occurs on the scale of the plasma wavelength the plasma responds after the bunch has already passed and therefore fails to shield both, the electric and the magnetic field of the particle bunch. Hence, the magnetic and electric forces of the bunch cancel (as in the vacuum case, equation 5.6 with $\beta \to 1$) and the net focusing effect on the bunch almost vanishes. The currents induced in the plasma are shifted behind the actual bunch in the simulations.
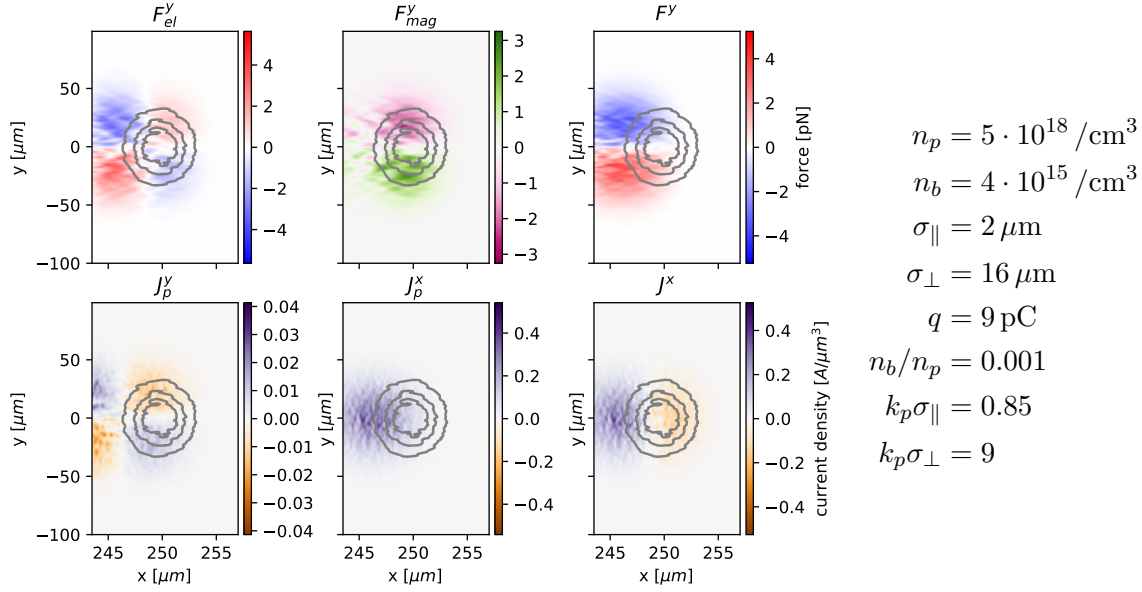
Figure 5.5: *A wide and short bunch: While the return currents are transversely matched to the bunch, they lag behind the actual bunch leading to a residual focusing magnetic field. As the plasma response lags behind the electron bunch, the electric field of the bunch is overcompensated in its tail and behind it leading to a focusing electric field.*

However, there are fields created behind the bunch which could be used to focus a second particle bunch. This principle has been proposed by Chen et al. 1987. It is strictly not a passive plasma lens scenario since the focusing fields for the second bunch are created by the preceding bunch.

As soon as one of the $k_p\sigma_\parallel$ or $k_p\sigma_\perp$ parameters approach unity the situation becomes more complicated. The next example shall be the one depicted in figure 5.5: The bunch is wide ($k_p\sigma_\perp = 9$), but longitudinally almost matched ($k_p\sigma_\parallel = 0.85$). As the bunch is wide, the plasma can match the current profile transversely to the shape of the bunch. The longitudinal plasma response is shifted late, which is behind the bunch. This is most visible in J_p^x. Consequently the bunch current is not fully compensated a the front of the bunch, but it is overcompensated at the bunch's tail and behind (J^x). Due to this delayed current, it can only compensate a part of the magnetic field such that some focusing magnetic field remains.

The delayed plasma response also leads to a new observation: As the shielding of the electric field is delayed, the electric field of the bunch is overcompensated in the tail of the bunch and thereafter. Accordingly there is a focusing electric field starting from the tail of the bunch (F_{el}^y). In total this leads to a focusing magnetic field inside the bunch and a focusing electric field in its tail and behind.
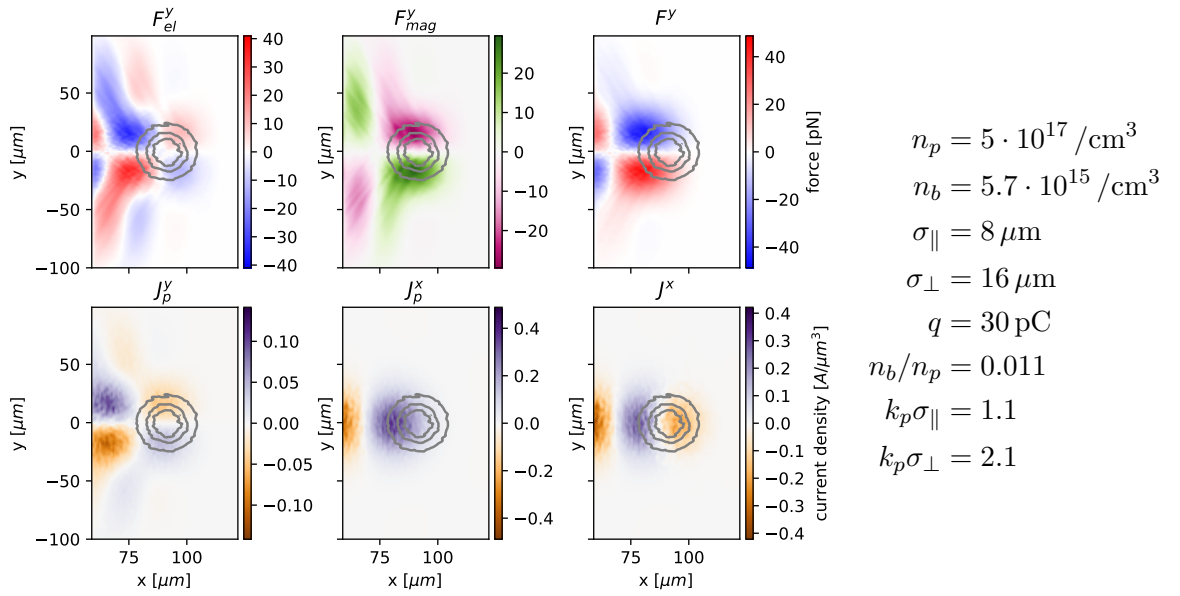
Figure 5.6: *This bunch is matched in the parallel direction to the plasma density, while it is a factor two larger than the matched spot size transversely. The changes of the shape of the electric and magnetic field it creates are strongly visible. Also a strong focusing remains, since the bunch is slightly longer than the matched spot size and the bunch's tail is extending into the focusing region the bunch's head is creating. In this scenario, the focusing is actually dominated by focusing electric force unlike the typical description of passive plasma lensing effect.*

The figure shows panels labeled F^y_{el}, F^y_{mag}, F^y (top row) and J^y_p, J^x_p, J^x (bottom row), with parameters:

$$n_p = 1 \cdot 10^{17} \,/\mathrm{cm}^3$$
$$n_b = 1.5 \cdot 10^{15} \,/\mathrm{cm}^3$$
$$\sigma_\parallel = 8 \,\mu\mathrm{m}$$
$$\sigma_\perp = 8 \,\mu\mathrm{m}$$
$$q = 6 \,\mathrm{pC}$$
$$n_b/n_p = 0.015$$
$$k_p\sigma_\parallel = 0.5$$
$$k_p\sigma_\perp = 0.5$$

Figure 5.7: *In this scenario the bunch size is almost matched in both directions. Notably, the transverse currents are only a factor 2.5 smaller than the longitudinal ones. Due to the very short bunch, only the onset of the plasma response can act back on the electron bunch to create a focusing effect. A longer bunch would be therefore beneficial to the focusing.*

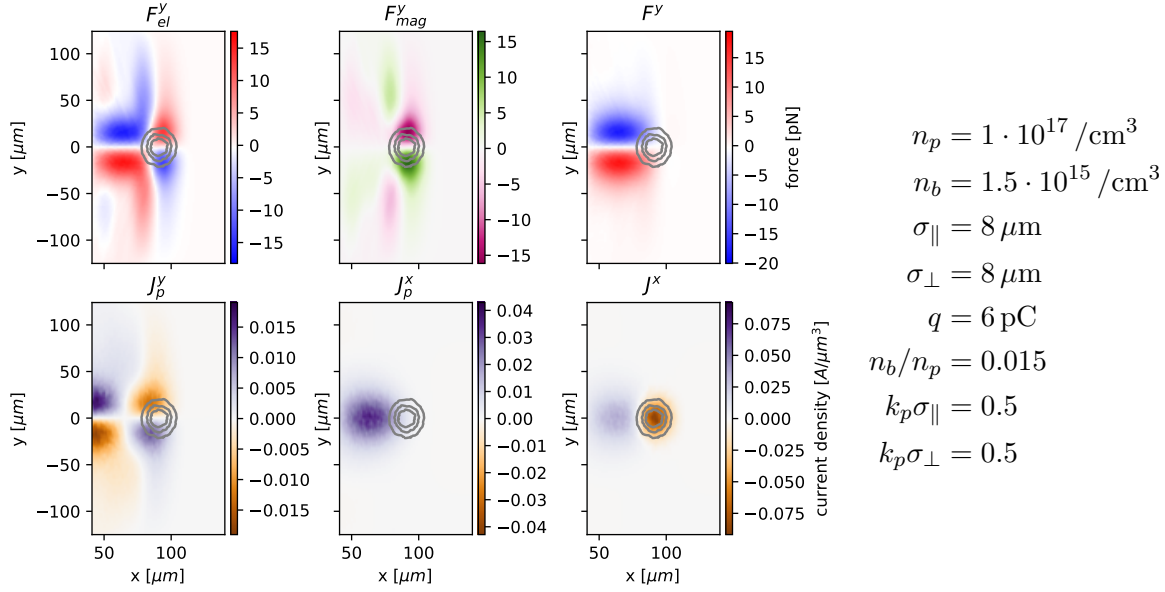Reducing $k_p\sigma_\perp$ further (figure 5.6: $k_p\sigma_\parallel = 1.1$, $k_p\sigma_\perp = 2.1$) leads to a very similar scenario with a much stronger influence of the transverse currents, since the return currents (J^x_p) are partially located radially outside of bunch as in the ideal passive plasma lensing scenario (figure 5.3). Also the focusing electric field increases strongly in this simulation. The simulation shows qualitatively the same behavior as figure 5.5, but the transverse currents within the plasma J^y_p have strongly increased compared to the longitudinal ones. Also, a deformation of F^y_{el} is visible. It is worth noting, that these parameters ($k_p\sigma_\parallel = 1.1$, $k_p\sigma_\perp = 2.1$) are clearly outside the typical passive plasma lensing scenario (long and narrow bunch). However, the simulation still shows a significant focusing effect for such short bunches.

A similar example is presented in figure 5.7, where $k_p\sigma_\parallel = k_p\sigma_\perp = 1/2$ and the deformation of the electric field is clearly visible. As the bunch gets shorter the focusing region is shifting behind the bunch and the focusing effect on the bunch reduces strongly. Compared with the scenario before, the plasma lensing is sensitive to the exact bunch parameters in this regime.

The presented simulations show the passive plasma lens effect for different parameters. When applicable, the model and the simulations predict a very similar focusing force. Most importantly, the simulations show a considerable focusing effect, even for parameters, which deviate strongly from the optimal plasma lensing scenario. Such a case is,

for example, $k_p\sigma_\parallel = 1.1$. It can also be seen that a comparably small change of the parameters in this regime can have a strong influence on the focusing effect.

5.3 Underdense regime ($n_p \ll n_b$)

A very different regime is approached when $n_p \ll n_b$. In this so called *overdense* regime the bunch's density is much larger than the background plasma density. Consequently the bunch is able to drive a strong plasma wake or even deplete the electron density, as displayed in figure 5.8. In this case the electron depleted region creates an electric field, which is focusing the bunch and, moreover, may lead to reduced transverse aberrations, because the electric field increases linearly with the radius [Su et al. 1990]. In addition due to the depletion of the electron density in the region of the bunch all return currents must be located outside of the bunch, which is clearly visible in J_p^x of figure 5.8. Therefore the transverse bunch size limit is not as strict as in the over-dense regime (equation 5.13). However a wide bunch may require a larger bunch density n_b in order to reach the electron blow out in the plasma compared to a narrow bunch.

Barov et al. 1998 has experimentally demonstrated the underdense passive plasma lens. $n_b/n_p = 2$ was expected for a 25 ps long electron bunch, carrying 14 nC of charge. While focusing of the plasma has been clearly observed in this experiment, depletion of the electron density has not. In another example a 15 MeV electron bunch of 18 nC was focused by a plasma with a focal length of only $f = 1.7$ cm reducing the area of the beam spot by a factor of 23 (Thompson et al. 2010). They were in the onset of the underdense regime with $n_b/n_p \approx 0.5$. Their measurements also show, that the the underdense regime can have very low spherical aberrations at a high focusing strength.

As the particle bunch is driving a plasma wake, this regime is not only of interest for focusing, but moreover for particle acceleration (PWFA). Due to the strong plasma wake, the particles in the tail of the plasma wake experience a strong accelerating force. Therefore changes of particle beam energy as well as transverse beam oscillations have been measured [Hogan et al. 2000]. A few years later PWFA driven energy doubling of a small fraction of the actual electron bunch has been reported [Blumenfeld et al. 2007].
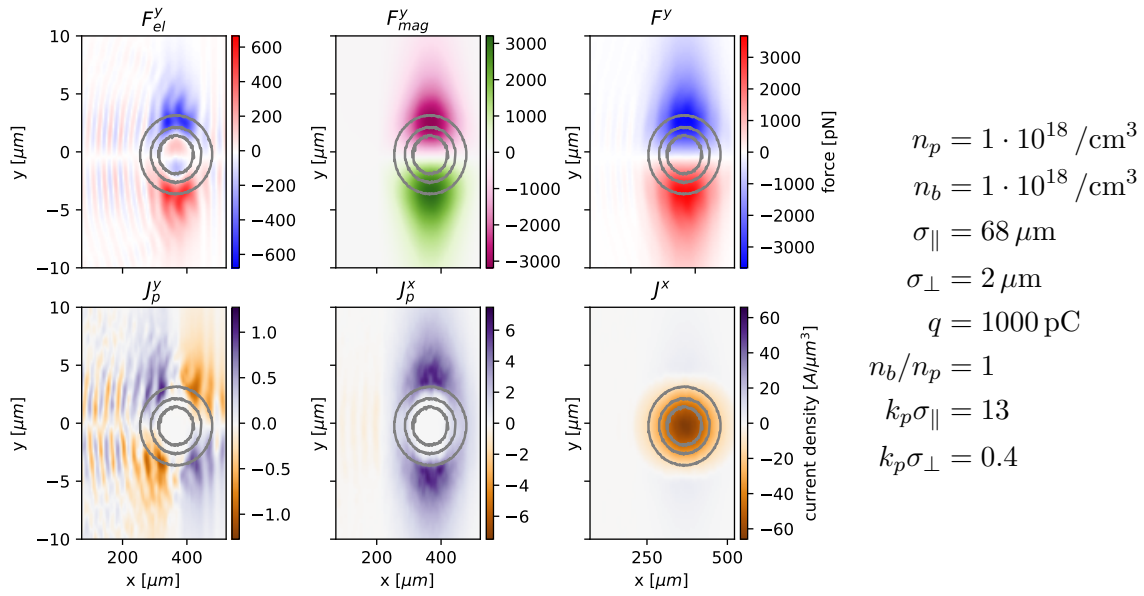
Figure 5.8: *Although $n_b/n_p = 1$ in this simulation, it can already be considered as the underdense case, since the electron bunch depletes the electron density of the plasma entirely. Even without a density plot this is clearly visible in the shape of the return current J_p^x, which is forced around the volume of the bunch. The mass of the bunch particles was increased in the simulation, in order to prevent them from being deviated due to the strong focusing forces. Therefore only the plasma response can be investigated while the particle bunch stays unaffected.*

6 Passive plasma lensing using an ultra-short electron bunch

This chapter presents the results of the plasma lensing experiment, performed at the JETI 40 laser system at the Institute for Optics and Quantum Electronics of the Friedrich-Schiller University Jena. Due to the use of the gas cell, the beam shape was much better controlled compared to the gas jet (Chapter 4). This improvement made the passive plasma lensing experiment possible.

It is the first demonstration of passive plasma lensing of a laser wake field accelerated electron bunch. Parts of the content of this chapter have been published in Kuschel et al. 2016.

6.1 Experimental setup

The setup of the passive plasma lensing experiment is similar to the one used for the gas cell experiment, while it is modified to support a second plasma stage after the first acceleration stage (figure 6.1). There was a tunable gap length L_{gap} between the gas cell (acceleration) and the gas jet (lensing). The usage of the gas cell was crucial to the experiment, as the stable beam profiles allowed the measurement of small changes of the electron beam divergence. Using the gas jet would have obscured the focusing effect by random electron beam shape fluctuations.

For the acceleration stage a modified version of the gas cell has been used to support smaller distances between the exit of the gas cell and the beginning of the second plasma stage, as shown in figure 6.2. The laser pulse enters the gas cell, where the LWFA takes place over a distance of $2\,\mathrm{mm}$. The optimal density for acceleration has been measured by interferometry to be $n_e = (1.0 \pm 0.25) \times 10^{19}\,/\mathrm{cm}^3$, using a mixture of 95% He and 5% N_2. The conditions in the gas cell are the same as reported in section 4.4: The electrons are ionization-injected (section 3.2.3) close to the injection threshold which constrains the injection process to the first bucket and the electron beam to a single bunch.
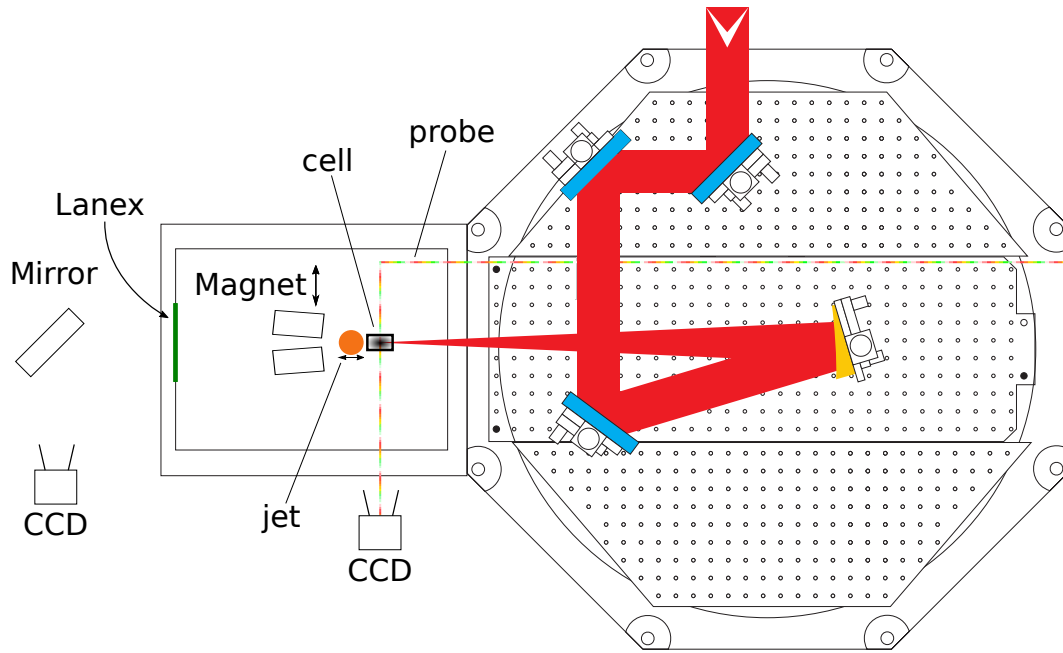
Figure 6.1: *The experimental setup used for the measurements of the plasma lens effect. The laser enters the gas cell where it accelerates electrons. Theses electrons are then passed through a second plasma provided by a gas jet. See figure 6.2 for a zoomed view into this part of the setup. The electrons are finally detected on a scintillating screen. Depending on the position of the motorized magnet, the scintillation screen provides pointing or spectral information.*
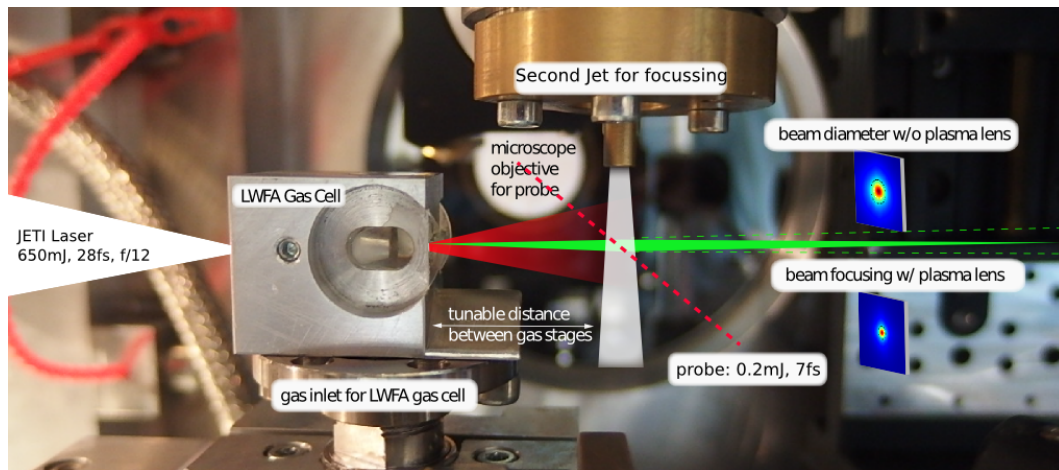
Figure 6.2: *A close image of the modified gas cell and the gas jet for the plasma lensing stage. The jet was motorized to tune the distance L_g between the exit of the gas cell and the beginning of the jet plasma in the range between $8\,\text{mm}$ and $24\,\text{mm}$. The residual laser pulse is still strong enough to ionize the Hydrogen gas in the jet (Helium could not be ionized) to provide the plasma for the passive plasma lensing. The beam's profiles were measured on a scintillation screen $57\,\text{cm}$ downstream.*

The laser pulse in the gas jet

After the first stage (acceleration), the residual laser pulse exits the gas cell and diverges strongly. Assuming it was guided with a matched spot size (equation 3.53), the exit divergence should match the focusing, that is $\sim$f/12 and consequently $\theta_{div} \approx 80$ mrad. In the experiment the residual laser pulse behind the gas cell was not sufficiently intense to ionize Helium in the gas jet, even for the lowest gap length of $L_g = 8.75$ mm. That is why the gas jet has been operated with H_2 during the entire experiment. It has been observed by interferometry, that H_2 was still ionized by the laser at $L_g = 24$ mm. This observation sets tight limits on the intensity the laser pulse can have inside the second plasma stage. Using the Ammonsov-Delon-Krainov (ADK) ionization rates [Ammosov et al. 1986] and assuming an ionization rate of 0.5 /fs, it is found that the laser's intensity has to be larger $I > 2.25 \times 10^{14}$ W/cm^2 at $L_g = 24$ mm, but smaller than $I < 1.75 \times 10^{15}$ W/cm^2 at $L_g = 8.75$ mm. These are reasonable values as the expected divergence leads to an intensity decrease compared to the gas cell exit of $\sim 1/2000$ (at $L_g = 8.75$ mm) and $\sim 1/13000$ (at $L_g = 24$ mm). Assuming a transmission of $\sim 30\%$ the calculation matches the intensities approximated by the ADK model. However, a temporal compression of the laser pulse due to the plasma would allow for a lower transmission. Additionally, that the plasma gradient at the end of the gas cell may reduce the divergence of the laser, which in general leaves a wider margin for the transmission.

It is important to note, that the laser pulse is unable to drive a significant plasma wake in gas jet. For the shortest distance of $L_g = 8.75$ mm the upper bound on the intensity corresponds to $a_0 < 0.03$ which means that the strongest plasma density perturbation driven by a single pulse is $\frac{\Delta n}{n_0} < 10^{-3}$, assuming optimal pulse shape. However, the laser's pulse shape is far from optimal: Due to its strong divergence the intensity distribution is almost flat which impairs its ability to drive a plasma wake significantly. Also, the flat intensity distribution does not allow any transverse fields due to symmetry, which is why the plasma wake cannot have any focusing fields. The fact, that the laser in this experiment is unable to drive a plasma wake with transverse fields, is the significant difference between this experiment and the active plasma lens reported in Nature Communications by [Thaury et al. 2015]. This experiment probes the passive plasma lensing effect.

6.1.1 Electron spectrometer

During the experiment not only beam profiles, but also electron spectra have been recorded. In order to perform a spectrally resolved divergence measurement, the divergence of the electron beam in the non-dispersive direction needs to be conserved. This requires an analysis of the fringe fields of the magnets and the yoke, which can

cause a residual curvature of the magnetic field lines. For this purpose the software package RADIA[1], developed at the ESRF has been used. The yoke was optimized to minimize deviations in the non-dispersive direction while maximizing the angular acceptance to 100×100 mrad and keeping the angular error < 1.5 mrad within that window for an 100 MeV electron beam.

The final yoke used throughout the experiments is shown in figure 6.3. The magnets (red) are $40 \times 40 \times 20$ mm each. The maximum field strength measured at the manufactured yoke and the design value have deviated by 1% (550 mT to 545 mT). The deviation of measurement to calculation at all other points around the yoke has been within the error margin of the hall probe. Electrons with $E = 200$ MeV will be deviated by 25 mrad when passing though the central magnetic field of the yoke, leading to $\sim 20\%$ energy resolution, when assuming 5 mrad pointing stability of the beam. Note, that this is a worst case scenario, as the pointing stability with gas cell is ~ 2.5 mrad and the energies measured typically range up to ~ 140 MeV only.

The yoke was light enough to place it on a vertically mounted motorized linear stage to drive it upwards out of the beam path. Therefore the same scintillating screen could be used for the observation of the pointing/beam profile or the spectrum of the electron beam. This resulted in a very compact setup.

---

[1] `http://www.esrf.eu/Accelerators/Groups/InsertionDevices/Software/Radia`
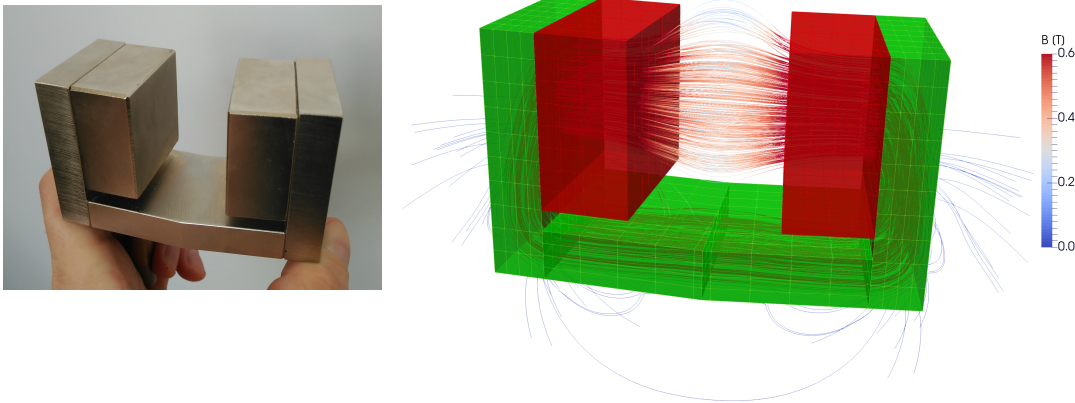
Figure 6.3: *The magnet yoke designed and build for the plasma lens experiment. The fields were calculated using the software package RADIA and the yoke was optimized to maximize angular acceptance while keeping the non-dispersive direction unchanged.*
Left: A picture of the final yoke.
Right: The computer model with the calculated magnetic field lines. The red boxes are the permanent magnets (N52), while the green volume is the yoke material (ST37).

6.2 Experimental demonstration of passive plasma lensing

Beam profiles

Electron beam profiles have been recorded at the scintillating screen, mounted $57\,\mathrm{cm}$ downstream from the laser's vacuum focus position. The focusing plasma provided an electron density of $n_e = 1.6 \cdot 10^{19}\,/\mathrm{cm}^3$ over a length of $2\,\mathrm{mm}$. The gap length between gas cell and gas jet was set to $8.75\,\mathrm{mm}$. The individual beam profiles have been aligned to their individual center position and averaged to assemble figure 6.4a,b. Focusing is clearly visible as a reduction of beam size on screen as well as an increase of the electron flux, when the passive plasma lens is in operation. In order to quantify the reduction of beam size, a 2D Gaussian distribution has been fitted to the data and its covariance matrix Σ has been calculated. As in section 4.6, the black ellipse's half axis lengths are chosen to match the square root of the eigenvalues of the covariance matrix. The area of the black ellipse is therefore a good measure for the solid angle, the electrons are emitted into. This solid angle Ω has decreased from $16\,\mu\mathrm{sr}$ to $6\,\mu\mathrm{sr}$ when the passive plasma lensing was in operation.

Figure 6.4c,d show the corresponding pictures from a 3D PIC simulation with EPOCH3D v4.3.7. A similar reduction of the beam size as in the experiment is reproduced by the simulation. The simulation does not include a laser pulse and the focusing effect is only driven by passive plasma lensing. The parameters of the simulations were matched to the experimental conditions. The simulation box size was $14 \times 200 \times 200\,\mu\text{m}$ $(0.25\,\mu\text{m}$ resolution). The electron bunch was chosen to be of gaussian shape with $\sigma_x = \sigma_\| = 2\,\mu\text{m}$ and $\sigma_{y,z} = \sigma_\perp = 5\,\mu\text{m}$ carrying a total charge of $q = 9\,\text{pC}$ with γ factor of $\gamma = 200$. The initial divergence was set by introducing a transverse temperature to match the measured divergence ($16\,\mu\text{sr}$ corresponding to $\Delta\theta = 2.3\,\text{mrad}$). These bunch parameters correspond to a normalized emittance of $\varepsilon_N = 1.9\,\text{mm\,mrad}$ (see section A.1), which is similar to already reported values in the literature, for example $2.3\pi\,\text{mm\,mrad}$ has been reported by Sears et al. 2010 or $2.2\pi\,\text{mm\,mrad}$ up to $1.1\pi\,\text{mm\,mrad}$ at best by Brunetti et al. 2010.

Due to the divergence of the electron bunch, its size increases while passing through the gap ($L_g = 8.75\,\text{mm}$) between acceleration and focusing stage. The transverse size of the electron bunch is estimated to be $\sigma_\perp^{\text{at lens}} \approx 21\,\mu\text{m}$ when entering the plasma lensing stage. The lensing stage finally reduced the beam's divergence to $1.4\,\text{mrad}$. The emittance limit of the divergence, that can be possibly achieved by a perfect lens at that position is given by $\sigma_\theta^{\text{min}} = \frac{\varepsilon_N}{\gamma\sigma_\perp^{\text{at lens}}} = 0.6\,\text{mrad}$. The measured focusing effect is therefore only a factor 2.3 smaller compared to the emittance limited theoretical maximum for a monoenergetic electron bunch. The electron bunch used here is clearly far away from being monoenergetic (see figure 6.7 for electron spectra). A reason for the difference to the theoretical optimal focusing may by chromatic aberration of the passive plasma lens. The experiment itself is clearly in the overdense regime and the lensing parameters are estimated as $k_p\sigma_\| = 1.5$ and $k_p\sigma_\perp = 10$. This scenario is therefore similar to the simulation in figure 5.5. The simulation clearly shows, that the focusing strength is maximal at the tail of the bunch, while it almost vanishes at its head. This longitudinally varying focusing may be another reason why the best focusing is deviating from its theoretical optimum. The fact, that the simulation (figure 6.4c,d) shows similar focusing as the experiment suggests, that the longitudinally varying focusing strength may be the dominant factor to the non-optimal focal spot.

A scaling of the solid angle Ω with respect to the plasma density in the focusing stage has been measured and is shown in figure 6.5. The error bars are similar for every data point but have been specifically determined only for reference shots, i.e. the lensing stage inoperative. While the plasma density of the plasma lens is increasing, the solid angle of the electrons is continuously decreasing. At the same time the maximal electron flux on the scintillation screen increases strongly as soon as the lens becomes operative but then stays at an almost constant level. Since a change of the plasma density implies a change
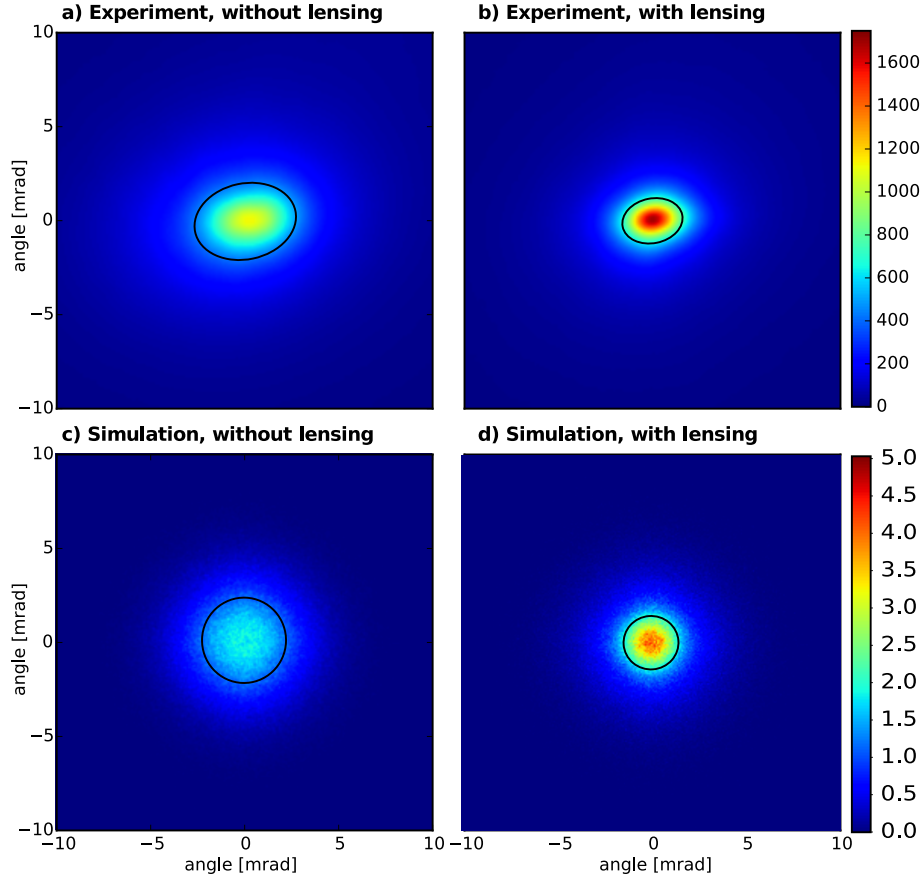
Figure 6.4: *Beam profiles as seen on the scintillation screen: Inset a) shows the center aligned and averaged beam profile of 227 reference shots with the acceleration stage only. Inset b) shows the center aligned and averaged beam profile of 175 shots with the focusing stage using an electron density of $1.6 \cdot 10^{19} \text{cm}^{-3}$ and a separation of $L_g = 8.75\,mm$. In both pictures the black ellipse encloses the standard deviation of a 2D gaussian fit function to the beam profile. The black ellipse reduces its area from $16\,\mu sr$ (left) to $6\,\mu sr$ (right) as the focusing stage is turned on.*
c) and d) show the corresponding data from the EPOCH3D Simulation: The bunch's initial divergence is set up to match the experimentally measured divergence of $16\,\mu sr$ (c). The encircled solid angle reduces to $7.3\,\mu sr$ after propagation through $2.5\,mm$ plasma with a density of $n_p = 1 \cdot 10^{19}/cm^3$ with $0.5\,mm$ linear ramps on both sides. [Kuschel et al. 2016]

Figure 6.5: *Solid angle and maximum electron flux depending on the density of the focusing plasma: The solid angle (left axis, blue) of the electron beam decreases as the plasma density increases. The gap length was kept constant at $L_g = 8.75\,mm$ for all measurements. Each point is calculated from a center-aligned and averaged 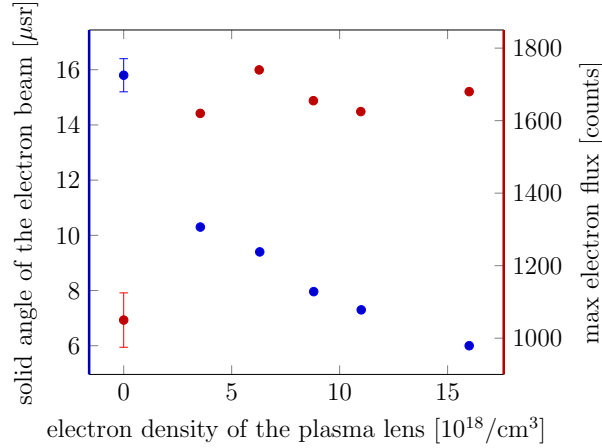(see text) beam profile over 150 to 250 shots. The reference with the lensing stage turned off (density = 0) has been measured in the beginning, middle and end of the scan. The error bars indicate the standard deviation ($\pm 1\sigma$) of these measurements. The error is similar for all measurements. The density measurements were taken using a wavefront sensor, resulting in an error of $\pm 0.5 \cdot 10^{19}/cm^3$. The red points (right axis) shows the peak electron flux on the scintillation screen. [Kuschel et al. 2016]*

of the focusing force, this may indicate that different electron energies are focused onto the screen, while lower energies are over-focused and higher energies experience only little focusing. The spectrally resolved data will show, that this is actually the case (see figures 6.7, 6.8).

Single shot analysis

In addition to the averaged beam profiles, also a single shot analysis has been carried out to confirm the results. The single shot data is shown in figure 6.6. For every laser shot a Gaussian profile has been fitted to the recorded beam profile to retrieve the solid angle covered, the maximum amplitude of the fit and the charge within the 1σ-ellipse. Each dot represents one laser shot, whereas the red arrow indicates the result of the analysis of the averaged pictures (figure 6.4). The two point clouds (with and without plasma lens) have clearly moved in both pictures, caused by the passive plasma lensing effect. The movement of the point clounds corresponds to the movement of the averaged beam profiles, as clearly seen in the picture, thus the analysis of the averaged data and the single shot analysis are well matched. While the solid angle decreases, the charge within the 1σ-ellipse decreases to about 75%. At the same time the Gaussian fit amplitude increases by a factor 1.65 indicating an increased electron fluence on the scintillating

screen. It can also be seen that the point clouds occupy areas of similar size with and without the passive plasma lens. Therefore it is worth noting, that the plasma lens does not amplify variations of the electron beam and is stable in comparison to the stability of the laser driven acceleration process.

Spectral analysis

In order to characterize the passive plasma lens effect spectrally resolved, the magnet yoke, as described in section 6.1.1, was inserted into the beam path (figure 6.1). This turns the scintillating screen into the spectrometer screen, maintaining the divergence of the beam in the non-dispersive direction. The magnet was mounted such that it could be moved without braking vacuum. Therefore the electron beam axis is well known from the measurements of the pointing stability. The energy resolution is consequently only impaired by shot-to-shot fluctuations, but no global offset.

For the spectral analysis multiple spectra have been averaged. Similar to the beam profiles the averaging was performed by first aligning the spectra in the non-dispersive direction to ensure their final width is dominated by the electron's divergence rather than their pointing stability.

The data is shown in figure 6.7. The averaged data is presented on the left, while the right part is the exact same visualization of a single shot only. Three different scenarios are displayed: The divergence resolved spectrum without the plasma lens and the plasma lens operated at at a gap length $L_g = 8\,\text{mm}$ and $L_g = 24\,\text{mm}$. A low energy region (40-42 MeV) and a high energy region (90-100 MeV) are emphasized and their individual profiles are compared in the upper and the lower panel of the figure. A clear spectral dependence of the passive plasma lens can be identified: At $L_g = 8\,\text{mm}$ the high energy part of the spectrum has reduced its divergence and increased the spectral electron flux. At $L_g = 24\,\text{mm}$ the low energy part of the spectrum has reduced its divergence and increased the spectral electron flux. This is most visible in the "low energy lineout" panel.

The plasma lensing experiment has been carried out at various gap lengths to measure the transition from the low energy to the high energy focusing. Divergence and intensity change are summarized in figure 6.8. The color scales in both panels indicates the contrast between the value with plasma lens and the reference without it. The contrast C between two values a and b is defined to be

$$C = \frac{a - b}{a + b} \tag{6.1}$$
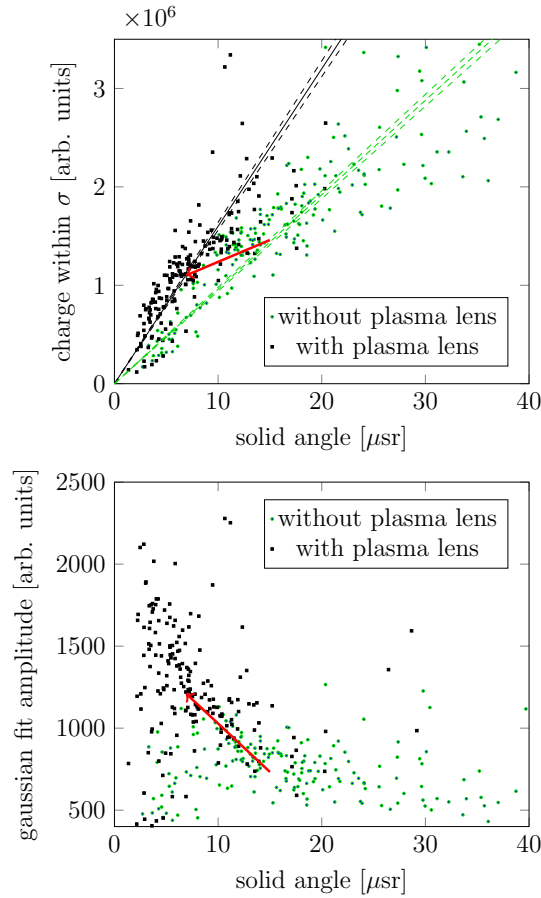
Figure 6.6: *Single shot data analysis of the plasma lensing effect: Each dot represents a single laser shot without the plasma lens (green) or with the plasma lens in operation (black). The shift of the point clouds is clearly visible. The averaged data sets are shown in figure 6.4a (green, no plasma lens) and 6.4b (black, plasma lens density $1.6 \cdot 10^{19}/cm^3$). The red arrows therefore indicate the values obtained from the averaged analysis in fig. 6.4. The gap length was kept constant at $L_g = 8.75\,mm$*

Top: As the average solid angle reduces from $16\,\mu sr$ to $6.8\,\mu sr$, the charge in the beam's central region drops to 75%. A linear fit reveals the increase of the beam's fluence from $(96 \pm 2) \cdot 10^3$ [a.u.] to $(160 \pm 4) \cdot 10^3$ [a.u.] with the lensing stage enabled. The dashed lines show the standard deviation of the fit.

Bottom: Together with the reduction of the solid angle an increase in the amplitude of the 2D Gaussian fit by a factor of 1.65 is observed. [Kuschel et al. 2016]
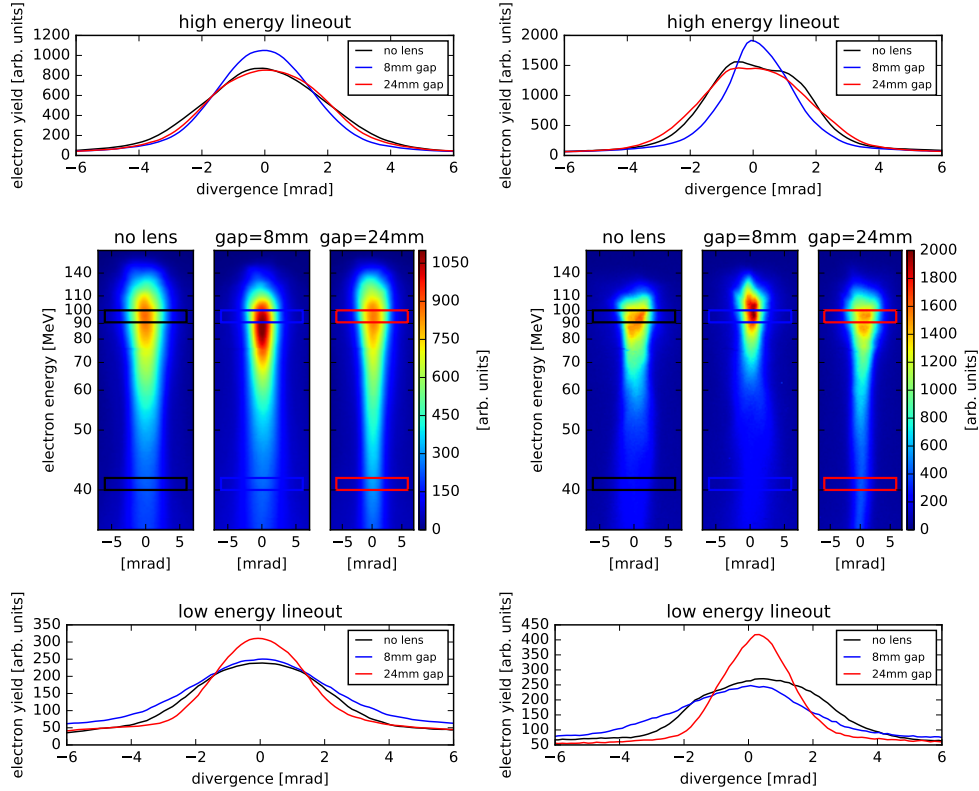
Figure 6.7: *Spectral dependence of the plasma lens:*
Left: Each of the three spectra is aligned and averaged over 40-50 shots. The spectra show a comparison between the divergence of the electrons without (left) and with plasma lens (middle and right).
Right: Identical analysis for the same cases depicted on the left, but only a single shot is shown for each scenario. The same focusing behavior can be observed as for the averaged spectra.
The plasma lens uses an electron density of $(1.2 \pm 0.8) \times 10^{19} / cm^3$. Profiles of the high energy part (90-100 MeV) and the low energy part (40-42 MeV) are shown on top and bottom. It is shown that the high energy electrons are focused at 8 mm gap length (blue), whereas the low energetic electrons are focused at 24 mm gap length (red). [Kuschel et al. 2016]

and therefore a positive contrast in the divergence change indicates an increase of divergence relative to the reference value without the plasma lens. The lower panel of figure 6.8 shows the change of maximum intensity on the scintillation screen. For $|C| \ll 1$, note that the relative change $a/b \approx 2C$. It can be seen, that he divergence angle θ is reduced up to a factor 1.4 in the data shown.

As a decrease of divergence (focusing, brown) should increase the maximum intensity on the scintillation screen. For better visualization the color scale of the intensity change is reversed. A correlation between both plots is clearly visible: A reduction of divergence correlates to an increase of intensity in the regions of low energy and large gap length as well as high energy and small gap length. It is very important to cross check, that divergence reduction and intensity increase correlate in order to validate the measured data. Otherwise a reduced angular acceptance of the passive plasma lens could cause an apparent lensing effect.

A pronounced feature is visible at low gap lengths: The plasma lens is acting rather strong at that gap length and focusing the high energy electrons. The low energy electrons increase their divergence while their intensity on the screen reduces. Therefore the lens is acting strong enough to overfocus lower energy electrons, meaning their focus is located between the passive plasma lens and the scintillating screen.

Estimate of plasma lens parameters

From the spectral measurement (6.8) some basic parameters of the passive plasma lens can be estimated. For the smallest gap length $L_{\text{gap}} = 8\,\text{mm}$ the minimum beam diameter on screen is located around $E = (90 \pm 10)\,\text{MeV}$ ($\gamma_{\text{min}} = 180 \pm 20$). As the divergence of the electrons increases to higher as well as lower energies, the focus of this particular energy must be located on the scintillating screen. This corresponds to a focal length of the plasma lens equal to the gap length $f = L_{\text{gap}} = 8\,\text{mm}$. Assuming the plasma lens can be approximated as a thin lens, the focusin strength is given by $K = 1/(f \cdot s)$, with $s = 2\,\text{mm}$, the length of the plasma lens. It evaluates to $K = 62 \cdot 10^3\,/\text{m}^2$. For a better comparison between the different gap lengths the focusing strength has also been normalized to a beam with $\gamma = 160$, yielding $K_{\gamma=160} = 70 \cdot 10^3\,/\text{m}^2$. The results of an identical estimation for $L_{\text{gap}} = 12\,\text{mm}$ and $L_{\text{gap}} = 24\,\text{mm}$ are summed up in table 6.1. Since the maximum focused energy is not visible for $L_{\text{gap}} = 24\,\text{mm}$ only an upper bound of the focusing strength can be obtained. These values will be used as initial data for the modeling of the beam in the following section.
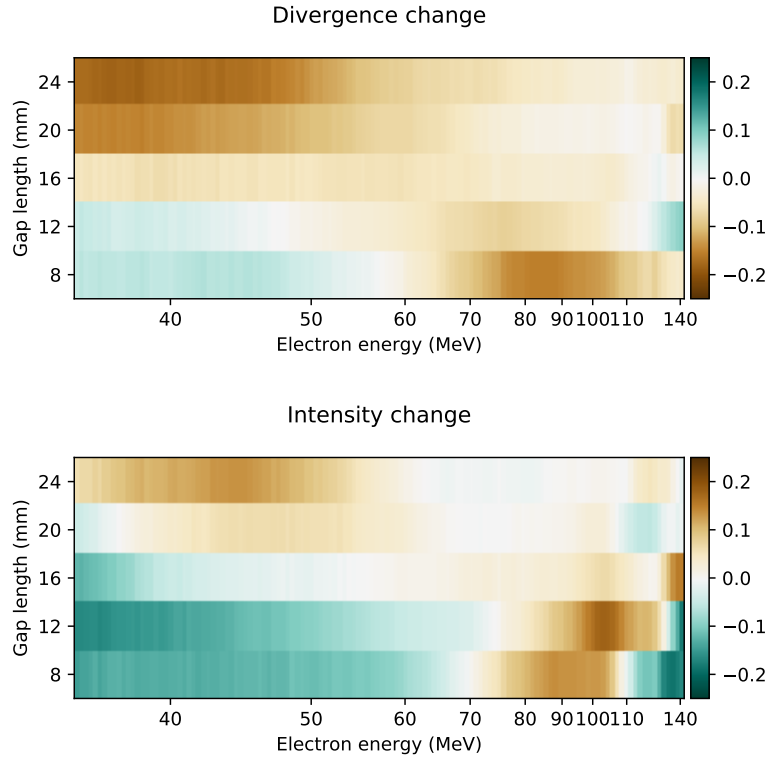
Figure 6.8: *The spectrally resolved divergence and intensity change induced by the passive plasma lens for five different gap lengths: The color maps indicate the contrast C (see text) between the the value with plasma lens and the reference value without it, which is the divergence θ for the upper panel and the maximum electron flux on the scintillation screen for the lower panel. A correlation between measured intensity and divergence is clearly visible: The intensity of the electron beam increases in regions, where the divergence decreases (focusing, brown) and vice versa.*
Furthermore in the low energy, small gap length region, over-focusing of the electron beam can be observed, as the divergence increases and the intensity decreases, while higher electron energies are being focused.

f [mm]	$\gamma_{\min}$	K $[10^3/\mathrm{m}^2]$	$K_{\gamma=160}$ $[10^3/\mathrm{m}^2]$
8	180 ± 20	62	70
12	160 ± 20	42	42
24	80 ± 10	< 20	< 10

Table 6.1: *A simple geometrical estimation of the plasma lens strength based on the measured data presented in figure 6.8.*

6.3 Model of the plasma lens based on the beam envelope equation

The experimental data of the spectrally resolved passive plasma lens (figure 6.8) can be modeled using the *beam envelope equation* Reiser 2008, p. 181. The beam envelope equation is an ordinary differential equation, whose solution is the beam radius depending on the propagation distance:

$$r'' = \frac{\varepsilon^2}{r^3} - K \cdot r \tag{6.2}$$

where r is the beam radius at a certain point and ε is the emittance of the beam and K is the focusing strength as before.

The electron beam is modeled by its parameters radius r, divergence r', normalized emittance ε^n and beam energy given by γ. The emittance used in equation 6.2 is calculated via $\varepsilon \approx \varepsilon^n/\gamma$ (equation A.2). Also, the focusing strength K of the lens has to be scaled with $1/\gamma$ of each energy of the beam. Using the initial conditions for every energy a beam is traced through a 2 mm long lens of constant focusing strength, followed by a 570 mm drift space ($K = 0$) to obtain its final size r at the position where the scintillating screen had been placed in the experiment. This has been repeated for various different electron energies to obtain the energy dependent profile with the lens. A second energy dependent profile without the lens has been obtained by repeating the entire operation with the lens out of operation ($K \equiv 0$). For the comparison with the experimental data, the numerical data has been blurred by a Gaussian filter with $\sigma = 4$ pixels accounting for the imaging system used in the experiment as well as the calculation of the averaged and aligned profiles. Although the procedure described above involves on the order of 100 numerical solutions of equation 6.2 for a single profile, the computation time is negligible on today's computers. The computed energy dependent contrast was fitted to the experimental data. The fit used the estimates from table 6.1 as initial conditions.

It has been found that, by fixing the emittance of the beam to $\varepsilon^n = 0.5$ mm mrad, the other three fit parameters ($K_{\gamma=160}, r_0, r'_0$) can be retrieved by fitting the numerical solution to the experimental data. The results of this process are displayed in figure 6.9. For the lower two gap lengths (8 mm, figure 6.9a and 12 mm, figure 6.9b) an energy dependent minimum is clearly visible, which allows all three fit parameters to be determined. This is not the case at the 24 mm gap length: The minimum is not visible and consequently the focusing strength of the lens as well as the beam radius r_0 have huge error bars, while depending on each other. Therefore assuming a focusing strength of $K_{\gamma=160} = 7 \cdot 10^3 / \text{m}^2$ – which is in the range of expectations from the estimation in

table 6.1 leads to a reasonable beam size at the lens entrance. This shows, that the lensing effect can be modeled by the beam envelope equation. In the case of a visible minimum (figure 6.9a, figure 6.9b) it can actually be used to increase the accuracy of the lens and beam parameter estimation.

The emittance of the beam has been set to $\varepsilon^n = 0.5\,\mathrm{mm\,mrad}$ for the model fit. Due to the required resolution it is not possible to retrieve the beam's emittance from the experimental data. However, there are still limits in which the emittance can be varied: Assuming an emittance of $\varepsilon^n > 1\,\mathrm{mm\,mrad}$, it is impossible to fit the experimental data unless the absolute beam size on the scintillation screen exceeds the experimentally measured margin. Smaller emittances as low as $\varepsilon^n \approx 0.1\,\mathrm{mm\,mrad}$ however would still lead to an accurate modeling of the results. For even lower emittances the beam sizes on the scintillation screen also deviate strongly.

As the beam envelope equation is only modeling one energy at a time, the emittance used is the emittance of a single energy only. Electrons of different energies may still populate different areas in phase space increasing the overall beam emittance significantly. A pepper pot measurement of the emittance does not resolve energy, which is why such a measurement would measure the phase space volume populated by electrons of all energies combined. This may lead to a much larger overall emittance as assumed in section 6.2.
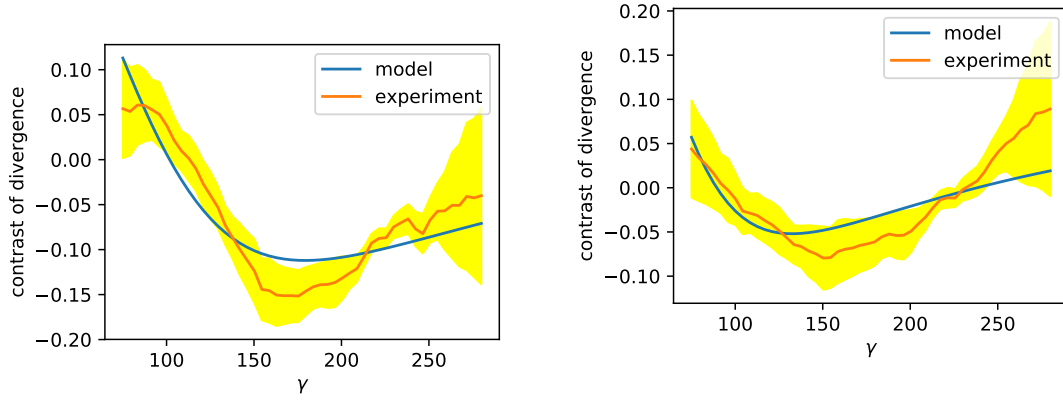
(a) $L_{gap} = 8\,\text{mm}$
$K_{\gamma=160} = (72 \pm 12) \cdot 10^3\,/\text{m}^2$,
$r_0 = (8 \pm 1)\,\mu\text{m}$, $r_0' = (1.1 \pm 0.1)\,\text{mrad}$

(b) $L_{gap} = 12\,\text{mm}$
$K_{\gamma=160} = (26 \pm 4) \cdot 10^3\,/\text{m}^2$,
$r_0 = (15 \pm 1)\,\mu\text{m}$,
$r_0' = (1.0 \pm 0.1)\,\text{mrad}$
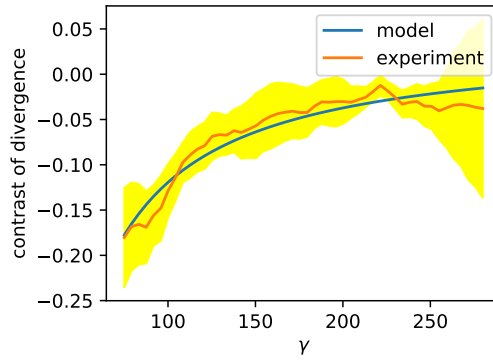
(c) $L_{gap} = 24\,\text{mm}$
$K_{\gamma=160} = (1 \pm 24) \cdot 10^3\,/\text{m}^2$,
$r_0 = (170 \pm 3200)\,\mu\text{m}$,
$r_0' = (1.9 \pm 0.6)\,\text{mrad}$
fixing $K_{\gamma=160} = 7 \cdot 10^3\,/\text{m}^2$ *leads to:*
$r_0 = (30 \pm 0.5)\,\mu\text{m}$,
$r_0' = (2.1 \pm 0.2)\,\text{mrad}$

Figure 6.9: *The measured passive plasma lensing effect (including $\pm 1\sigma$ error) for differ-*
ent gap lengths is compared with the modeling by the beam envelope equation
(equation 6.2): The experimental data presented is the same as in figure 6.8,
but here plotted over $\gamma = \frac{E_{kin}}{mc^2} - 1$. *The parameters mentioned in the captions*
have been varied to fit the model to the experimental data. A beam emittance
of $\varepsilon^n = 0.5\,\text{mm mrad}$ *has been assumed. The lensig effect can be clearly repro-*
duced by the beam envelope model, yielding accurate estimates of the lensing
parameters.

6.4 Discussion of the plasma lensing effect

The plasma lens measurements are compared to the simple analytical model, that has been introduced in section 5.2. It consists of two scaling laws, which are equation 5.12 in the underdense ($n_b > n_p$) and equation 5.13 in the overdense regime. Strictly this model is valid for long bunches only. However, its predictions are surprisingly similar to the measured values as seen in the following.

The theoretical scaling is shown for different bunch and plasma densities in figure 6.10. In case of the underdense regime, the focusing strength only scales with the plasma density n_p. Since the model assumes, that the plasma density is depleted by the bunch, the return currents are forced around the bunch and the transverse beam size $\sigma_\perp$ has no influence. In case of the overdense regime, K scales with the bunch density n_b. The focusing strength is reduced by return currents inside the bunch. A reduction of the plasma density n_b therefore also decreases k_p and the return currents move outward the electron bunch That is why a reduction of the plasma density counter intuitively increases the focusing strength K (figure 6.10).

For comparison with the experimental data, the measured lensing strenghts retrieved from figure 6.9 are also shown in figure 6.10. The three data points correspond to different transverse beam sizes, which is why only one of the points in each graphic can be directly compared to the scaling shown: In the left (right) plot only the upmost (lowest) point corresponds to the beam size, for which the scaling is calculated. The point is indicated by a black arrow. The other points are merely shown to indicate the trend. The scaling is much better visible in the profile of constant plasma density (figure 6.10, lower graphic): The three black points indicate the data from the experiment including errorbars and the lines show the scaling for different transverse bunch sizes $\sigma_\perp$ depending on the bunch density n_b. As soon as the bunch density crosses $1 \cdot 10^{19} /\mathrm{cm}^3$, the overdense regime is reached and the sudden jump in the scaling occurs because the underdense model assumes no return current inside the bunch in this regime.

The plasma density of the plasma lens in the experiment was $n_p = 1 \cdot 10^{19} /\mathrm{cm}^3$. With the estimated $\sigma_\parallel = 2\,\mu\mathrm{m}$, this results in $k_p\sigma_\parallel = 1.2$. The transverse extent of the electron bunch depends on the gap length between cell and jet and therefore $k_p\sigma_\perp$ reaches from 4.7 to 18 for different gap lengths.

The actual values plotted are listed in table 6.2 for comparison. While $\sigma_\perp = 8\,\mu\mathrm{m}$ almost matches the focusing strength, $\sigma_\perp = 15\,\mu\mathrm{m}$ underestimates it. This is a surprising result, because the passive lensing seems to work much better for the low gap length compared to what the model suggests, although the bunch itself is quite short. In fact, assuming
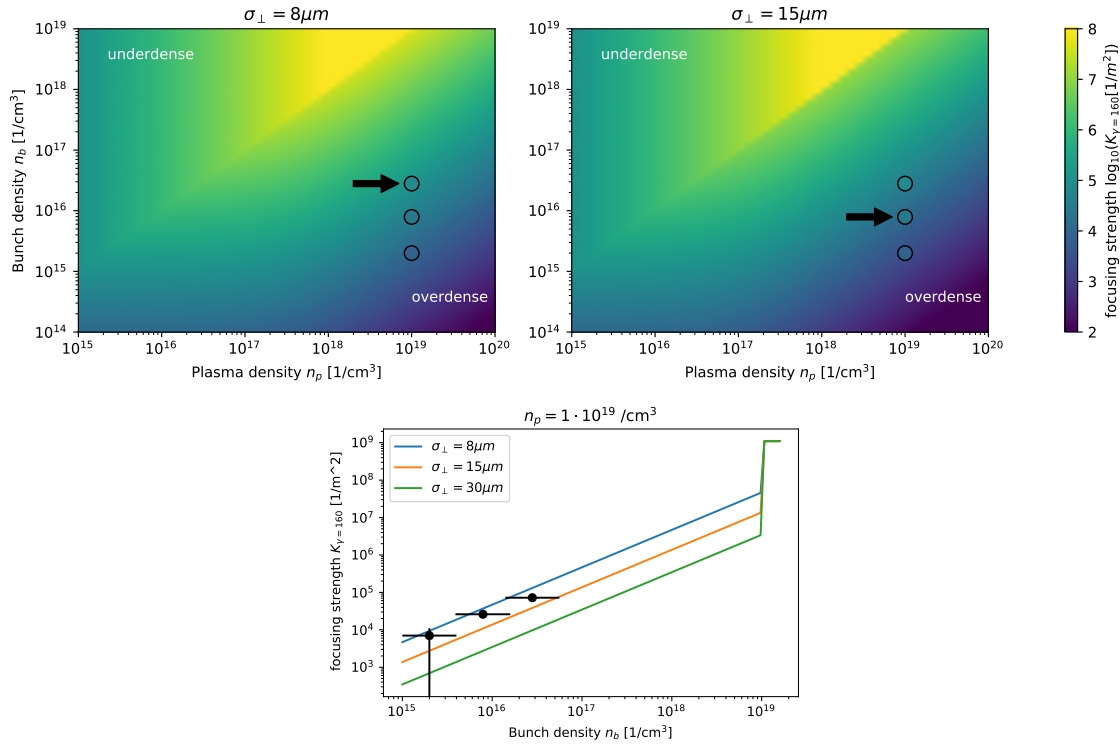
Figure 6.10: *Theoretical scaling of the passive plasma lens effect depending on the bunch n_b and plasma density n_p. It showns equation 5.12 in the underdense and equation 5.13 in the overdense regime. Since there is no reduction due to return currents in the underdense regime a sudden jump of the focusing strength is visible when changing from one regime to another. The difference between the upper two plots is the assumed transverse size $\sigma_\perp$ of the electron bunch which affects the return currents, particularly for large plasma densities. For comparison the values deduced from the experimental data fitted to the beam model (figure 6.9) are marked in both plots. Since the size of the beam differs for different gap lengths, only the upmost (lowest) point in the left (right) plot is directly comparable to the scaling shown. The points marked by the black arrow are matching the transverse bunch size $\sigma_\perp$. The lower plot shows the profile along $n_p = 1 \cdot 10^{19}$ /cm^3. The black dots indicate the data points from the experiment. The errorbars for K are taken from table 6.2. A relative error of factor 2 is assumed for the bunch density.*

L_{gap}	n_b [1/cm^3]	$K_{\gamma=160}$ [10^3/m^2]			$K_{\gamma=160}$ [10^3/m^2]
		$\sigma_\perp=8\,\mu$m $k_p\sigma_\perp = 4.7$	$\sigma_\perp=15\,\mu$m $k_p\sigma_\perp = 9$	$\sigma_\perp=30\,\mu$m $k_p\sigma_\perp = 18$	measured
8 mm	$28 \cdot 10^{15}$	**130**	38	9.7	72 ± 12
12 mm	$8 \cdot 10^{15}$	37	**11**	2.8	26 ± 4
24 mm	$2 \cdot 10^{15}$	9.4	2.7	**0.7**	7^{+3}_{-7}

Table 6.2: *Calculated and measured values for $K_{\gamma=160}$ in units of 10^3 /m^2. The measured values are taken from figure 6.9 and the bunch density is an estimate based on the beam size retrieved from the experimental data. The model predicts the bold values for the actually measured values. A plasma density in the lensing stage of $n_p = 1 \cdot 10^{19}$ /cm^3 has been used for the calculations to match the measurement of the experiment.*

$\sigma_\| = 2\,\mu$m yields $k_p\sigma_\| = 1.2$ at $n_p = 1 \cdot 10^{19}$ /cm^3. This is exactly the regime in which analytical descriptions break down as described in section 5.2. In the transverse direction $\sigma_\perp = 15\,\mu$m corresponds to $k_p\sigma_\perp = 9$, which is very similar to the simulation shown in figure 5.5. This simulation shows that a significant focusing force is not only created by the magnetic field, but also by the electric field, which is not included into the model. Hence, this may provides a possible reason for a stronger focusing force, compared to the prediction of the model. Moreover figure 5.6 shows the same effect, but even stronger for a variation of the electron bunch parameters. Here the electric focusing field is the major contribution to the focusing. It is therefore reasonable to assume that the electric field may have contributed to the focusing effect in the experiment. However the general trend and the order of magnitude of the focusing effect are reproduced by that simple model.

Various parameters of the particle bunch can only be estimated in the experiment. In addition to its exact length $\sigma_\|$, the electron bunch may have an energetic chirp. As presented in section 3.2.3, ionization injection is a continuous injection process and electrons which were injected first should end up with the highest energy, as long as dephasing has not yet set in. Therefore it is logical to assume an energetic chirp within the electron bunch with the most energetic electrons at the head and the lowest energetic electrons at the tail of the bunch. The lowest energetic electrons may therefore experience a focusing field induced by the high energetic electrons. Consequently, it may be possible to exploit the longitudinally varying focusing strength as a diagnostic for the length of the particle bunch or its chirp. Those measurements are still subject to research because established methods for measuring the bunch duration can only give an upper bound for these ultrashort electron bunches. Of course, such measurements require a comprehensive understanding of the (non-linear) plasma wake response in 3D.

In order to increase the effect of the passive plasma lensing, the model (figure 6.10) suggests two options: Starting from the parameters of this experiment, decreasing of the plasma density n_p, would push return currents out of the bunch, and thus increasing the focusing effect. As the LWFA electron bunch is ultrashort, this may also impair the focusing as soon as the plasma response shifts behind the electron bunch as in figure 5.7, which is not included in the scaling. The second option of increasing the bunch density n_b seems promising: An increased bunch density will shift the experiment towards the underdense regime, expecting a strong increase of the plasma lens strength. This is an experimentally viable option by moving the entire experiment to a large laser system in order to accelerate more charge. The current experiment has been carried out with a few pC of charge whereas larger laser systems like Astra Gemini (Rutherford Appleton Laboratory, UK) have shown to accelerate up to a few 100 pC, which is an increase of factor 100 in accelerated charge. Increasing n_b by two orders of magnitude will also increase the focusing strength by two orders of magnitude, following the scaling shown in figure 6.10. In addition, the return currents might be forced around the electron bunch on the transition from the over- to the underdense regime, resulting in an additional increase of focusing strength (figure 6.10). Assuming that the acceleration process can deliver enough charge, it is most intriguing to probe this parameter range and measure how the effect scales on the transition from the over- to the underdense regime.

In general, the increase of focusing strength K is important in two ways: First, the larger focusing strength enhances the signal-to-noise ratio, allowing a more detailed analysis. Secondly, using larger bunch charges will shift the entire experiment towards the underdense regime, where the electron bunch drives a considerable plasma wake within the background plasma. Using the transverse probing [Schwab et al. 2013], which is available at the JETI 40 and JETI 100[2] laser systems, this may lead to imaging of a beam driven wakefield. Also, the charge dependent focusing should be measured. Currently, first experiments are in preparation.

Finally, it is interesting to compare the passive plasma lens to conventional focusing devices. Conventional quadrupole magnets typically operate around a strength of $K_Q \approx 50\,\text{T/m}$. Using equation 5.17 together with $F = qcB$ for a relativistic electron beam leads to $K = \frac{qK_Q}{\gamma mc} \approx \frac{29 \cdot 10^3}{\gamma}\,1/\text{m}^2$ which corresponds to $K^{\text{Q}}_{\gamma=160} = 0.18 \cdot 10^3\,1/\text{m}^2$ in the focusing direction. A quadrupole lens focuses one transverse direction while it defocuses the other. Accordingly lens doublets or triplets are used to focus the beam in both directions, leading to an even lower net focusing strength. The passive plasma lens demonstrated in this work, has a focusing strength of up to $K^{\text{passive}}_{\gamma=160} = 72 \cdot 10^3\,/\text{m}^2$, which is more than two orders of magnitude stronger. Moreover, it focuses both trans-

---

[2]sub 20 fs, 4 J

verse directions of the beam simultaneously. The active plasma lens demonstrated by Thaury et al. 2015 can be estimated with $K_{\gamma=160}^{\text{active}} = 2000 \cdot 10^3 \, 1/\text{m}^2$ at $n_p = 4 \cdot 10^{18} \, /\text{cm}^3$, which is even stronger. However, a sufficiently dense electron bunch should be able to excite a plasma wake of similar amplitude which should increase the focusing strength of the passive plasma lens to a similar value. From our results we can put boundaries on possible emittance growth and find that the effects are at best negligible and most tolerable for many applications. The single shot analysis shows, that the passive plasma lens is also stable in comparison to the stability of the laser driven acceleration process. Further work is required for a full characterisation of the passive plasma lens with regards to quantify the emittance. Clearly plasma lenses have very strong focusing capabilities compared to conventional approaches and are well matched to the compact scale of LWFA accelerators, providing a new and useful experimental tool.

7 Conclusion & Outlook

Laser wake field acceleration (LWFA) is a promising concept to complement conventional radio-frequency (RF) accelerators. In LWFA, a high intensity laser pulse is intrinsically synchronized to an ultra short and dense electron bunch, which provides an ideal platform for experiments investigating QED at high intensities. However, the quality and stability of LWFA electron beams still requires significant improvement in order to make such experiments possible. Beyond testing QED in high fields, the stability and quality of laser accelerated electron beams are also crucial for applications such as LWFA driven free-electron lasers.

Laser plasma accelerators have been studied in this thesis by experiments, simulations and analytical theory. The experiments were performed at the $40\,\mathrm{TW}$ high intensity laser system JETI at the Institute of Optics and Quantum Electronics in Jena. Particle-in-cell simulations were used for the interpretation of the experimental results. They were analyzed using the python code, called postpic, which was developed in this PhD work and is the first open-source package for post-processing of PIC simulation data.

The first part of this thesis is focused on the improvement of the laser-driven electron acceleration. It is shown that the injection process plays a crucial role for the stability of the electron beam. The injection, which is the transition of electrons from the plasma into the accelerating phase of the plasma wake, is often realized by wave breaking. This is a highly non-linear process depending on the phase velocity (β_p) and the amplitude of the plasma wake. Novel experimental techniqes were used to investigate the injection process. Using a few-cycle probe pulse, plasma density variations were measured in widely used gas jets with a resolution of $10\,\mu\mathrm{m}$ for the first time. It is observed that the plasma wavelength varies during propagation. As these density variations could not been resolved up to now, their influence could not be investigated. Simulations and analytical theory presented here reproduce the experimental observations. Two contributions to the phase velocity of the plasma wake have been identified – the down ramp term as well as the etching and dispersion term. The measurement of the density variations allowed quantifying the contributions of these terms individually. Surprisingly, a detailed analysis shows that the down ramp term is the dominant contribution to the phase velocity of the wake. As a result, injection is triggered by the density variations in the experiments

with the gas jet. It is obvious that random density fluctuations in the gas jet also affect the stability and quality of the electron beam, which has also been confirmed by the experimental data.

To mitigate the density variations, a gas cell has been developed with an emphasis on the homogeneity of the plasma. Experiments using the gas cell show that the plasma density variations disappear. As expected, no self-injection could be observed using the gas cell. It is important to note that the self-injection free regime is a requirement for a plasma based accelerator in which the injection is decoupled from the acceleration stage. Therefore ionization injection has been used in the gas cell to initiate the acceleration process. Using a homogeneous gas target and ionization injection, the performance of the laser plasma accelerator has been significantly enhanced. The pointing stability of the electron beam has been increased by an order of magnitude. Moreover, the electron beam profile was improved and shows less deviations between individual laser shots compared to the gas jet. These results are important for the development of stable laser plasma accelerators that might be used in future high field QED experiments. The influence of possible plasma density variations is also important in a broader context, for example, in particle beam driven wake field acceleration (PWFA).

In addition to the improved performance of the laser plasma accelerator, high field QED experiments also require dense electron bunches. A passive plasma lens was investigated using experiments and 3D PIC simulations for the focusing of ultra-short LWFA electron bunches. In the experiments, the passive plasma lens was realized by a second gas target such that the laser accelerated electron bunch propagates through a second plasma with defined plasma density. The analysis of the electron beam divergence shows a focusing effect which is attributed to passive plasma lensing in the second plasma target. Using this compact all-optical setup, passive plasma lensing was demonstrated experimentally with an ultra-short electron bunch for the first time. Plasma lensing was further studied using PIC simulations and analytical modeling which reproduce the lensing effect. For the estimated parameters of the experiment, an analytical model based on the beam envelope equation was further used to determine the focusing strength of the passive plasma lens. It was found that the focusing strength of the passive plasma lens is much stronger compared to quadrupole magnets. In addition, the plasma lens is able to focus both transverse directions simulatneously. An analytical model is introduced that predicts a favorable scaling of the plasma lensing for higher bunch charges. The passive plasma lensing may therefore become a simple but effective tool to focus electron beams in future experiments.

As an outlook, experiments are planed at the JETI 100 laser system at the Helmholtz-Insitute Jena. Due to the higher power of this laser system, higher charges are expected.

Accordingly, a much stronger focsing strength, as predicted by the model, would result in a dense electron beam. This also pushes the plasma lensing towards the underdense regime, which may have reduced aberrations. Such a focused, ultra-short electron bunch is essential for many high field QED experiments.

One of the envisioned QED experiments (Chapter 1) has already been conducted at the Astra Gemini laser system at the Rutherford Appleton Laboratory (RAL), UK. In this experiment, the equation of motion of a free electron in an intense electromagnetic field was investigated - the so-called radiation reaction problem. Remarkably very basic problem does not yet have a generally accepted solution which is correct across all intensity regimes. In particular the description at very high field strengths, where quantum effects in the emission of photons becomes a significant effect on the electron's trajectory becomes important does not yet have a solution. To access this regime a ultrarelativstic electron beam interacting with a high intensity laser field was investigated. By colliding a dense electron bunch with a high intensity laser field, γ-rays are emitted, which can contain a significant fraction of the electron energy. Their energy loss due to radiation reaction has been observed for the first time. Eventually, such experiments can help to differentiate between different regimes and models of radiation reaction. The classically self-consistent equation of motion including radiation reaction is the Landau-Lifshitz equation. QED calculations, on the other hand, show a different energy loss when the quantum parameter $\chi = \frac{2\hbar}{m_e c^2}\omega_L \gamma a_0$ approaches unity[1]. A comparison of classical and QED models with the experimental data is therefore required to develop an equation of motion based on QED, which is correct across the full range of possible parameters Poder et al. 2017a.

---

[1] For a laser with $\lambda = 800\,\mathrm{nm}$ this simplifies to $\chi \approx 6 \cdot 10^{-6} \gamma a_0$.
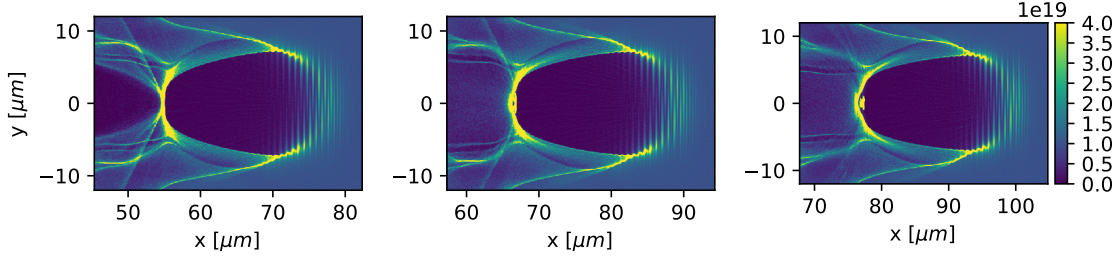
A Appendix

Figure A.1: *Snapshots of the wave-breaking process: The color scale indicates the plasma density in units of $1/\mathrm{cm}^3$. The laser pulse $(a_0 = 10)$ in this 2D PIC simulation is propagating from left to right. It visualizes the principle of wave breaking. The first density spike behind the laser pulse increases its amplitude until some of the plasma electrons separate and become trapped in the plasma wave, which is exited by the laser pulse.*

A.1 Trace space and emittance of a particle beam

A single particle is fully characterized by its position in the 6-dimensional phase space (x, y, z, p_x, p_y, p_z). An ensemble of particles is therefore characterized by a density in this phase space. According to Liouville's theorem the volume in phase is a conserved quantity as long as the particles are not interacting with each other. In other words: the phase space density along any particle trajectory is conserved. The volume occupied by a particle beam is therefore good measure for the quality of the beam, meaning to what spot size it can be focused to.

Instead of considering the 6-dimensional volumes it is common to look at the projection onto the two two-dimensional transverse planes x-p_x and y-p_y for a beam propagating in z-direction [Floettmann 2003]. With non-interacting particles the area of each transverse phase-space projection Γ_x, Γ_y is conserved. This relates to the *normalized emittance ε^n*:

$$\varepsilon_x^n = \frac{\Gamma_x}{\pi m_e c} \tag{A.1}$$

and likewise for ε_y^n.

Instead of measuring momentum it is more practical to measure the beam's energy and divergence $x' = \frac{p_x}{p_z} \approx \frac{p_x}{p}$, which is why the so-called *trace space x-x'* is introduced. The area A_x occupied by the beam in trace space relates to the *geometric emittance* $\varepsilon_x = A_x/\pi$ and the relation between the geometric and normalized emittances is

$$\varepsilon^n = \gamma \beta_z \varepsilon \tag{A.2}$$

In a real world measurement x and x' can have various profiles which is why it may become difficult to assign a single Δx and $\Delta x'$ value. A straight forward way is the use of the standard deviation for the beam size $\Delta x = \sigma_x$ and the standard deviation of the divergence $\Delta x' = \sigma_{x'}$. The calculation of ε^n becomes trivial, if all values are measured in the focus of the beam (!):

$$\varepsilon_x^n = \gamma\beta_y \cdot \sigma_x \cdot \sigma_{x'} \tag{A.3}$$

The trace space area A_x is consequently identical to the area of an ellipse with half axis σ_x and $\sigma_{x'}$, which motivates its definition above [Becker et al. 2006].

An electron beam focused to $\sigma_x = 10\,\mu\text{m}$ at a divergence of $\sigma_{x'} = 1\,\text{mrad}$ at an energy of $100\,\text{MeV}$ ($\gamma \approx 200$) has therefore a normalized emittance of approximately $\varepsilon_x^n = 2\,\text{mm}\,\text{mrad}$. Since the emittance was historically sometimes identified as the trace space area this was written as $\varepsilon_x^n = 2\,\pi\,\text{mm}\,\text{mrad}$, to clarify that π has not been multiplied in, just in case someone would rather calculate the area of the trace space ellipse. Nowadays many publications instead write $\varepsilon_x^n = 2\,\mu\text{m}$, because rad is dimensionless and therefore omitted. The different notations often lead to confusion, which is why it is important to note that all three notations describe identical beams [Becker et al. 2006].

B List of publications (chronological)

unpublished

1. K. Behm, J. M. Cole, A. Joglekar, E. Gerstmayr, C. Baird, T. G. Blackburn, M. Duff, C. Harvey, A. Ilderton, **S. Kuschel**, S. P. D. Mangles, M. Marklund, P. McKenna, C. D. Murphy, Z. Najmudin, K. Poder, C. P. Ridgers, G. M. Samarin, G. Sarri, D. R. Symes, J. Warwick, J. Wood, M. Zepf, K. Krushelnick, A. G. R. Thomas "Novel design of a gamma ray spectrometer measuring spectra with photon energies greater than 100 MeV" *submitted to RSI*,

2. **S. Kuschel**, M. B. Schwab, W. Ziegler, M. Yeung, D. Hollatz, A. Sävert, M. C. Kaluza, M. Zepf "Background free ionization injection for pointing stablity enhancement" *in preparation*,

published

1. A. Blinne, D. Schinkel, **S. Kuschel**, N. Elkina, S. G. Rykovanov, M. Zepf "A Systematic Approach to Numerical Dispersion in Maxwell Solvers" *arXiv*, 1710.06829 (2017)

2. K. Poder, M. Tamburini, G. Sarri, A. Di Piazza, **S. Kuschel**, C. D. Baird, K. Behm, S. Bohlen, J. M. Cole, M. Duff, E. Gerstmayr, C. H. Keitel, K. Krushelnick, S. P. D Mangles, P. McKenna, C. D. Murphy, Z. Najmudin, C. P. Ridgers, G. M. Samarin, D. Symes, A. G. R Thomas, J. Warwick, M. Zepf "Evidence of strong radiation reaction in the field of an ultra-intense laser" *arXiv*, 1709.01861v2 (2017)

3. J. M. Cole, K. T. Behm, E. Gerstmayr, T. G. Blackburn, J. C. Wood, C. D. Baird, M. J. Duff, C. Harvey, A. Ilderton, A. S. Joglekar, K. Krushelnick, **S. Kuschel**, M. Marklund, P. McKenna, C. D. Murphy, K. Poder, C. P. Ridgers, G. M. Samarin, G. Sarri, D. R. Symes, A. G. R. Thomas, J. Warwick, M. Zepf, Z. Najmudin, S. P. D. Mangles "Experimental observation of radiation reaction in the collision of a high-intensity laser pulse with a laser-wakefield accelerated electron beam" *arXiv*, 1707.06821v1 (2017)

4. M. Yeung, S. Rykovanov, J. Bierbach, L. Li, E. Eckner, **S. Kuschel**, A. Wold-egeorgis, C. Rödel, A. Sävert, G. G. Paulus, M. Coughlan, B. Dromey, M. Zepf "Experimental observation of attosecond control over relativistic electron bunches with two-colour fields" *Nature Photonics*, 11, 32-35 (2017)

5. G. Sarri, J. Warwick, W. Schumaker, K. Poder, J. Cole, D. Doria, T. Dzelzainis, K. Krushelnick, **S. Kuschel**, S. P. D. Mangles, Z. Najmudin, L. Romagnani, G. M. Samarin, D. Symes, A. G. R. Thomas, M. Yeung, M. Zepf "Spectral and spatial characterisation of laser-driven positron beams" *Plasma Physics and Controlled Fusion*, 59, 014015 (2017)

6. **S. Kuschel**, D. Hollatz, T. Heinemann, O. Karger, M. B. Schwab, D. Ullmann, A. Knetsch, A. Seidel, C. Rödel, M. Yeung, M. Leier, A. Blinne, H. Ding, T. Kurz, D J. Corvan, A. Sävert, S. Karsch, M. C. Kaluza, B. Hidding, M. Zepf "Demonstration of passive plasma lensing of a laser wakefield accelerated electron bunch" *Physical Review Accelerators and Beams*, 19, 071301 (2016)

7. B. Dromey, M. Coughlan, L. Senje, M. Taylor, **S. Kuschel**, B. Villagomez, R. Stefanuik, G. Nersisyan, L. Stella, J. Kohanoff, M. Borghesi, F. Currell, D. Riley, D. Jung, C.-G. Wahlström, C. L. S. Lewis, M. Zepf "Picosecond metrology of laser-driven proton bursts" *Nature Communications*, 7:10642 (2016)

8. M. Yeung, J. Bierbach, E. Eckner, S. Rykovanov, **S. Kuschel**, A. Sävert, M. Förster, C. Rödel, G. G. Paulus, S. Cousens, M. Coughlan, B. Dromey, M. Zepf "Noncollinear Polarization Gating of Attosecond Pulse Trains in the Relativistic Regime" *Physical Review Letters*, 115, 19 (2015)

9. J. Bierbach, M. Yeung, E. Eckner, C. Rödel, **S. Kuschel**, M. Zepf, G. G. Paulus "Long-term operation of surface high-harmonic generation from relativistic oscillating mirrors using a spooling tape" *Optics Express*, 23(9):12321-7 (2015)

10. G. Sarri, K. Poder, J. M. Cole, W. Schumaker, A. Di Piazza, B. Reville, T. Dzelzainis, D. Doria, L. A Gizzi, G. M. Grittani, S. Kar, C. H. Keitel, K. Kruschelnik, **S. Kuschel**, S. P. D. Mangles, Z. Najmudin, N. Shukla, L. O. Silva, D. Symes, A. G. R. Thomas, M. Vargas, J. Vieira, M. Zepf "Generation of neutral and high-density electron–positron pair plasmas in the laboratory" *Nature Communications*, 6:6747 (2015)

11. B. Aurand, **S. Kuschel**, C. Rödel, O. Jäckel, J. Polz, B. Elkin, H. Zhao, A. Karmakar, P. Gibbon, M. C. Kaluza, T. Kühl "Reduction of X-ray generation in high-intensity laser ion acceleration" *Applied Physics B*, 118(2):247-251 (2015)

12. L. Senje, M. Yeung, B. Aurand, **S. Kuschel**, C. Rödel, F. Wagner, K. Li, B. Dromey, V. Bagnoud, P. Neumeyer, M. Roth, C.-G. Wahlström, M. Zepf, T. Kühl, D. Jung "Diagnostics for studies of novel laser ion acceleration mechanisms" *Review of Scientific Instruments*, 85(11):113302 (2014)

13. T. Hahn, J. Bierbach, C. Rödel, D. Hemmers, M. Yeung, B. Dromey, S. Fuchs, A. G. Pour, **S. Kuschel**, M. Zepf, G. G. Paulus, G. Pretzler "Broadband XUV polarimetry of high harmonics from plasma surfaces using multiple Fresnel reflections" *Applied Physics B*, 118(2):241-245 (2014)

14. B. Aurand, **S. Kuschel**, O. Jäckel, C. Rödel, H. Zhao, S. Herzer, A. E. Paz, J. Bierbach, J. Polz, B. Elkin, A. Karmakar, P. Gibbon, M. C. Kaluza, T. Kühl "Enhanced radiation pressure-assisted acceleration by temporally tuned counter-propagating pulses" *Nuclear Insturments and Methdos*, 740, 83-86 (2014)

15. B. Aurand, B. Elkin, L.-O. Heim, B. Lommel, B. Kindler, M. Kindler, M. Tomut, C. Rödel, **S. Kuschel**, O. Jäckel, T. Kühl "Ultra-thin polymer foils for laser-ion acceleration" *Journal of Radiological and Nuclear Chemistry*, 299 (2), 965-968 (2014)

16. B. Aurand, **S. Kuschel**, O. Jäckel, C. Rödel, H. Zhao, S. Herzer, A. E. Paz, J. Bierbach, J. Polz, B. Elkin, G. G. Paulus, A. Karmakar, P. Gibbon, T. Kühl, M. C. Kaluza "Radiation pressure-assisted acceleration of ions using multi-component foils in high-intensity laser–matter interactions" *New Journal of Physics*, 15:033031 (2013)

17. G. Sarri, W. Schumaker, A. Di Piazza, K. Poder, J. M. Cole, M. Vargas, D. Dora, **S. Kuschel**, B. Dromey, G. M. Grittani, L. A Gizzi, M. E. Dieckmann, A. Green, V. Chvykov, A. Maksimchuck. V. Yanovski, Z. He, B. Hou, J. Nees, S. Kar, Z. Najmudin, A. G. Thomas, C. H. Keitel, K. Kruschelnik, M. Zepf "Laser-driven generation of collimated ultra-relativistic positron beams" *Plasma Physics and Controlled Fusion*, 55(12):4017 (2013)

18. B. Aurand, B. Elkin, L.-O. Heim, B. Lommel, B. Kindler, M. Tomut, C. Rödel, **S. Kuschel**, O. Jäckel, J. Barz, T. Kühl "Preparation and Characterization of Nanometer-Thin Freestanding Polymer Foils for Laser-Ion Acceleration" *Journal of Polymer Science Part B Polymer Physics*, 51(81):1355-1360 (2013)

19. S. Fuchs, C. Rödel, M. Krebs, S. Hädrich, J. Bierbach, A. E. Paz, **S. Kuschel**, M. Wünsche, V. Hilbert, U. Zastrau, E. Förster, J. Limpert, G. G. Paulus "Sensitivity calibration of an imaging extreme ultraviolet spectrometer-detector system

for determining the efficiency of broadband extreme ultraviolet sources" *Review of Scientific Instruments*, 84, 023101 (2013)

20. J. Bierbach, C. Rödel, M. Yeung, B. Dromey, T. Hahn, A. G. Pour, S. Fuchs, A. E. Paz, S. Herzer, **S. Kuschel**, O. Jäckel, M. C. Kaluza, G. Pretzler, M. Zepf, G. .G. Paulus "Generation of 10μW relativistic surface high-harmonic radiation at a repetition rate of 10Hz" *New Journal of Physics*, 14:65005-9 (2012)

21. B. Pollock, J. Meinecke, **S. Kuschel**, J. S. Ross, J. L. Shaw, C. Stoafer, L. Divol, G. Tynan, S. H. Glenzer "Simultaneous imaging electron- and ion-feature Thomson scattering measurements of radiatively heated Xe" *The Review of scientific instruments*, 83(10):10E348 (2012)

22. A. E. Paz, **S. Kuschel**, C. Rödel, M. Schnell, O. Jäckel, M. C. Kaluza, G. G. Paulus "Thomson backscattering from laser-generated, relativistically moving high-density electron layers" *New Journal of Physics*, 14(093018) (2012)

23. B. Aurand, C. Rödel, H. Zhao, **S. Kuschel**, M. Wünsche, O. Jäckel, M. Heyer, F. Wunderlich, M. C. Kaluza, G. G. Paulus, T. Kühl "Note: A large aperture four-mirror reflective wave-plate for high-intensity short-pulse laser experiments" *The Review of scientific instruments*, 83(3):036104 (2012)

24. B. Aurand, **S. Kuschel**, C. Rödel, M. Heyer, F. Wunderlich, O. Jäckel, M. C. Kaluza, G. G. Paulus, T. Kühl "Creating circularly polarized light with a phase-shifting mirror" *Optics express*, 19(18):17151-7 (2011)

Patents

1. "Verfahren zur Herstellung ultradünner Polymerfolien"
   Erfinder: B. Aurand, S. Kuschel, C. Rödel, O. Jäckel, B. Elkin, T. Kühl
   DE 10 2012 100 476.5
   Tag der Offenlegung: 25. Juli 2013

C References

Ammosov, Maxim V., Nikolai B. Delone, and Vladimir P. Krainov (1986). *Tunnel Ion-ization Of Complex Atoms And Atomic Ions In Electromagnetic Field.* DOI: `10.1117/12.938695`. URL: `10.1117/12.938695`.

Ammosov, MV, NB Delone, V Krainov, AM Perelomov, VS Popov, MV Terent'ev, Gennady L Yudin, and Misha Yu Ivanov (1987). "Tunnel ionization of complex atoms and of atomic ions in an alternating electric field". In: *Sov. Phys. JETP* 64, pp. 1191–1194.

Arber, T D, K Bennett, C S Brady, A Lawrence-Douglas, M G Ramsay, N J Sircombe, P Gillies, R G Evans, H Schmitz, A R Bell, and C P Ridgers (Nov. 2015). "Contemporary particle-in-cell approach to laser-plasma modelling". In: *Plasma Physics and Controlled Fusion* 57.11, pp. 1–26.

Audet, T. L., M. Hansson, P. Lee, F. G. Desforges, G. Maynard, S. Dobosz Dufrénoy, R. Lehe, J.-L. Vay, B. Aurand, A. Persson, I. Gallardo González, A. Maitrallain, P. Monot, C.-G. Wahlström, O. Lundh, and B. Cros (2016). "Investigation of ionization-induced electron injection in a wakefield driven by laser inside a gas cell". In: *Physics of Plasmas* 23.2, 023110. DOI: `http://dx.doi.org/10.1063/1.4942033`. URL: `http://scitation.aip.org/content/aip/journal/pop/23/2/10.1063/1.4942033`.

Azambuja, R, M Eloy, G Figueira, and D Neely (1999). "Three-dimensional characterization of high-density non-cylindrical pulsed gas jets". In: *Journal of Physics D: Applied Physics* 32.8, p. L35. URL: `http://stacks.iop.org/0022-3727/32/i=8/a=001`.

Barov, N., M. E. Conde, W. Gai, and J. B. Rosenzweig (Jan. 1998). "Propagation of Short Electron Pulses in a Plasma Channel". In: *Phys. Rev. Lett.* 80 (1), pp. 81–84. DOI: `10.1103/PhysRevLett.80.81`. URL: `http://link.aps.org/doi/10.1103/PhysRevLett.80.81`.

Bauer, D., P. Mulser, and W. -H. Steeb (Dec. 1995). "Relativistic Ponderomotive Force, Uphill Acceleration, and Transition to Chaos". In: *Phys. Rev. Lett.* 75 (25), pp. 4622–4625. DOI: `10.1103/PhysRevLett.75.4622`. URL: `http://link.aps.org/doi/10.1103/PhysRevLett.75.4622`.

Becker, R. and W. B. Herrmannsfeldt (2006). "Why *pi* and mrad?" In: *SLAC PUB*, p. 11949. URL: `http://slac.stanford.edu/pubs/slacpubs/11750/slac-pub-11949.pdf`.

Blaclard, G, H Vincenti, R Lehe, and JL Vay (2016). "Pseudo-spectral Maxwell solvers for an accurate modeling of Doppler harmonic generation on plasma mirrors with Particle-In-Cell codes". In: *arXiv preprint arXiv:1608.05739*. URL: https://arxiv.org/abs/1608.05739.

Blinne, A., D. Schinkel, S. Kuschel, N. Elkina, S. Rykovanov, and M. Zepf (Oct. 2017). "A Systematic Approach to Numerical Dispersion in Maxwell Solvers". In: *ArXiv e-prints*. arXiv: 1710.06829 [physics.plasm-ph].

Blumenfeld, Ian, Christopher E Clayton, Franz-Josef Decker, Mark J Hogan, Chengkun Huang, Rasmus Ischebeck, Richard Iverson, Chandrashekhar Joshi, Thomas Katsouleas, Neil Kirby, et al. (2007). "Energy doubling of 42 GeV electrons in a metre-scale plasma wakefield accelerator". In: *Nature* 445.7129, pp. 741–744.

Boggasch, E., B. Heimrich, and D.H.H. Hoffmann (1993). "Focusing behaviour of plasma lenses compared to conventional quadrupole systems". In: *Nuclear Instruments and Methods in Physics Research Section A: Accelerators, Spectrometers, Detectors and Associated Equipment* 336.3, pp. 438–441. ISSN: 0168-9002. DOI: http://dx.doi.org/10.1016/0168-9002(93)91255-L. URL: http://www.sciencedirect.com/science/article/pii/016890029391255L.

Boyd, Robert W. (2008). *Nonlinear optics*. London: Academic.

Brancolini, Valeria (2016). "Full text". In: *CERN Yellow Reports* 1.0. URL: https://e-publishing.cern.ch/index.php/CYR/article/view/210.

Brunetti, E., R. P. Shanks, G. G. Manahan, M. R. Islam, B. Ersfeld, M. P. Anania, S. Cipiccia, R. C. Issac, G. Raj, G. Vieux, G. H. Welsh, S. M. Wiggins, and D. A. Jaroszynski (Nov. 2010). "Low Emittance, High Brilliance Relativistic Electron Beams from a Laser-Plasma Accelerator". In: *Phys. Rev. Lett.* 105 (21), p. 215007. DOI: 10.1103/PhysRevLett.105.215007. URL: http://link.aps.org/doi/10.1103/PhysRevLett.105.215007.

Buck, A., J. Wenz, J. Xu, K. Khrennikov, K. Schmid, M. Heigoldt, J. M. Mikhailova, M. Geissler, B. Shen, F. Krausz, S. Karsch, and L. Veisz (May 2013). "Shock-Front Injector for High-Quality Laser-Plasma Acceleration". In: *Phys. Rev. Lett.* 110 (18), p. 185006. DOI: 10.1103/PhysRevLett.110.185006. URL: http://link.aps.org/doi/10.1103/PhysRevLett.110.185006.

Buck, A., K. Zeil, A. Popp, K. Schmid, A. Jochmann, S. D. Kraft, B. Hidding, T. Kudyakov, C. M. S. Sears, L. Veisz, S. Karsch, J. Pawelke, R. Sauerbrey, T. Cowan, F. Krausz, and U. Schramm (2010). "Absolute charge calibration of scintillating screens for relativistic electron detection". In: *Review of Scientific Instruments* 81.3, p. 033301. DOI: 10.1063/1.3310275. eprint: http://dx.doi.org/10.1063/1.3310275. URL: http://dx.doi.org/10.1063/1.3310275.

Buck, Alexander, Maria Nicolai, Karl Schmid, Chris M. S. Sears, Alexander Savert, Julia M. Mikhailova, Ferenc Krausz, Malte C. Kaluza, and Laszlo Veisz (July 2011). "Real-

time observation of laser-driven electron acceleration". In: *Nat Phys* 7.7, pp. 543–548. ISSN: 1745-2473. DOI: `10.1038/nphys1942`. URL: `http://dx.doi.org/10.1038/nphys1942`.

Bulanov, S., N. Naumova, F. Pegoraro, and J. Sakai (Nov. 1998). "Particle injection into the wave acceleration phase due to nonlinear wake wave breaking". In: *Phys. Rev. E* 58 (5), R5257–R5260. DOI: `10.1103/PhysRevE.58.R5257`. URL: `http://link.aps.org/doi/10.1103/PhysRevE.58.R5257`.

Burke, D. L., R. C. Field, G. Horton-Smith, J. E. Spencer, D. Walz, S. C. Berridge, W. M. Bugg, K. Shmakov, A. W. Weidemann, C. Bula, K. T. McDonald, E. J. Prebys, C. Bamber, S. J. Boege, T. Koffas, T. Kotseroglou, A. C. Melissinos, D. D. Meyerhofer, D. A. Reis, and W. Ragg (Sept. 1997). "Positron Production in Multiphoton Light-by-Light Scattering". In: *Phys. Rev. Lett.* 79 (9), pp. 1626–1629. DOI: `10.1103/PhysRevLett.79.1626`. URL: `https://link.aps.org/doi/10.1103/PhysRevLett.79.1626`.

Bussmann, M., H. Burau, T. E. Cowan, A. Debus, A. Huebl, G. Juckeland, T. Kluge, W. E. Nagel, R. Pausch, F. Schmitt, U. Schramm, J. Schuchart, and R. Widera (2013). "Radiative Signatures of the Relativistic Kelvin-Helmholtz Instability". In: *Proceedings of the International Conference on High Performance Computing, Networking, Storage and Analysis*. SC '13. Denver, Colorado: ACM, 5:1–5:12. ISBN: 978-1-4503-2378-9. DOI: `10.1145/2503210.2504564`. URL: `http://doi.acm.org/10.1145/2503210.2504564`.

Chen, M, E Esarey, CB Schroeder, CGR Geddes, and WP Leemans (2012). "Theory of ionization-induced trapping in laser-plasma accelerators". In: *Physics of Plasmas (1994-present)* 19.3, p. 033101.

Chen, P., D. Cline, W. Craddock, F.J. Decker, R. Iverson, T. Katsouleas, P. Kwok, W. Leemans, S. Masuda, D.D. Meyerhofer, K. Nakajima, A. Ogata, P. Raimondi, A. Sessler, D. Walz, and A. Weidemann (1998). "Plasma lens experiment at the final focus test beam". In: *Nuclear Instruments and Methods in Physics Research Section A: Accelerators, Spectrometers, Detectors and Associated Equipment* 410.3, pp. 407–417. ISSN: 0168-9002. DOI: `10.1016/S0168-9002(98)00153-3`. URL: `http://www.sciencedirect.com/science/article/pii/S0168900298001533`.

Chen, P., J. J. Su, T. Katsouleas, S. Wilks, and J. M. Dawson (Apr. 1987). "Plasma Focusing for High-Energy Beams". In: *IEEE Transactions on Plasma Science* 15.2, pp. 218–225. ISSN: 0093-3813. DOI: `10.1109/TPS.1987.4316688`.

Chen, Pisin (1987). "A possible final focusing mechanism for linear colliders". In: *Particle Accelerators* 20, p. 171.

Clayton, C. E., J. E. Ralph, F. Albert, R. A. Fonseca, S. H. Glenzer, C. Joshi, W. Lu, K. A. Marsh, S. F. Martins, W. B. Mori, A. Pak, F. S. Tsung, B. B. Pollock, J. S. Ross, L. O. Silva, and D. H. Froula (Sept. 2010). "Self-Guided Laser Wakefield Acceleration beyond 1 GeV Using Ionization-Induced Injection". In: *Phys. Rev. Lett.*

105 (10), p. 105003. DOI: `10.1103/PhysRevLett.105.105003`. URL: `http://link.aps.org/doi/10.1103/PhysRevLett.105.105003`.

Cowan, Benjamin M., David L. Bruhwiler, John R. Cary, Estelle Cormier-Michel, and Cameron G. R. Geddes (Apr. 2013). "Generalized algorithm for control of numerical dispersion in explicit time-domain electromagnetic simulations". In: *Phys. Rev. Accel. Beams* 16.4, p. 041303. ISSN: 1098-4402. DOI: `10.1103/PhysRevSTAB.16.041303`.

Decker, C. D., W. B. Mori, K.-C. Tzeng, and T. Katsouleas (1996). "The evolution of ultra-intense, short-pulse lasers in underdense plasmas". In: *Physics of Plasmas* 3.5, pp. 2047–2056. DOI: `http://dx.doi.org/10.1063/1.872001`. URL: `http://scitation.aip.org/content/aip/journal/pop/3/5/10.1063/1.872001`.

Esarey, E., R. F. Hubbard, W. P. Leemans, A. Ting, and P. Sprangle (Oct. 1997). "Electron Injection into Plasma Wakefields by Colliding Laser Pulses". In: *Phys. Rev. Lett.* 79 (14), pp. 2682–2685. DOI: `10.1103/PhysRevLett.79.2682`. URL: `http://link.aps.org/doi/10.1103/PhysRevLett.79.2682`.

Esarey, E., C. B. Schroeder, and W. P. Leemans (Aug. 2009). "Physics of laser-driven plasma-based electron accelerators". In: *Rev. Mod. Phys.* 81 (3), pp. 1229–1285. DOI: `10.1103/RevModPhys.81.1229`. URL: `http://link.aps.org/doi/10.1103/RevModPhys.81.1229`.

Esarey, Eric, Phillip Sprangle, Jonathan Krall, and Antonio Ting (1996). "Overview of plasma-based accelerator concepts". In: *IEEE Transactions on Plasma Science* 24.2, pp. 252–288.

Floettmann, Klaus (Mar. 2003). "Some basic features of the beam emittance". In: *Phys. Rev. ST Accel. Beams* 6 (3), p. 034202. DOI: `10.1103/PhysRevSTAB.6.034202`. URL: `http://link.aps.org/doi/10.1103/PhysRevSTAB.6.034202`.

Froula, D. H., C. E. Clayton, T. Döppner, K. A. Marsh, C. P. J. Barty, L. Divol, R. A. Fonseca, S. H. Glenzer, C. Joshi, W. Lu, S. F. Martins, P. Michel, W. B. Mori, J. P. Palastro, B. B. Pollock, A. Pak, J. E. Ralph, J. S. Ross, C. W. Siders, L. O. Silva, and T. Wang (Nov. 2009). "Measurements of the Critical Power for Self-Injection of Electrons in a Laser Wakefield Accelerator". In: *Phys. Rev. Lett.* 103 (21), p. 215006. DOI: `10.1103/PhysRevLett.103.215006`. URL: `https://link.aps.org/doi/10.1103/PhysRevLett.103.215006`.

Gabor, Dennis (1947). "A space-charge lens for the focusing of ion beams". In: *Nature* 160.4053, pp. 89–90.

Geddes, C. G. R., K. Nakamura, G. R. Plateau, Cs. Toth, E. Cormier-Michel, E. Esarey, C. B. Schroeder, J. R. Cary, and W. P. Leemans (May 2008). "Plasma-Density-Gradient Injection of Low Absolute-Momentum-Spread Electron Bunches". In: *Phys. Rev. Lett.* 100 (21), p. 215004. DOI: `10.1103/PhysRevLett.100.215004`. URL: `https://link.aps.org/doi/10.1103/PhysRevLett.100.215004`.

Gonsalves, AJ, Kei Nakamura, Chen Lin, Dmitriy Panasenko, Satomi Shiraishi, Thomas Sokollik, Carlo Benedetti, CB Schroeder, CGR Geddes, Jeroen Van Tilborg, et al. (2011). "Tunable laser plasma accelerator based on longitudinal density tailoring". In: *Nature Physics* 7.11, pp. 862–866.

Govil, R., W. P. Leemans, E. Yu. Backhaus, and J. S. Wurtele (Oct. 1999). "Observation of Return Current Effects in a Passive Plasma Lens". In: *Phys. Rev. Lett.* 83 (16), pp. 3202–3205. DOI: 10.1103/PhysRevLett.83.3202. URL: http://link.aps.org/doi/10.1103/PhysRevLett.83.3202.

Grebenyuk, Julia, Ralph Assmann, Ulrich Dorda, and Barbara Marchetti (2014). "Plasma acceleration with external injection at SINBAD". In: *Beam Dynamics and Optimization (BDO), 2014 20th International Workshop on.* IEEE, pp. 1–2.

Grote, David P, Alex Friedman, Jean-Luc Vay, and Irving Haber (2005). "The warp code: modeling high intensity ion beams". In: *Lawrence Berkeley National Laboratory.*

Hairapetian, G., P. Davis, C. E. Clayton, C. Joshi, S. C. Hartman, C. Pellegrini, and T. Katsouleas (Apr. 1994). "Experimental demonstration of dynamic focusing of a relativistic electron bunch by an overdense plasma lens". In: *Phys. Rev. Lett.* 72 (15), pp. 2403–2406. DOI: 10.1103/PhysRevLett.72.2403. URL: http://link.aps.org/doi/10.1103/PhysRevLett.72.2403.

Hansson, M., L. Senje, A. Persson, O. Lundh, C.-G. Wahlström, F. G. Desforges, J. Ju, T. L. Audet, B. Cros, S. Dobosz Dufrénoy, and P. Monot (Mar. 2014). "Enhanced stability of laser wakefield acceleration using dielectric capillary tubes". In: *Phys. Rev. ST Accel. Beams* 17 (3), p. 031303. DOI: 10.1103/PhysRevSTAB.17.031303. URL: https://link.aps.org/doi/10.1103/PhysRevSTAB.17.031303.

Hogan, M. J., R. Assmann, F.-J. Decker, R. Iverson, P. Raimondi, S. Rokni, R. H. Siemann, D. Walz, D. Whittum, B. Blue, C. E. Clayton, E. Dodd, R. Hemker, C. Joshi, K. A. Marsh, W. B. Mori, S. Wang, T. Katsouleas, S. Lee, P. Muggli, P. Catravas, S. Chattopadhyay, E. Esarey, and W. P. Leemans (2000). "E-157: A 1.4-m-long plasma wake field acceleration experiment using a 30 GeV electron beam from the Stanford Linear Accelerator Center Linac". In: *Physics of Plasmas* 7.5, pp. 2241–2248. DOI: 10.1063/1.874059. eprint: http://dx.doi.org/10.1063/1.874059. URL: http://dx.doi.org/10.1063/1.874059.

Hu, Huayu, Carsten Müller, and Christoph H. Keitel (Aug. 2010). "Complete QED Theory of Multiphoton Trident Pair Production in Strong Laser Fields". In: *Phys. Rev. Lett.* 105 (8), p. 080401. DOI: 10.1103/PhysRevLett.105.080401. URL: https://link.aps.org/doi/10.1103/PhysRevLett.105.080401.

Jackson (2006). *Klassische Elektrodynamik.* 4th ed. de Gruyter.

Kostyukov, I., A. Pukhov, and S. Kiselev (2004). "Phenomenological theory of laser-plasma interaction in "bubble" regime". In: *Physics of Plasmas* 11.11, pp. 5256–5264.

DOI: `http://dx.doi.org/10.1063/1.1799371`. URL: `http://scitation.aip.org/content/aip/journal/pop/11/11/10.1063/1.1799371`.

Kuschel, S., D. Hollatz, T. Heinemann, O. Karger, M. B. Schwab, D. Ullmann, A. Knetsch, A. Seidel, C. Rödel, M. Yeung, M. Leier, A. Blinne, H. Ding, T. Kurz, D. J. Corvan, A. Sävert, S. Karsch, M. C. Kaluza, B. Hidding, and M. Zepf (July 2016). "Demonstration of passive plasma lensing of a laser wakefield accelerated electron bunch". In: *Phys. Rev. Accel. Beams* 19 (7), p. 071301. DOI: `10.1103/PhysRevAccelBeams.19.071301`. URL: `https://link.aps.org/doi/10.1103/PhysRevAccelBeams.19.071301`.

Kuypers, Friedhelm (2005). *Klassische Mechanik*. Wiley.

Lamb, B. M. and G. J. Morales (1983). "Ponderomotive effects in nonneutral plasmas". In: *Physics of Fluids* 26.12, pp. 3488–3496. DOI: `10.1063/1.864132`. URL: `http://link.aip.org/link/?PFL/26/3488/1`.

Landgraf, Björn, Michael Schnell, Alexander Sävert, Malte C. Kaluza, and Christian Spielmann (2011). "High resolution 3D gas-jet characterization". In: *Review of Scientific Instruments* 82.8, 083106. DOI: `http://dx.doi.org/10.1063/1.3624694`. URL: `http://scitation.aip.org/content/aip/journal/rsi/82/8/10.1063/1.3624694`.

Lehe, R., M. Kirchen, I. A. Andriyash, B. B. Godfrey, and J.-L. Vay (June 2016). "A spectral, quasi-cylindrical and dispersion-free Particle-In-Cell algorithm". In: *Computer Physics Communications* 203, pp. 66–82. DOI: `10.1016/j.cpc.2016.02.007`. arXiv: `1507.04790 [physics.plasm-ph]`.

Lehe, R., A. Lifschitz, C. Thaury, V. Malka, and X. Davoine (Feb. 2013). "Numerical growth of emittance in simulations of laser-wakefield acceleration". In: *Phys. Rev. ST Accel. Beams* 16 (2), p. 021301. DOI: `10.1103/PhysRevSTAB.16.021301`. URL: `http://link.aps.org/doi/10.1103/PhysRevSTAB.16.021301`.

Lemos, N., N. Lopes, J. M. Dias, and F. Viola (2009). "Design and characterization of supersonic nozzles for wide focus laser-plasma interactions". In: *Review of Scientific Instruments* 80.10, 103301. DOI: `http://dx.doi.org/10.1063/1.3233895`. URL: `http://scitation.aip.org/content/aip/journal/rsi/80/10/10.1063/1.3233895`.

Lu, W., C. Huang, M. Zhou, W. B. Mori, and T. Katsouleas (Apr. 2006). "Nonlinear Theory for Relativistic Plasma Wakefields in the Blowout Regime". In: *Phys. Rev. Lett.* 96 (16), p. 165002. DOI: `10.1103/PhysRevLett.96.165002`. URL: `http://link.aps.org/doi/10.1103/PhysRevLett.96.165002`.

Lu, Wei, M Tzoufras, C Joshi, FS Tsung, WB Mori, J Vieira, RA Fonseca, and LO Silva (2007). "Generating multi-GeV electron bunches using single stage laser wakefield acceleration in a 3D nonlinear regime". In: *Physical Review Special Topics-Accelerators and Beams* 10.6, p. 061301.

Lundh, O, J Lim, C Rechatin, L Ammoura, A Ben-Ismail, X Davoine, Guilhem Gallot, JP Goddet, E Lefebvre, Victor Malka, et al. (2011). "Few femtosecond, few kiloampere electron bunch produced by a laser-plasma accelerator". In: *Nature Physics* 7.3, p. 219.

Malka, V., C. Coulaud, J. P. Geindre, V. Lopez, Z. Najmudin, D. Neely, and F. Amiranoff (2000). "Characterization of neutral density profile in a wide range of pressure of cylindrical pulsed gas jets". In: *Review of Scientific Instruments* 71.6, pp. 2329–2333. DOI: `http://dx.doi.org/10.1063/1.1150619`. URL: `http://scitation.aip.org/content/aip/journal/rsi/71/6/10.1063/1.1150619`.

Mangles, S. P. D., G. Genoud, M. S. Bloom, M. Burza, Z. Najmudin, A. Persson, K. Svensson, A. G. R. Thomas, and C.-G. Wahlström (Jan. 2012). "Self-injection threshold in self-guided laser wakefield accelerators". In: *Phys. Rev. ST Accel. Beams* 15 (1), p. 011302. DOI: `10.1103/PhysRevSTAB.15.011302`. URL: `https://link.aps.org/doi/10.1103/PhysRevSTAB.15.011302`.

Mott-Smith, H. M. (June 1951). "The Solution of the Boltzmann Equation for a Shock Wave". In: *Phys. Rev.* 82 (6), pp. 885–892. DOI: `10.1103/PhysRev.82.885`. URL: `http://link.aps.org/doi/10.1103/PhysRev.82.885`.

Nakanishi, H., Y. Yoshida, T. Ueda, T. Kozawa, H. Shibata, K. Nakajima, T. Kurihara, N. Yugami, Y. Nishida, T. Kobayashi, A. Enomoto, T. Oogoe, H. Kobayashi, B. S. Newberger, S. Tagawa, K. Miya, and A. Ogata (Apr. 1991). "Direct observation of plasma-lens effect". In: *Phys. Rev. Lett.* 66 (14), pp. 1870–1873. DOI: `10.1103/PhysRevLett.66.1870`. URL: `http://link.aps.org/doi/10.1103/PhysRevLett.66.1870`.

Ng, J. S. T., P. Chen, H. Baldis, P. Bolton, D. Cline, W. Craddock, C. Crawford, F. J. Decker, C. Field, Y. Fukui, V. Kumar, R. Iverson, F. King, R. E. Kirby, K. Nakajima, R. Noble, A. Ogata, P. Raimondi, D. Walz, and A. W. Weidemann (Nov. 2001). "Observation of Plasma Focusing of a 28.5 GeV Positron Beam". In: *Phys. Rev. Lett.* 87 (24), p. 244801. DOI: `10.1103/PhysRevLett.87.244801`. URL: `http://link.aps.org/doi/10.1103/PhysRevLett.87.244801`.

Osterhoff, J., A. Popp, Zs. Major, B. Marx, T. P. Rowlands-Rees, M. Fuchs, M. Geissler, R. Hörlein, B. Hidding, S. Becker, E. A. Peralta, U. Schramm, F. Grüner, D. Habs, F. Krausz, S. M. Hooker, and S. Karsch (Aug. 2008). "Generation of Stable, Low-Divergence Electron Beams by Laser-Wakefield Acceleration in a Steady-State-Flow Gas Cell". In: *Phys. Rev. Lett.* 101 (8), p. 085002. DOI: `10.1103/PhysRevLett.101.085002`. URL: `http://link.aps.org/doi/10.1103/PhysRevLett.101.085002`.

Pak, A., K. A. Marsh, S. F. Martins, W. Lu, W. B. Mori, and C. Joshi (Jan. 2010). "Injection and Trapping of Tunnel-Ionized Electrons into Laser-Produced Wakes". In: *Phys. Rev. Lett.* 104 (2), p. 025003. DOI: `10.1103/PhysRevLett.104.025003`. URL: `http://link.aps.org/doi/10.1103/PhysRevLett.104.025003`.

Panofsky, W. K. H. and W. R. Baker (1950). "A Focusing Device for the External 350-Mev Proton Beam of the 184-Inch Cyclotron at Berkeley". In: *Review of Scientific Instruments* 21.5, pp. 445–447. DOI: http://dx.doi.org/10.1063/1.1745611. URL: http://scitation.aip.org/content/aip/journal/rsi/21/5/10.1063/1.1745611.

Poder, K., M. Tamburini, G. Sarri, A. Di Piazza, S. Kuschel, C. D. Baird, K. Behm, S. Bohlen, J. M. Cole, M. Duff, E. Gerstmayr, C. H. Keitel, K. Krushelnick, S. P. D. Mangles, P. McKenna, C. D. Murphy, Z. Najmudin, C. P. Ridgers, G. M. Samarin, D. Symes, A. G. R. Thomas, J. Warwick, and M. Zepf (Sept. 2017a). "Evidence of strong radiation reaction in the field of an ultra-intense laser". In: *ArXiv e-prints*. arXiv: 1709.01861 [physics.plasm-ph].

Poder, Kristjan, Jason Cole, Jonathan C Wood, Nelson C Lopes, Saleh Alatabi, Peta Foster, Christos Kamperidis, Olena Kononenko, Charlotte Palmer, Dean Rusby, et al. (2017b). "Measurements of self-guiding of ultrashort laser pulses over long distances". In: *Plasma Physics and Controlled Fusion*.

Pollock, B. B., C. E. Clayton, J. E. Ralph, F. Albert, A. Davidson, L. Divol, C. Filip, S. H. Glenzer, K. Herpoldt, W. Lu, K. A. Marsh, J. Meinecke, W. B. Mori, A. Pak, T. C. Rensink, J. S. Ross, J. Shaw, G. R. Tynan, C. Joshi, and D. H. Froula (July 2011). "Demonstration of a Narrow Energy Spread, ~ 0.5 GeV Electron Beam from a Two-Stage Laser Wakefield Accelerator". In: *Phys. Rev. Lett.* 107 (4), p. 045001. DOI: 10.1103/PhysRevLett.107.045001. URL: http://link.aps.org/doi/10.1103/PhysRevLett.107.045001.

Pukhov, A. (1999). "Three-dimensional electromagnetic relativistic particle-in-cell code VLPL (Virtual Laser Plasma Lab)". In: *J. Plasma Phys.* 61.3, pp. 425–433.

Ralph, J. E., C. E. Clayton, F. Albert, B. B. Pollock, S. F. Martins, A. E. Pak, K. A. Marsh, J. L. Shaw, A. Till, J. P. Palastro, W. Lu, S. H. Glenzer, L. O. Silva, W. B. Mori, C. Joshi, and D. H. Froula (2010). "Laser wakefield acceleration at reduced density in the self-guided regime". In: *Physics of Plasmas* 17.5, 056709. DOI: http://dx.doi.org/10.1063/1.3323083. URL: http://scitation.aip.org/content/aip/journal/pop/17/5/10.1063/1.3323083.

Reiser, Martin (2008). *Theory and Design of Charged Particle Beams*. Wiley-VCH. ISBN: 978-3-527-40741-5. DOI: 10.1002/9783527617623.

Rosenzweig, J. B., B. Breizman, T. Katsouleas, and J. J. Su (Nov. 1991). "Acceleration and focusing of electrons in two-dimensional nonlinear plasma wake fields". In: *Phys. Rev. A* 44 (10), R6189–R6192. DOI: 10.1103/PhysRevA.44.R6189. URL: http://link.aps.org/doi/10.1103/PhysRevA.44.R6189.

Rosenzweig, J. B. and Pisin Chen (Apr. 1989). "Beam optics of a self-focusing plasma lens". In: *Phys. Rev. D* 39 (7), pp. 2039–2045. DOI: 10.1103/PhysRevD.39.2039. URL: http://link.aps.org/doi/10.1103/PhysRevD.39.2039.

Rosenzweig, J. B., P. Schoessow, B. Cole, C. Ho, W. Gai, R. Konecny, S. Mtingwa, J. Norem, M. Rosing, and J. Simpson (1990). "Demonstration of electron beam self-focusing in plasma wake fields". In: *Physics of Fluids B: Plasma Physics (1989-1993)* 2.6, pp. 1376–1383. DOI: 10.1063/1.859559. URL: http://scitation.aip.org/content/aip/journal/pofb/2/6/10.1063/1.859559.

Ruffini, Remo, Gregory Vereshchagin, and She-Sheng Xue (2010). "Electron–positron pairs in physics and astrophysics: from heavy nuclei to black holes". In: *Physics Reports* 487.1-4, pp. 1–140.

Sauter, Fritz (Nov. 1931). "Über das Verhalten eines Elektrons im homogenen elektrischen Feld nach der relativistischen Theorie Diracs". In: *Zeitschrift für Physik* 69.11, pp. 742–764. ISSN: 0044-3328. DOI: 10.1007/BF01339461. URL: https://doi.org/10.1007/BF01339461.

Sävert, A., S. P. D. Mangles, M. Schnell, E. Siminos, J. M. Cole, M. Leier, M. Reuter, M. B. Schwab, M. Möller, K. Poder, O. Jäckel, G. G. Paulus, C. Spielmann, S. Skupin, Z. Najmudin, and M. C. Kaluza (July 2015). "Direct Observation of the Injection Dynamics of a Laser Wakefield Accelerator Using Few-Femtosecond Shadowgraphy". In: *Phys. Rev. Lett.* 115 (5), p. 055002. DOI: 10.1103/PhysRevLett.115.055002. URL: http://link.aps.org/doi/10.1103/PhysRevLett.115.055002.

Sazhin, O. (July 2008). "Gas flow through a slit into a vacuum in a wide range of rarefaction". In: *Journal of Experimental and Theoretical Physics* 107.1, pp. 162–169. ISSN: 1090-6509. DOI: 10.1134/S1063776108070170. URL: https://doi.org/10.1134/S1063776108070170.

Schmid, K., A. Buck, C. M. S. Sears, J. M. Mikhailova, R. Tautz, D. Herrmann, M. Geissler, F. Krausz, and L. Veisz (Sept. 2010). "Density-transition based electron injector for laser driven wakefield accelerators". In: *Phys. Rev. ST Accel. Beams* 13 (9), p. 091301. DOI: 10.1103/PhysRevSTAB.13.091301. URL: http://link.aps.org/doi/10.1103/PhysRevSTAB.13.091301.

Schroeder, C. B., C. Benedetti, E. Esarey, and W. P. Leemans (Mar. 2011). "Nonlinear Pulse Propagation and Phase Velocity of Laser-Driven Plasma Waves". In: *Phys. Rev. Lett.* 106 (13), p. 135002. DOI: 10.1103/PhysRevLett.106.135002. URL: https://link.aps.org/doi/10.1103/PhysRevLett.106.135002.

Schroeder, C. B., E. Esarey, B. A. Shadwick, and W. P. Leemans (2006). "Trapping, dark current, and wave breaking in nonlinear plasma waves". In: *Physics of Plasmas* 13.3, p. 033103. DOI: 10.1063/1.2173960. eprint: http://dx.doi.org/10.1063/1.2173960. URL: http://dx.doi.org/10.1063/1.2173960.

Schwab, MB, A Sävert, O Jäckel, J Polz, M Schnell, T Rinck, L Veisz, M Möller, P Hansinger, GG Paulus, et al. (2013). "Few-cycle optical probe-pulse for investigation of relativistic laser-plasma interactions". In: *Applied Physics Letters* 103.19, p. 191118.

Schwinger, Julian (June 1951). "On Gauge Invariance and Vacuum Polarization". In: *Phys. Rev.* 82 (5), pp. 664–679. DOI: 10.1103/PhysRev.82.664. URL: https://link.aps.org/doi/10.1103/PhysRev.82.664.

Sears, Christopher MS, Alexander Buck, Karl Schmid, Julia Mikhailova, Ferenc Krausz, and Laszlo Veisz (2010). "Emittance and divergence of laser wakefield accelerated electrons". In: *Physical Review Special Topics-Accelerators and Beams* 13.9, p. 092803.

Semushin, S. and V. Malka (2001). "High density gas jet nozzle design for laser target production". In: *Review of Scientific Instruments* 72.7, pp. 2961–2965. DOI: http://dx.doi.org/10.1063/1.1380393. URL: http://scitation.aip.org/content/aip/journal/rsi/72/7/10.1063/1.1380393.

Shaw, J. L., N. Vafaei-Najafabadi, K. A. Marsh, and C. Joshi (2012). "100 MeV injector cell for a staged laser wakefield accelerator". In: *AIP Conference Proceedings* 1507.1, pp. 315–320. DOI: 10.1063/1.4773714. eprint: http://aip.scitation.org/doi/pdf/10.1063/1.4773714. URL: http://aip.scitation.org/doi/abs/10.1063/1.4773714.

Sprangle, P., E. Esarey, and A. Ting (Apr. 1990). "Nonlinear interaction of intense laser pulses in plasmas". In: *Phys. Rev. A* 41 (8), pp. 4463–4469. DOI: 10.1103/PhysRevA.41.4463. URL: http://link.aps.org/doi/10.1103/PhysRevA.41.4463.

Su, J. J., T. Katsouleas, J. M. Dawson, and R. Fedele (Mar. 1990). "Plasma lenses for focusing particle beams". In: *Phys. Rev. A* 41 (6), pp. 3321–3331. DOI: 10.1103/PhysRevA.41.3321. URL: http://link.aps.org/doi/10.1103/PhysRevA.41.3321.

Suk, H., N. Barov, J. B. Rosenzweig, and E. Esarey (Feb. 2001). "Plasma Electron Trapping and Acceleration in a Plasma Wake Field Using a Density Transition". In: *Phys. Rev. Lett.* 86 (6), pp. 1011–1014. DOI: 10.1103/PhysRevLett.86.1011. URL: https://link.aps.org/doi/10.1103/PhysRevLett.86.1011.

Sun, Guo-Zheng, Edward Ott, Y. C. Lee, and Parvez Guzdar (1987). "Self-focusing of short intense pulses in plasmas". In: *Physics of Fluids* 30.2, pp. 526–532. DOI: http://dx.doi.org/10.1063/1.866349. URL: http://scitation.aip.org/content/aip/journal/pof1/30/2/10.1063/1.866349;jsessionid=nqR1kITkOQOgLGxRWc5Jzult.x-aip-live-03.

Thaury, Cédric, Emilien Guillaume, Andreas Döpp, Remi Lehe, Agustin Lifschitz, K Ta Phuoc, Julien Gautier, Jean-Philippe Goddet, Amar Tafzi, Alessandro Flacco, et al. (2015). "Demonstration of relativistic electron beam focusing by a laser-plasma lens". In: *Nature communications* 6, p. 6860.

Thomas, A. G. R., S. P. D. Mangles, Z. Najmudin, M. C. Kaluza, C. D. Murphy, and K. Krushelnick (Feb. 2007). "Measurements of Wave-Breaking Radiation from a Laser-Wakefield Accelerator". In: *Phys. Rev. Lett.* 98 (5), p. 054802. DOI: 10.1103/PhysRevLett.98.054802. URL: https://link.aps.org/doi/10.1103/PhysRevLett.98.054802.

Thompson, M. C., H. Badakov, J. B. Rosenzweig, G. Travish, N. Barov, P. Piot, R. Fliller, G. M. Kazakevich, J. Santucci, J. Li, and R. Tikhoplav (2010). "Observations of low-aberration plasma lens focusing of relativistic electron beams at the underdense threshold". In: *Physics of Plasmas* 17.7, p. 073105. DOI: 10.1063/1.3457924. eprint: http://dx.doi.org/10.1063/1.3457924. URL: http://dx.doi.org/10.1063/1.3457924.

Tilborg, J. van, S. Steinke, C. G. R. Geddes, N. H. Matlis, B. H. Shaw, A. J. Gonsalves, J. V. Huijts, K. Nakamura, J. Daniels, C. B. Schroeder, C. Benedetti, E. Esarey, S. S. Bulanov, N. A. Bobrova, P. V. Sasorov, and W. P. Leemans (Oct. 2015). "Active Plasma Lensing for Relativistic Laser-Plasma-Accelerated Electron Beams". In: *Phys. Rev. Lett.* 115 (18), p. 184802. DOI: 10.1103/PhysRevLett.115.184802. URL: http://link.aps.org/doi/10.1103/PhysRevLett.115.184802.

Umstadter, D., J. K. Kim, and E. Dodd (Mar. 1996). "Laser Injection of Ultrashort Electron Pulses into Wakefield Plasma Waves". In: *Phys. Rev. Lett.* 76 (12), pp. 2073–2076. DOI: 10.1103/PhysRevLett.76.2073. URL: http://link.aps.org/doi/10.1103/PhysRevLett.76.2073.

Umstadter, Donald (2003). "Relativistic laser–plasma interactions". In: *Journal of Physics D: Applied Physics* 36.8, R151. URL: http://stacks.iop.org/0022-3727/36/i=8/a=202.

Vargas, M., W. Schumaker, Z.-H. He, Z. Zhao, K. Behm, V. Chvykov, B. Hou, K. Krushelnick, A. Maksimchuk, V. Yanovsky, and A. G. R. Thomas (2014). "Improvements to laser wakefield accelerated electron beam stability, divergence, and energy spread using three-dimensional printed two-stage gas cell targets". In: *Applied Physics Letters* 104.17, 174103. DOI: http://dx.doi.org/10.1063/1.4874981. URL: http://scitation.aip.org/content/aip/journal/apl/104/17/10.1063/1.4874981.

Wagner, R., S.-Y. Chen, A. Maksimchuk, and D. Umstadter (Apr. 1997). "Electron Acceleration by a Laser Wakefield in a Relativistically Self-Guided Channel". In: *Phys. Rev. Lett.* 78 (16), pp. 3125–3128. DOI: 10.1103/PhysRevLett.78.3125. URL: https://link.aps.org/doi/10.1103/PhysRevLett.78.3125.

Whittum, David H, Andrew M Sessler, John J Stewart, and Simon S Yu (1990). "Plasma suppression of beamstrahlung". In: *Particle Accelerators* 34.1-2, pp. 89–104.

D Ehrenwörtliche Erklärung

Ich erkläre hiermit ehrenwörtlich, dass ich die vorliegende Arbeit selbständig, ohne unzulässige Hilfe Dritter und ohne Benutzung anderer als der angegebenen Hilfsmittel und Literatur angefertigt habe. Die aus anderen Quellen direkt oder indirekt übernommenen Daten und Konzepte sind unter Angabe der Quelle gekennzeichnet. Die Auswahl und Auswertung des Materials ist selbständig erfolgt. Prof. Matt Zepf war an der Diskussion der Ergebnisse beteiligt. Weitere Personen waren an der inhaltlich-materiellen Erstellung der vorliegenden Arbeit nicht beteiligt. Insbesondere habe ich hierfür nicht die entgeltliche Hilfe von Vermittlungs- bzw. Beratungsdiensten (Promotionsberater oder andere Personen) in Anspruch genommen. Niemand hat von mir unmittelbar oder mittelbar geldwerte Leistungen für Arbeiten erhalten, die im Zusammenhang mit dem Inhalt der vorgelegten Dissertation stehen.

Die Arbeit wurde bisher weder im In- noch im Ausland in gleicher oder ähnlicher Form einer anderen Prüfungsbehörde vorgelegt.

Die geltende Promotionsordnung der Physikalisch-Astronomischen Fakultät ist mir bekannt.

Ich versichere ehrenwörtlich, dass ich nach bestem Wissen die reine Wahrheit gesagt und nichts verschwiegen habe.

Jena, den

E Schlusswort

Im Laufe dieser Arbeit gab es viele gute und auch einige schwere Zeiten. Ich danke allen, die mich währenddessen unterstützt haben und möchte nur einige hervorheben:

Prof. Matt Zepf, der mir viel Vertrauen entgegen gebracht hat, meine eigenen Ideen stets verfolgen zu können und zu dürfen.

Oliver Karger, mit dem zusammen die Idee für die passive Plasmalinse erst entstanden ist, als wir uns zufällig auf einer Konferenz kennen lernten.

Matthew Schwab für die grandiose Zusammenarbeit im Büro und Labor bei unserem gemeinsamen Experiment am JETI 40.

Dominik Hollatz, Andreas Seidel und Wilhelm Eschen, deren Betreuung ihrer Abschlussarbeiten mir sehr viel Freude gemacht hat.

Christian Rödel, Vasily Kharin, Sergey Rykovanov, Alexander Blinne, Marc Günter und alle andere Kollegen mit denen ich spannende Diskussionen und eine tolle Zusammenarbeit haben durfte.

Burgard Beleites und Falk Ronneberger, auf die am Laser stets Verlass war.

Wolfgang Ziegler für jegliche Unterstützung bei Konstruktionszeichnungen, insbesondere bei der Konstruktion der Gaszelle und der Magnetjoche.

Bernhard Klumbies und des gesamte Team der Werkstatt, das bei unerwarteten Problemen unkomplizierte Hilfe bot und deren Qualität in der Fertigung viel besser war, als ich es je hätte erwarten können.

Die ungenannten Freunde, durch die die letzten Jahre zu einer unvergessliche Zeit für mich wurden.

Meine Eltern und meine Schwester, die mich stets und uneingeschränkt in allen Lebenslagen unterstützt haben.